UNIVERSITY OF LJUBLJANA
FACULTY OF MATHEMATICS AND PHYSICS
DEPARTMENT OF PHYSICS

Matija Milanič

DEVELOPMENT AND EVALUATION OF PULSED PHOTOTHERMAL RADIOMETRY FOR TEMPERATURE PROFILING IN BIOLOGICAL TISSUES

Doctoral thesis

ADVISER: Assist. Prof. Boris Majaron

Ljubljana, 2008

UNIVERZA V LJUBLJANI
FAKULTETA ZA MATEMATIKO IN FIZIKO
ODDELEK ZA FIZIKO

Matija Milanič

RAZVOJ IN EVALUACIJA METODE SUNKOVNE FOTOTERMALNE RADIOMETRIJE ZA TEMPERATURNO PROFILOMETRIJO BIOLOŠKIH TKIV

Doktorska disertacija

MENTOR: doc. dr. Boris Majaron

Ljubljana, 2008

Abstract

In this dissertation we present the development and evaluation of pulsed photothermal radiometric (PPTR) temperature depth profiling in biological tissues. Motivation for this work is incomplete success in laser therapy of port-wine stain birthmarks (PWS). PPTR technique, which utilizes infrared (IR) emission from materials following pulsed laser exposure, can provide information about PWS depth and epidermal thickness, both required to optimize the therapy.

We develop three original reconstruction codes, which are based on truncated singular value decomposition (TSVD), conjugated gradient (CG) and the υ-method, respectively. All codes involve a non-negativity constraint to the sought temperature vector and automatic regularization. When applied to different test objects, all three codes produce reconstruction results, which are much more accurate than the results published in earlier PPTR studies.

Calibration of PPTR signals and the error due to linearization of PPTR signal expression is analyzed. We find that the linearization error depends on temperature amplitude, absorber depth, acquisition time, and the spectral acquisition band.

PPTR measurements commonly employ broad-band signal acquisition to increase signal-to-noise ratio (SNR), but all reported studies use a fixed effective IR absorption coefficient (μ_{eff}). We show that in samples with large spectral variation of $\mu(\lambda)$ in mid-IR, which includes most biological tissues, selection of μ_{eff} strongly affects the accuracy of the results. A novel analytical approach to determination of optimal μ_{eff} from spectral properties of the sample and radiation detector is presented. In extensive numerical simulation of PPTR temperature profiling in human skin using different IR detectors and spectral bands, we demonstrate that our approach predicts viable values of μ_{eff}.

The influence of spectral filtering on the accuracy of temperature profiles is studied by a systematic experimental comparison of PPTR temperature profiling on agar tissue phantoms utilizing the customary spectral band of the InSb detector (λ = 3.0-5.6 μm) and a narrowed acquisition spectral band (λ = 4.5-5.6 μm). To support our experimental observations, we present also a detailed numerical simulation of the experimental procedure utilizing spectral acquisition bands with the lower wavelength limit varied between λ_{l} = 3.0 μm and 5.0 μm and the upper wavelength limit fixed at 5.6 μm. The experimental and numerical simulation results indicate that spectral filtering reduces reconstruction error and broadening of temperature profiles, especially for shallower and more complex absorbing structures. Analogously, we performed the experiment and numerical simulation involving gelatin tissue phantoms, which more closely resemble human skin. Again, we find that a suitable spectral filtering (λ_{l} = 4.0–4.5 μm) is beneficial, despite the associated reduction of SNR.

We determine experimentally the accuracy of PPTR temperature depth profiling in custom tissue phantoms composed of agar gel layers separated by single very thin absorbing layers. The laser-induced temperature depth profiles, reconstructed from measured PPTR signals, correlate very well with absorber depths determined by magnetic resonance imaging and optical microscopy. We observe significant broadening and attenuation of reconstructed profiles with increasing depth of absorbing layer. Corresponding numerical analysis indicates that the broadening equals to ~13% of the absorber depth. Using a numerical simulation we also analyzed, how the accuracy of reconstructed temperature profiles depends on sampling frequency.

PACS: 02.30.Zz, 42.30.Wb, 42.62.Be, 87.57.Gg, 87.63.it, 87.64.Cc, 87.50.W-, 87.61.Ff

Keywords: pulsed photothermal radiometry (PPTR), temperature depth profiling, image reconstruction, infrared absorption

Povzetek

V disertaciji je predstavljen razvoj in evalvacija sunkovne fototermalne radiometrije (SFTR) za temperaturno profilometrijo v bioloških tkivih. Motivacija za to delo je nepopoln uspeh laserske terapije ognjenih znamenj (OZ). SFTR tehnika, ki izrablja infrardeče (IR) sevanje snovi pogrete zaradi laserskega sunka, omogoča določitev globine OZ in debeline epidermisa, podatkov pomembnih za optimizacijo zdravljenja OZ.

Zato smo razvili rekonstrukcijske algoritme, ki omogočajo reševanje inverznega problema SFTR. Algoritmi temeljijo na metodah dekompozicije po singularnih vrednostih (TSVD), konjugiranih gradientov (CG) in υ-metodi. V vse algoritme smo vključili pogoj nenegativnosti in avtomatsko regularizacijo. Ko smo jih preizkusili na različnih testnih objektih, vsi trije algoritmi vrnejo rekonstruirane rešitve, ki so precej natančnejše od rezultatov objavljenih v predhodnih študijah SFTR.

Nato smo analizirali kalibracijo SFTR signalov in napako linearizacije izraza SFTR signala. Ugotovili smo, da je napaka odvisna od amplitude in globine temperaturnih profilov, časa zajemanja in spektralnega pasu zajemanja.

SFTR meritve se običajno opravlja v širokem spektralnem pasu, saj se s tem izboljša razmerje med signalom in šumom. Vendar pa se hkrati uporablja konstantna vrednost IR absorpcijskega koeficienta μ_{eff}. Pokazali smo, da pri vzorcih z veliko variacijo IR spektra $\mu(\lambda)$, kar vključuje večino bioloških vzorcev, izbira μ_{eff} bistveno vpliva na kvaliteto rekonstrukcije. Predstavili smo nov pristop analitičnega določanja optimalne vrednosti μ_{eff}, ki vključuje spekter $\mu(\lambda)$ vzorca in spektralno občutljivost IR detektorja. Z obsežno numerično simulacijo smo pokazali, da naš analitični pristop da optimalne vrednosti μ_{eff}.

Vpliv spektralnega filtriranja na točnost rekonstruiranih temperaturnih profilov smo proučili s sistematično eksperimentalno primerjavo temperaturne profilometrije SFTR v tkivnih fantomih iz agarja, pri čemer smo uporabili celoten (λ = 3,0–5,6 μm) in zožen spektralni pas (λ = 4,5–5,6 μm) detektorja. V podporo eksperimentalnim rezultatom so izvedli tudi numerično simulacijo eksperimenta za različne spektralne pasove med λ = 3,0 in 5,6 μm. Tako eksperimentalni kot numerični rezultati nakazujejo, da zoženje spektralnega pasu zmanjša napako rekonstrukcije in razširitev rekonstruiranih temperaturnih profilov, še posebej za plitve in kompleksnejše absorbirajoče strukture. Izvedli smo tudi eksperiment in numerično simulacijo za kolagenske tkivne fantome, ki posnemajo lastnosti človeške kože bolje kot agar. Tudi v tem primeru smo ugotovili, da spektralno filtriranje izboljša rezultate rekonstrukcije, navkljub zmanjšanem razmerju signal-šum.

Eksperimentalno smo določili natančnost našega sistema SFTR na fantomih iz agarja, ki so vsebovali eno tanko plast absorberja na različnih globinah. Globine rekonstruiranih temperaturnih profilov se zelo dobro ujemajo z globinami, ki smo jih določili z optično mikroskopijo ali mikro magnetno resonančnim slikanjem. Očitna pa je razširitev in atenuacija temperaturnih profilov z naraščajočo globino absorbirajoče plasti. Izvedli smo tudi numerično simulacijo in na podlagi eksperimentalnih in numeričnig rezultatov ugotovili, da efekt razširitve znaša do 15% globine absorberja.

PACS: 02.30.Zz, 42.30.Wb, 42.62.Be, 87.57.Gg, 87.63.it, 87.64.Cc, 87.50.W-, 87.61.Ff

Ključne besede: sunkovna fototermalna radiometrija (SFTR), temperaturna globinska profilometrija, rekonstrukcija slike, infrardeča absorpcija

I would like to sincerely thank my advisor assist. prof. Boris Majaron for his guiding, discussions and support. I also thank prof. dr. J. Stuart Nelson from Department of Biomedical Engineering, University of California, Irvine, for inviting me to his group where I spent a fruitful month experimenting on PPTR temperature profilometry and OCT imaging. I am very grateful to assist. prof. Igor Serša for help with micro-MRI imaging, and to Nadja Dervišević who helped me with tissue phantoms and PPTR measurements. I also thank all my colleagues for all the fun I had during my time at the Complex Matter Department

Finally, I owe special gratitude to my family for continuous and unconditional support and to Nina for her enduring patience, understanding, and love.

Contents

Chapter 1

Introduction

Nowadays, cooperation between physics and medicine has become tighter than ever before. Physics provides medicine with new explanations, tools for diagnostics and treatment, while medicine presents physics with challenges from a completely new world. There are countless areas of cooperation; just to name some of them: x-rays, MRI, biomedical optics.[1] The advent of lasers had a great impact on modern surgery, diagnostics of eye diseases, cancer, etc. In the dissertation we are presenting the development and evaluation of a radiometric technique known as pulsed photothermal radiometry (PPTR).

The motivation for this work is incomplete success in laser therapy of port-wine stain (PWS) birthmarks. PWS are permanent hypervascular lesions in human skin, which consist of an excess of ectacic blood vessels. These are usually fully contained within the most superficial millimeter of the skin. The exact depth varies from patient to patient, but on average, the highest fractional blood content is found 200–400 μm below the epidermal-dermal junction.[2] PWS are currently treated by selective photocoagulation of the ectatic vasculature using pulsed green or yellow/orange laser. In order to optimize laser therapy parameters (pulse duration, radiant exposure, and light wavelength) on an individual patient basis, determination of PWS depth, epidermal thickness, and epidermal heating is required.[3,4]

PPTR is a noncontact technique, which utilizes infrared (IR) emission from materials following pulsed laser exposure. Selective absorption of laser radiation in subsurface cromophores results in localized heating and may be detected as transient increase in IR emission from tissue surface. When thermal properties of the sample are known, the laser-induced temperature profile can be reconstructed from acquired radiometric signals. Such PPTR temperature profiling was recognized as a promising technique for non-invasive determination of structure and cromophore distribution in strongly scattering biological tissues and was extensively investigated.[5–12]

In contrast to alternative diagnostic techniques, which utilize detection of scattered or frequency converted light from the irradiated tissue (e.g., optical coherence tomography,[13] diffuse optical tomography,[14] ultrasound-modulated optical tomography[15]), PPTR provides a signal amplitude that is directly related to the initial space-dependent temperature increase in targeted cromophores. An important advantage of PPTR over the photoacustic technique[16] is that the measurement is made without touching the sample. For example, resting a photoacustic probe on the skin surface for several seconds may change the hydratation of stratum corneum, while slightly heavier contact will change the hemodynamics in the area under the probe.

In the dissertation we present development and evaluation of a PPTR system for temperature profiling in biological tissues performed at the Complex Matter Department at the Jožef Stefan Institute in Ljubljana, Slovenia. The work involved development of novel reconstruction algorithms, numerical analysis of PPTR profiling, construction and optimization of a laboratory PPTR system and experiments on tissue phantoms.

The dissertation is structured as follows. The PPTR temperature profiling inverse problem is derived in Chapter 2. Chapter 3 describes the actual PPTR temperature profiling setup. Expressions for radiometric signal and measurement noise are derived, which are then used in experimental characterization of our PPTR temperature profiling system. In Chapter 4 we develop original reconstruction codes for solving the PPTR temperature profiling inverse problem. The calibration procedure and error estimation due to simplifications of PPTR signal expression are presented in Chapter 5. Chapter 6 presents the effect of the monochromatic approximation deficiency on reconstructed temperature profile for different spectral acquisition bands, and an analytical approach for determination of the optimal effective absorption coefficient. Chapter 7 analyzes the influence of the sampling rate.

Second part of the dissertation presents experimental evaluation of the PPTR system performance. We begin with construction of tissue phantoms, which serve as test samples in our experiments (Chapter 8). The experiments and numerical simulations on agar (Chapter 9) and collagen gel tissue phantoms (Chapter 10) demonstrate the effect of spectral filtering on reconstructed temperature profiles. In Chapter 11 we analyze the accuracy of reconstructed temperature profiles, specifically the depth and width of reconstructed temperature profiles. In Chapter 12 we summarize the main ideas and conclusions.

Chapter 2

Theoretical background

The mechanism of PPTR signal generation was given in early work by Leung and Tam.[17] Basic relations for PPTR temperature depth profiling were first derived in one dimension and monochromatic approximation,[6–9] and later on extended to account for spectral variation of the sample IR absorption coefficient $\mu(\lambda)$ in the mid-IR detection range.[18] The one-dimensional theory was also extended to three-dimensions.[19]

We derive an expression for PPTR signal amplitude $\Delta S(t)$ in terms of the initial temperature depth profile $\Delta T(z, 0)$ in a tissue immediately following pulsed laser irradiation. For the purpose of our analysis, we assume that the tissue occupies a semi-infinite half-space. We use the one-dimensional heat equation for the temperature increase $\Delta T(z, t)$[20]

$$D\,\frac{\partial^2 \Delta T}{\partial z^2} + \frac{\partial \Delta T}{\partial t} - Q\Delta T = 0 \tag{2.1}$$

with a mixed boundary condition at the air-tissue interface

$$\left.\frac{\partial \Delta T}{\partial z}\right|_{z=0} - h\Delta T\big|_{z=0} = 0 \tag{2.2}$$

where D denotes the thermal diffusivity of tissue, which we assume is homogenous, h represents the reduced heat transfer coefficient at the air-tissue interface. In addition to heat diffusion, heat can be removed from the irradiated tissue also by the blood flow. The effect of blood flow is included in (2.2) as the blood perfusion rate Q. We do not include heat loss due to radiation in (2.1), because it is significantly smaller than heat conduction for typical experimental conditions. The Green's function solution to (2.1)–(2.2)[21] represents temperature increase in the tissue at depth z and time t in response to instantaneous release of a planar impulse heat source at depth z' and time $t = 0$

$$G_{\mathrm{T}}(z',z,t) = \frac{e^{-Qt}}{\sqrt{4\pi Dt}}\left\{e^{-(z-z')^2/4Dt} + e^{-(z-z')^2/4Dt}\left[1 - h\sqrt{4\pi Dt}\,\mathrm{erfcx}(u)\right]\right\} \tag{2.3}$$

where

$$u = \frac{z+z'}{\sqrt{4Dt}} + h\sqrt{Dt}$$

and $\mathrm{erfcx}(u) = \exp(u^2)\,\mathrm{erfc}(u)$, where $\mathrm{erfc}(u)$ is the complementary error function. Because the relaxation time due to blood perfusion ($1/Q$) in the microvasculature is much longer than the time of measurement, the exponent function involving Q can be neglected from (2.3). Using the Green's function solution, the temperature depth profile $\Delta T(z, t)$ at an arbitrary depth z and time t is written as

$$\Delta T(z,\,t) = \int_{z'=0}^{\infty} \Delta T(z,0)\; G_{\mathrm{T}}(z',z,t)\;\mathrm{d}z \tag{2.4}$$

The regular expression for radiometric signal of blackbody involving constant temperature T_{b}, can be generalized to correspond to objects with non-homogenous temperature distribution by including z-integral with factor $\mu(\lambda)\exp(-\mu(\lambda)\,z)$. Thus, the measured radiometric signal $S(t)$ is then given by integrating Planck's expression for radiative emission $B_\lambda(T_\mathrm{b} + \Delta T(z, t))$ over all depths

$$S(t) \;=\; C \int_{\lambda_\mathrm{l}}^{\lambda_\mathrm{h}} R(\lambda)\; \mu(\lambda) \int_{z=0}^{\infty} B_\lambda \left[T_\mathrm{b} + \Delta T(z,t) \right] e^{-\mu(\lambda)\, z}\, \mathrm{d}z\, \mathrm{d}\lambda \tag{2.5}$$

where λ_l and λ_h are the lower and upper limit of the detection spectral range, respectively, while $R(\lambda)$ describes spectral sensitivity of the radiation detector. The constant C accounts for sample emissivity and other experimental specifics (e.g., losses of collection optics, radiation detector field of view, etc.). However, we obtain the regular expression for radiometric signal of blackbody by setting $\Delta T(z, t) = 0$ and integrating the z-integral.

When the induced temperature rise $\Delta T(z, t)$ is significantly smaller than T_b, we can expand $B_\lambda(T_\mathrm{b})$ in Taylor series, which leads to the linearized expression for the transient part of the spectrally composite radiometric signal

$$\Delta S(t) \;=\; C \int_{\lambda_\mathrm{l}}^{\lambda_\mathrm{h}} R(\lambda)\, B_\lambda{}'(T_\mathrm{b})\; \mu(\lambda) \int_{z=0}^{\infty} \Delta T(z,t)\;\, e^{-\mu(\lambda)\, z}\, \mathrm{d}z\, \mathrm{d}\lambda \tag{2.6}$$

where $B_\lambda'(T_\mathrm{b})$ represents the temperature derivative of $B_\lambda(T_\mathrm{b})$. From (2.4) the PPTR signal is related to the laser-induced temperature profile $\Delta T(z,0)$ by a simple convolution

$$\Delta S(t) \;=\; \int_{z=0}^{\infty} K(z,t)\, \Delta T(z,0)\, \mathrm{d}z \tag{2.7}$$

with the kernel function $K(z,t)$ defined by (2.3)–(2.6):

$$K(z,t) \;=\; C \int_{\lambda_\mathrm{l}}^{\lambda_\mathrm{h}} R(\lambda)\, B_\lambda{}'(T_\mathrm{b})\; \mu(\lambda) \int_{0}^{\infty} G_\mathrm{T}(z',z,t)\; e^{-\mu(\lambda)\, z'}\, \mathrm{d}z'\, \mathrm{d}\lambda \tag{2.8}$$

When using a spectrally invariant value μ is justified (or assumed), $K(z,t)$ can be simplified through factorization of the double integral in (2.8):

$$\tilde{K}(z,t) \;=\; C \int_{\lambda_\mathrm{l}}^{\lambda_\mathrm{h}} R(\lambda)\, B_\lambda{}'(T_\mathrm{b})\, \mathrm{d}\lambda\;\, \mu \int_{0}^{\infty} G_\mathrm{T}(z',z,t)\; e^{-\mu z'}\, \mathrm{d}z' \tag{2.9}$$

where, for given experimental conditions, the first integral yields a constant. This relation allows us to establish a direct correspondence with earlier reports on PPTR depth profiling, disregarding the spectral variation $\mu(\lambda)$. By inserting $G_\mathrm{T}(z', z, t)$, the second integral results in[6]

$$\kappa(z,t) = \frac{1}{2} \exp[-z^2/(4D\,t)] \left\{ \mathrm{erfcx}(u_-) + \mathrm{erfcx}(u_+) + \frac{2h}{\mu - h} \left[\mathrm{erfcx}(u_+) - \mathrm{erfcx}(u_1) \right] \right\} \tag{2.10}$$

with $\mathrm{erfcx}(u) = [1 - \mathrm{erf}(u)]\exp(u^2)$, $u_\pm = \mu\sqrt{Dt} \pm z/(2\sqrt{Dt})$, $u_1 = h\sqrt{Dt} + z/(2\sqrt{Dt})$.

In experimental practice, PPTR signals are represented by vectors, and relation (2.7) becomes multiplication of the initial temperature profile vector $\boldsymbol{T}$ ($T_j = \Delta T(z_j,0)$) with kernel matrix $\boldsymbol{K}$ ($K_{i,j} = K(z_j,t_i)\, \Delta z$)

$$\boldsymbol{S} = \boldsymbol{K}\, \boldsymbol{T} \tag{2.11}$$

Chapter 3

Experimental setup

Figure 3.1 shows a schematic of an experimental PPTR system. The test object is irradiated with a single pulse from a pulsed laser. The irradiation spot size must be large (typical diameter ~ 5 mm) as compared to the surface of the studied volume of the sample (typical diameter ~ 1 mm), because one-dimensional analysis is used. IR emission is monitored at normal incidence to the sample surface by a radiation detector. IR radiation is collected on the detector by an IR collection lens. The electrical response of the detector, after preamplification, is monitored by a fast analog-to-digital converter. A silicon photodiode is used to detect the laser pulse onset. Digitized signals are stored and processed in a personal computer.

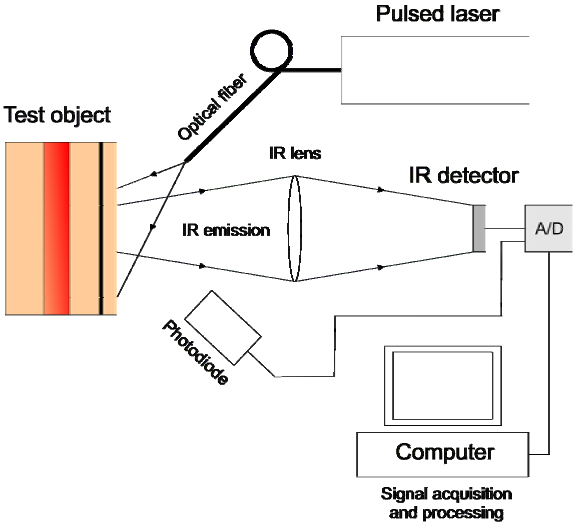

Figure 3.1: Experimental setup for PPTR temperature profiling in biological tissues.

3.1 Pulsed laser source

Any pulsed light source, which is selectively absorbed in the sample, can be used to induce the initial temperature profile. For PPTR temperature profiling in human skin, we most often apply the same light sources as used for laser therapy: pulsed green (KTP/YAG, λ = 532 nm) or yellow/orange lasers (flashlamp-pumped dye, 577 nm and 585-600 nm). Since the above wavelengths are preferentially absorbed in melanin and hemoglobin, which are located in epidermis and blood vessels, we obtain information about epidermal thickness and blood vessel distribution. Furthermore, temperature profiles similar to those induced during laser therapy are obtained when the above therapeutic lasers are used.

The required pulse energies depend on the irradiation spot size, detector sensitivity and cromophore absorption. Clearly, it is desirable to avoid any thermal damage. Pulse length τ should ideally be about 1 ms or less to prevent excessive heat diffusion from induced temperature profiles. Table 3.1 lists some combinations of excitation wavelength λ, radiant exposure H and pulse length τ used for PPTR temperature profiling in human skin. In our experiments we used a pulsed-dye laser (PDL) at wavelength 585 nm with pulse length 1.5 ms (ScleroPlus, Candela, Wayland, MA, USA) and a KTP laser generating 1 ms long 532 nm laser pulses (Dualis^{VP}, Fotona, Ljubljana).

Table 3.1: Some combinations of excitation wavelength λ, radiant exposure H and pulse length τ used for PPTR temperature profiling in human skin. PDL – pulsed dye laser, KTP – second harmonic Nd:YAG laser.

Laser type	λ (nm)	H (J/cm^2)	τ (ms)	References
PDL	585	7.0	0.45	6
PDL	577	0.5	0.001	9
KTP	532	3.4	2–10	19
PDL	585–600	5.0–6.0	1.5	18

3.2 IR radiation detector

Commercially available IR radiation detectors are divided into two groups: thermal and quantum detectors. The former are not applicable to PPTR temperature profiling, because they have a low signal-to-noise (SNR) ratios and they are not convenient for measurement of transient phenomena. Common IR detectors involved in PPTR temperature profiling are liquid nitrogen cooled photovoltaic InSb and photoconductive HgCdTe (MCT) quantum detectors. The main disadvantage of the photoconductive detector is that it requires a mechanical chopper to modulate IR radiation. The chopper limits the sampling rate to a few 1000 s^{-1}, introduces additional measurement noise to the radiometric signal, requires a lock-in amplifier and generates air current, which increases the heat loss at the sample surface (h). Furthermore, InSb detector offers a more predictable responsivity,[22] which is especially favorable for numerical simulations. In contrast, MCT detector yields larger PPTR signals, since wider spectral acquisition bands can be used, and the temperature derivative of Planck's formula $B_\lambda'(T_b)$ is larger for these spectral bands (see Fig. 3.3, *dashed line*). Considering the advantages and weaknesses of both detectors, we have decided to use the InSb detector in our experimental setup.

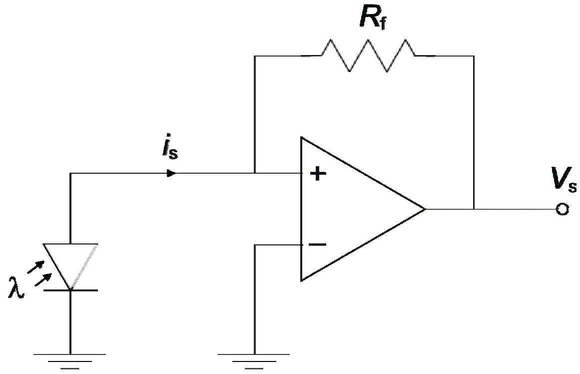

Figure 3.2: Current mode preamplifier circuit for InSb detector. λ represents IR radiation, i_s signal current, R_f feedback resistor, and V_s signal voltage.

Photovoltaic detectors are diodes made from semiconductor materials. InSb material typically has a band gap of 0.22 eV at temperature $T = 77$ K, thus only photons with $\lambda \leq 5.5$ µm are detected. This maximal detectable wavelength is called the cut-off wavelength (λ_c). When the diode is exposed to IR radiation, it generates a current proportional to the photon arrival rate. Photovoltaic detectors are commonly used in a current preamplifier circuit (Fig. 3.2), where voltage drop across the detector is practically zero.

When monochromatic radiation of wavelength λ and power P irradiates the photovoltaic detector, the signal current i_s equals[22]

$$i_s = \frac{\eta \lambda e_0}{h c} P \tag{3.1}$$

where η denotes quantum efficiency (about 0.64 for InSb), e_0 is the electron charge, h represents the Planck's constant and c the speed of light. The spectral responsivity of a radiation detector $R(\lambda)$ is defined as the signal output i_s divided by the radiant input P, thus the theoretical spectral responsivity of InSb detector is easily deduced from (3.1)

$$R(\lambda) = \eta e_0 \frac{\lambda}{hc} \tag{3.2}$$

Figure 3.3 shows relative spectral responsivity $R(\lambda)/R_p$ for a specific InSb detector (P5968-100, Hamamatsu) with the peak responsivity $R_p = 2.5$ A/W at $\lambda_p = 5.3$ μm and a specific HgCdTe detector (P3257, Hamamatsu) with the peak responsivity at $\lambda_p = 10$ μm.

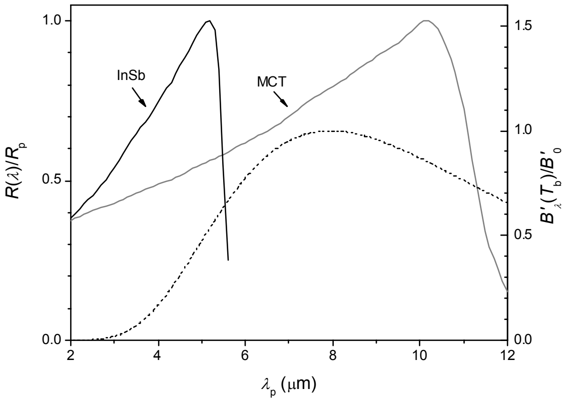

Figure 3.3: Relative spectral responsivity $R(\lambda)$ of InSb and HgCdTe (MCT) detectors (*solid lines*) with peak responsivities at $\lambda_p = 5.3$ μm and 10.0 μm, respectively. Temperature derivative of Planck's radiation formula $B_\lambda'(T_b)$ at $T_b = 303$ K (*dashed line*) has the maximum at 8 μm.

3.2.1 Measurement noise

Noise present in an IR detection system originates from a number of sources.[22,23]

Shot noise originates from the discrete nature of photodetection process. Its amplitude is

$$n_{sh} = \sqrt{2 e_0 i_s \Delta f} \tag{3.3}$$

where Δf represents frequency bandwidth. Frequency bandwidth is calculated as $1/(2t_{\text{int}})$, where t_{int} is the integration time.

Johnson noise originates from random motion of free charges. Its amplitude is

$$n_J = \sqrt{\frac{4k_B T_d \Delta f}{R_f}} \tag{3.4}$$

where k_B is the Boltzmann's constant, T_d represents temperature of the detector, and R_f is the feedback resistance (see Fig. 3.2).

Other contributions to measurement noise include amplifier noise, digitalization noise and external noises. Inasmuch as multiple noise sources are present, we can use the central-limit theorem to estimate square of the total noise amplitude n_t as the sum of squares of amplitudes of all noise contributions.

While most noise contributions are spectrally invariant ("white"), so-called *1/f noise* is often present in radiometric signals. In general, the presence of 1/f noise is characterized by the corner frequency f_c and exponent α. The total noise spectral density $\tilde{n}_t$ is given by[22]

$$\tilde{n}_\mathrm{t}^2 = \tilde{n}_\mathrm{white}^2 \left[\left(\frac{f_\mathrm{c}}{f} \right)^\alpha + 1 \right] \tag{3.5}$$

where $\tilde{n}_\mathrm{white}$ denotes the spectral density of white noise and f represents frequency. For discrete radiometric signals, the total noise amplitude n_t and the noise spectral density $\tilde{n}_\mathrm{t}$ are correlated using the discrete Parseval's theorem[24]

$$n_\mathrm{t}^2 = \frac{\sum_{i=1}^{N} \tilde{n}_\mathrm{t}^2(f_i)}{N^2} \tag{3.6}$$

where f_i represent the discrete frequencies and N denotes the number of radiometric signal and spectral density data points.

3.3 Infrared optics

Figure 3.4 presents the transmittance $T(\lambda)$ of three materials commonly utilized for mid-IR optics (λ = 3–5 µm).

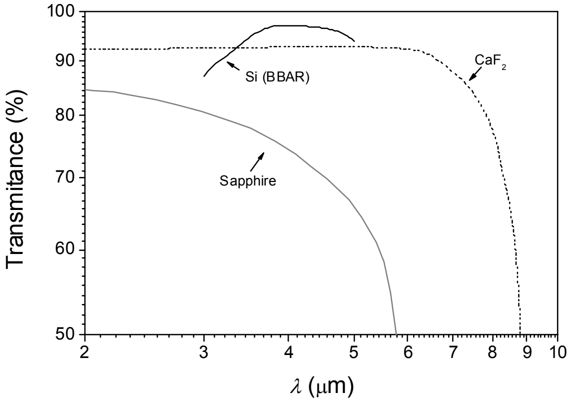

Figure 3.4: Transmittance of broadband antireflex coated silicon (Tydex, St. Petersburg, Russia), sapphire (MellesGriot), and CaF_2 (ThorLabs).

In our setup we use the broadband antireflex silicon IR optics because of large transmittance in the λ = 3–6 µm spectral band and good mechanical characteristics. The collection optics consists of two planoconvex silicon antireflex coated lenses (Galvoptics, Essex, UK) with transmittance $T \geq 98\%$ at the 3–5 µm spectral band. The lenses are positioned in such a manner that magnification is $M = 1$ (Fig. 3.5).

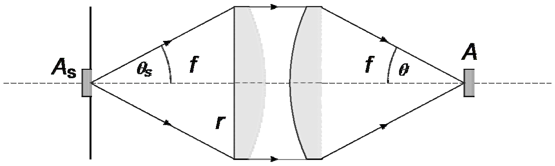

Figure 3.5: Schematics of the 2-lens collection optics with magnification $M = 1$. The source area A_s equals the detector active area A, and the collection angle at the source θ_s matches the collection angle θ at the IR detector. Arrows indicate direction of IR radiation.

3.4 Radiometric signal

Figure 3.5 presents a schematic of radiometric signal collection using the 2-lens collection optics with $M = 1$. The source area A_s equals the IR detector active area A and the collection angle at the source θ_s matches the collection angle θ of the IR detector. Expression for θ follows from Fig. 3.5

$$\tan\theta = \frac{r}{f} \tag{3.7}$$

where r is the lens radius (i.e., aperture) and f represents its focal length.

The amount of radiant power emitted from the source area A_s at temperature T_b at wavelength λ and which falls within the solid angle dΩ around the direction specified by θ_s is

$$\mathrm{d}P_\lambda = \frac{\varepsilon}{\pi} B_\lambda(T_\mathrm{b}) \cos\theta_\mathrm{s}\, A_\mathrm{s}\ \mathrm{d}\Omega \tag{3.8}$$

where ε denotes the sample emissivity. The radiation power varies as the cosine of θ_s (Lambert's law). The total radiation power P_λ emitted into the solid angle θ_s is found by integrating (3.8)

$$P_\lambda = \varepsilon \sin^2\theta_\mathrm{s}\, A_\mathrm{s}\ B_\lambda(T_\mathrm{b}) \tag{3.9}$$

In absences of transmission lenses, the emitted power equals the collected power on the detector. However, the power must be reduced for the collection optic losses. Hence, the analogous expression to (3.8) for the collected radiation power is obtained

$$P_\lambda = \varepsilon\, T(\lambda)\, \sin^2\theta\ A\ B_\lambda(T_\mathrm{b}) \tag{3.10}$$

Accordingly, the radiometric signal i_s is detected in a broad spectral band between λ_l and λ_h

$$i_\mathrm{s} = \varepsilon \sin^2\theta\ A \int_{\lambda_\mathrm{l}}^{\lambda_\mathrm{h}} T(\lambda)\ R(\lambda)\ B_\lambda(T_\mathrm{b})\ \mathrm{d}\lambda \tag{3.11}$$

3.5 Experimental characterization of our PPTR system

In our system, IR radiation is detected by a single-element InSb detector (P5968-100, Hamamatsu). The detector properties, as specified by the manufacturer, are active area A = 0.79 mm^2 (d = 1 mm), half-angle of the field of view θ = 22.5°, and spectral responsivity $R(\lambda)$ with peak value R_p = 2.5 A/W at λ_p = 5.3 µm (Fig. 3.3), while the cut-off wavelength is λ_c = 5.6 µm.

In addition, the manufacturer has specified measurement noise under specific conditions, where small radiometric signal from a 500 K blackbody is detected in a background-limited regime (BLIP) at modulation frequency of 1200 Hz, and with a small frequency bandwidth Δf (1 Hz). The peak detectivity D_p^*, as a standard figure of merit[22] can be calculated from the reported noise standard deviation and the above detector parameters, resulting in $D_\mathrm{p}^* = 2.8 \times 10^{11}$ cm Hz$^{1/2}$/W. This value does not include 1/f noise, which may dominate at lower frequencies, and other noise sources (i.e., amplifier noise, external noise sources), which may be present in an actual PPTR system. Therefore, we have determined experimentally the noise parameters for our PPTR system.

We measured the response of the IR detector using a blackbody (BB701, Omega Engineering, Stamford, CT, USA) set to different temperatures, T_BB = 288–232 K. The entire detector's field of view was filled with radiation from the blackbody. The detector response at each T_BB was acquired using the entire spectral band of the IR detector (λ = 3.0–5.6 µm). The radiometric values were acquired at a sampling rate of 50,000 s^{-1}. We have numerically reduced the sampling rate by calculating the average value of 50 consecutive values (t_int = 1 ms). This yielded radiometric signals

$s(T_{BB})$ with the sampling rate $f = 1000\ s^{-1}$ and frequency bandwidth $\Delta f = 500\ s^{-1}$.

We determined theoretical values of $s(T_{BB})$ by inserting the blackbody temperature T_{BB} and the system parameters into (3.11) and completing the λ integral. The blackbody emissivity was $\varepsilon = 0.94$ and transmittance $T = 0.98$ (both specified by the manufacturers). Figure 3.6 presents the average of experimental radiometric signals (*circles*), which matches perfectly the theoretically predicted signal values (*line*); thus (3.11) adequately predicts the PPTR system response when the above $R(\lambda)$ is used.

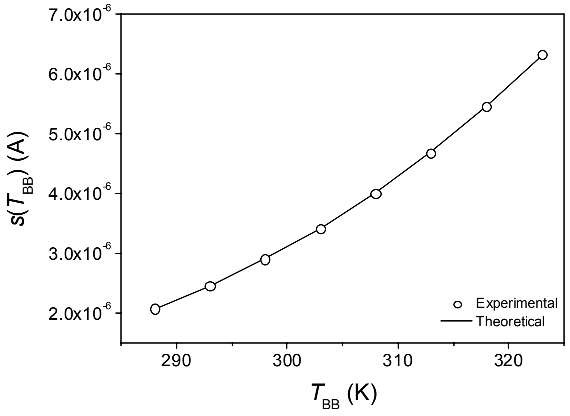

Figure 3.6: Experimental (*circles*) and theoretical (*line*) radiometric signal values $i_s(T_{BB})$ determined for T_{BB} = 288–323 K and for the entire spectral band.

To obtain the noise spectrum each determined signal $s(T_{BB})$ was Fourier transformed using the *fft* function implemented in Matlab 14 (Mathworks, Natick, MA, USA). We fit (3.5) to the noise spectrum to determine the noise parameters f_c and α. The total noise amplitude n_t was determined as the standard deviation of $s(T_{BB})$, albeit it could be found also from the noise spectrum using the discrete Parseval's theorem (Eq. 3.6). An example of a noise spectrum and the corresponding fit of (3.7) is presented in Fig. 3.7. The 1/f noise evidently dominates at frequencies below ~20 s^{-1}.

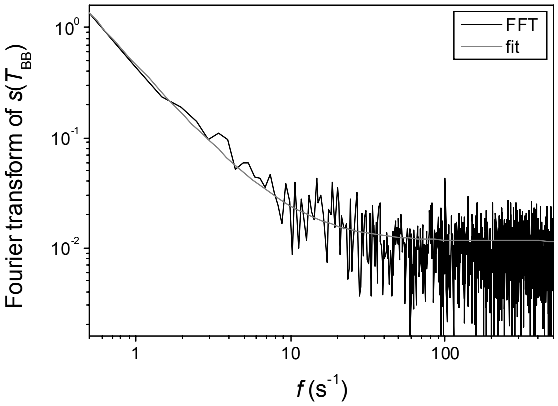

Figure 3.7: An example of a noise spectrum measured at T_{BB} = 303 K using the entire spectral band (*black line*) and the best fit of function $\tilde{n}_t^2$ (Eq. 3.5) (*gray line*). The determined noise parameters are total noise amplitude n_t = 3.2×10^{10} A, corner frequency $f_c = 15\ s^{-1}$, and exponent $\alpha = 1.5$.

In order to accurately discern between detector-specific noise n_d and shot noise n_{sh}, the detector response at each T_{BB} was acquired also using a long-pass IR filter (Barr Associates, Westford, MA; see Fig. 3.8) placed between the blackbody and the detector.

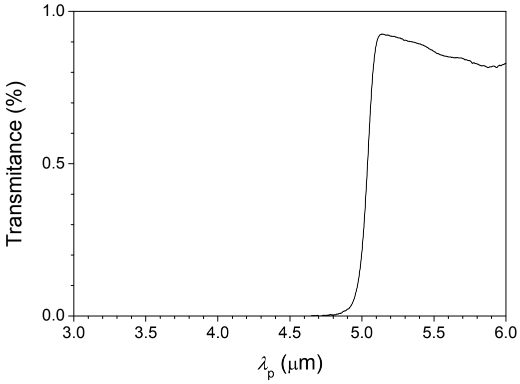

Figure 3.8: Transmittance of a long-pass IR filter with cut-on wavelength of λ = 5 μm (Barr Associates, Westford, MA).

Then, we calculated shot noise amplitudes n_{sh} for each temperature T_{BB} and both spectral acquisition bands by substituting the measured radiometric signals $s(T_{\text{BB}})$ into (3.3). Figure 3.9 presents the experimental noise amplitudes n_{t} and shot noise amplitudes n_{sh} as a function of T_{BB}. For the entire spectral band (Fig. 3.9a), values n_{t} are scattered around the average value 3.1×10^{-10} A with a standard deviation of ~10^{-11} A. Shot noise amplitudes n_{sh} increase monotonically with increasing T_{BB}, but are approximately 10 times smaller than n_{t}. For the reduced spectral band (Fig. 3.9b), n_{t} is $(2.9 \pm 0.1) \times 10^{-10}$ A. Since detector-specific noise obviously dominates in our PPTR system and the average n_{t} is almost identical for both spectral bands, a constant value $n_{\text{t}} = 3 \times 10^{-10}$ A suitably characterizes the total noise in our PPTR signals at $\Delta f = 500$ s^{-1}.

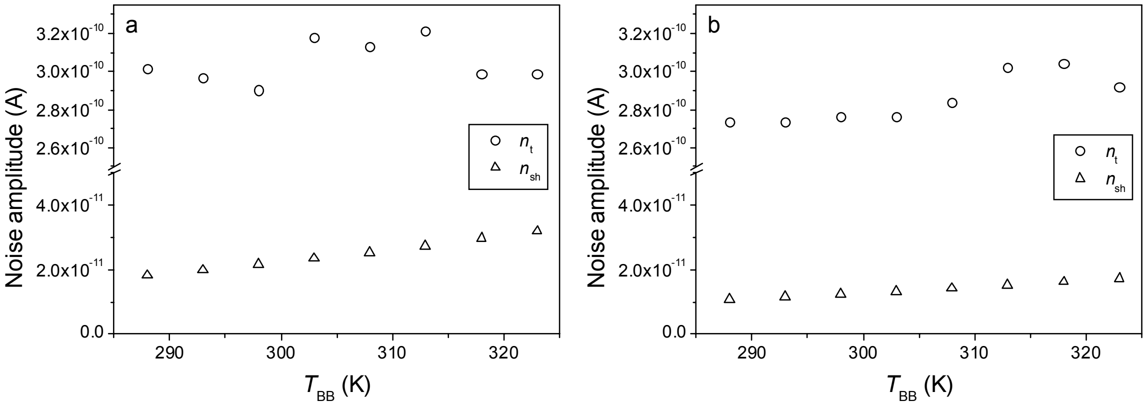

Figure 3.9: Determined total noise amplitude n_{t} (*circles*) and shot noise amplitude n_{sh} (*triangles*) as functions of T_{BB} for (a) the entire spectral band and (b) the reduced spectral band.

Radiometric signals measured by our PPTR system are dominated by the 1/f-noise at low frequencies (Fig. 3.7). The average corner frequency is $f_{\text{c}} = 15 \pm 10$ s^{-1} and 10 ± 8 s^{-1} for the entire and reduced spectral acquisition band, respectively. The average exponent is $\alpha = 1.3 \pm 0.4$ for both spectral acquisition bands.

Chapter 4

Reconstruction algorithms

Ill-posed inverse problems arise quite often when one is interested in determining the internal structure of a physical system from the system's measured behavior. It is well known that a small perturbation of signal (i.e. noise) can substantially change the solution. Ordinary methods for solving algebraic equations (i.e., inversion) do not succeed in solving ill-posed problems therefore special methods must be used. A good survey of numerical methods applicable to general classes of algebraic equations is provided by Björck,[25] while reconstruction algorithms suitable for the ill-posed problems are described by Hansen.[26]

In this chapter, we analyze the PPTR inverse problem using the singular value decomposition (SVD). Then, we describe the development original reconstruction codes dedicated to solving the PPTR inverse problem. Finally, we show that our reconstruction codes perform significantly better than the general purpose algorithms available on the market and earlier dedicated codes for PPTR profilometry.

4.1 Discrete ill-posed problems

Basic relations of PPTR temperature profiling were derived in Chapter 2. The expression for PPTR signal (2.7) represents a Fredholm integral equation of the first kind, which results in a discrete forward problem (2.11). The calculation of kernel matrix components $K_{i,j}$ (see Eq. 2.10) is a delicate task, since it involves mathematical operations on very large (i.e., exponential function) and very small numbers (i.e., error function). Hence, one must consider the order of mathematical operations and include adequate approximations to avoid unwanted numerical errors (see the Appendix B). Equation (2.11) represents the PPTR inverse problem for $\boldsymbol{T}$, which is commonly solved by iterative minimization of the residual norm $\| \boldsymbol{S} - \boldsymbol{K}\,\boldsymbol{T} \|^2$, yielding the best approximate solution $\boldsymbol{T}$. A statistical approach to the minimization problem can be found in Calvetti.[28] The process of finding the approximate solution $\boldsymbol{T}$ is also referred to as reconstruction.

4.1.1 Singular Value Decomposition

Singular value decomposition (SVD) is a useful tool for analysis of discrete ill-posed problems.[25,26] The SVD of the matrix $\boldsymbol{K}$ is a unique decomposition of the form

$$\boldsymbol{K} = \boldsymbol{U}\,\boldsymbol{\Sigma}\,\boldsymbol{V} = \sum_{i=1}^{n} \boldsymbol{u}_i\,\sigma_i\,\boldsymbol{v}_i^{\mathrm{T}} \tag{4.1}$$

where $\boldsymbol{U} \int \mathrm{IR}^{m\times n}$ and $\boldsymbol{V} \int \mathrm{IR}^{n\times n}$ are matrices with orthonormal columns, $\boldsymbol{U}^{\mathrm{T}}\boldsymbol{U} = \boldsymbol{V}^{\mathrm{T}}\boldsymbol{V} = \boldsymbol{I}$. The diagonal matrix $\boldsymbol{\Sigma}$ has nonnegative diagonal elements σ_i sorted in nonincreasing order. The numbers σ_i are called singular values of $\boldsymbol{K}$, while the vectors $\boldsymbol{u}_i$ and $\boldsymbol{v}_i$ are left and right singular vectors of $\boldsymbol{K}$, respectively.

Using the orthonormal basis vectors $\boldsymbol{u}_i$ and $\boldsymbol{v}_i$, we can write

$$\boldsymbol{T} = \sum_{i=1}^{n} \left(\boldsymbol{v}_i^{\mathrm{T}} \boldsymbol{T} \right) \boldsymbol{v}_i \tag{4.2a}$$

$$\boldsymbol{S} = \sum_{i=1}^{n} \left(\boldsymbol{u}_i^{\mathrm{T}} \boldsymbol{S} \right) \boldsymbol{u}_i \tag{4.2b}$$

When (4.1) and (4.2) are inserted into (2.11), we obtain

$$\sum_{i=1}^{n} \left(\boldsymbol{u}_i^{\mathrm{T}} \boldsymbol{S} \right) \boldsymbol{u}_i = \sum_{i=1}^{n} \sigma_i \left(\boldsymbol{v}_i^{\mathrm{T}} \boldsymbol{T} \right) \boldsymbol{u}_i \tag{4.3}$$

which leads to an expression for solution ***T***

$$\boldsymbol{T} = \sum_{i=1}^{n} (\boldsymbol{u}_i^{\mathrm{T}} \boldsymbol{S} / \sigma_i) \, \boldsymbol{v}_i \tag{4.4}$$

We now illustrate the characteristics of the PPTR inverse problem (2.11). The kernel matrix ***K*** is calculated by evaluating (2.9), where the size of ***K*** is 1000 × 100, corresponding to time intervals Δt = 1ms over 1s and to spatial resolution Δz = 10 μm extending to a depth of 1 mm. The heat diffusion constant is D = 0.11 mm^2 s^{-1}, the reduced heat transfer coefficient is h = 0.02 mm^{-1}, and the IR absorption coefficient is μ = 50 mm^{-1}.

Singular values σ_i of the kernel matrix ***K*** are presented in Fig. 4.1. The singular values decay according to the exponential law ($\sigma_i \sim \exp(-\alpha\, i)$), thus the PPTR inverse problem is classified as severely ill-posed.[29] The more ill-posed is the problem, the slower is the convergence of regularization algorithms.[30] Evidently, the accuracy of computed singular values is limited by the computational platform (e.g., a personal computer with 32-bit precision has $\varepsilon = 2.22\times10^{-16}$). As a result, σ_i settle at a level which is approximately equal to the machine precision.

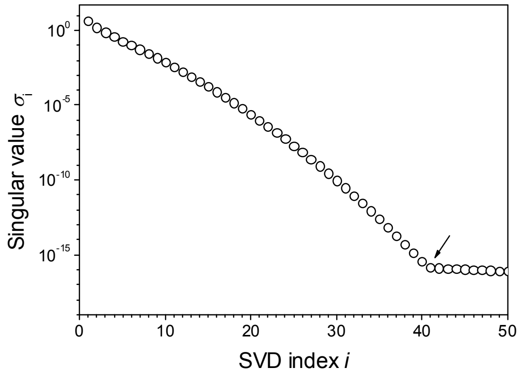

Figure 4.1: Singular values σ_i of the kernel matrix ***K***. Arrow indicates where the computer platform accuracy (32-bit personal computer) prevents accurate calculation of further singular values.

Left singular vectors $\boldsymbol{u}_i$ (*white background*) and right singular vectors $\boldsymbol{v}_i$ (*gray background*) corresponding to the largest eight singular values of ***K*** are shown in Fig. 4.2. Vectors with larger indices i clearly present more sign changes. SVD gives an important insight the smoothing effect in forward direction. While σ_{i} decrease the singular vectors $\boldsymbol{u}_i$ and $\boldsymbol{v}_i$ become more and more oscillatory. The high-frequency components of ***T*** are more damped in ***S*** than the low-frequency components due to multiplication with small σ_{i} (see Eq. 4.3). In contrast, division by σ_i in (4.4) amplifies the high-frequency oscillations in ***S***, thus amplifying high frequency components including the noise in ***S***, and deteriorating accuracy of the solution ***T***.

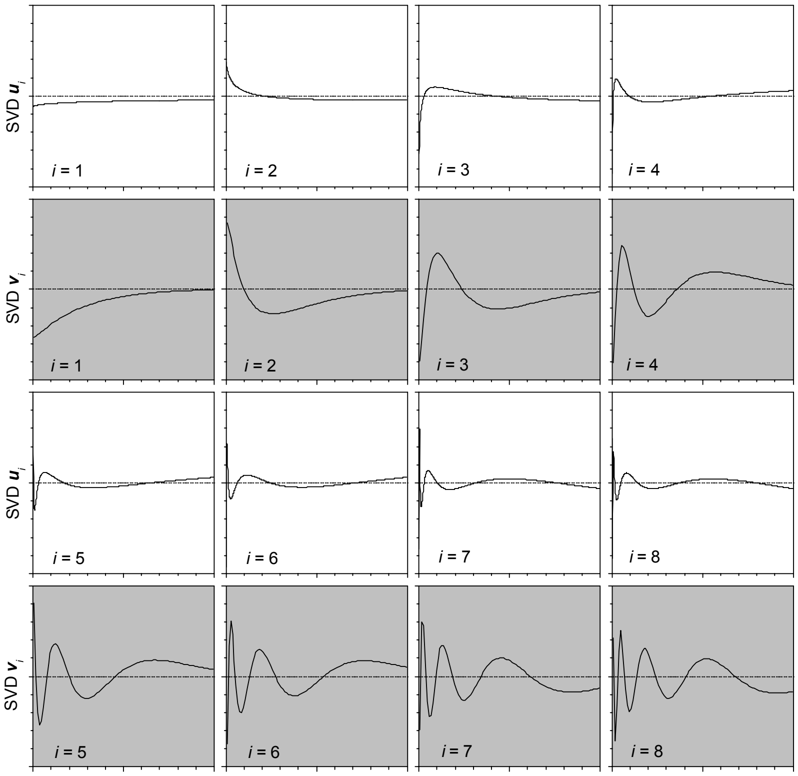

Figure 4.2: Eight left singular vectors $\boldsymbol{u}_i$ (*white background*) and right singular vectors $\boldsymbol{v}_i$ (*gray background*) of $\boldsymbol{K}$. Horizontal dashed lines represent zero value.

4.2 Reconstruction algorithms

From a general perspective, we can choose between two classes of reconstruction algorithms: direct algorithms that are based on decomposition, such as singular value decomposition (SVD), and iterative algorithms.

A number of direct algorithms exist,[25,26] but we focus on the truncated SVD (TSVD). An advantage of the direct regularization methods is that the computational effort can be estimated a priori, because they are based on standard operations and decompositions in numerical algebra.

Iterative algorithms are based on iteration schemes that access the kernel matrix $\boldsymbol{K}$ only via matrix-vector multiplications, and they produce a sequence of iteration vectors $\boldsymbol{T}^{(i)}$, that converge toward the desired solution. When iterative algorithms are applied to discrete ill-posed problems, the iteration vector initially approaches the correct solution, but in later stages of the iterations, some other undesired vector is obtained.[26] This is referred to as semiconvergence. Iterative methods are preferred when $\boldsymbol{K}$ is large, because explicit decomposition of $\boldsymbol{K}$ requires a large amount of computer memory. We discuss below two iterative methods: the υ-method and the conjugate gradient (CG) method.

4.2.1 Truncated SVD

In the ideal setting, without perturbations and rounding errors, the treatment of the PPTR inverse problems (2.11) is simple. The optimal solution is computed by means of (4.4). In practice, there are various types of errors in $\boldsymbol{S}$, such as discretization and measurement errors, including noise. Also, $\boldsymbol{K}$ may not describe accurately all the involved physical processes. Finally, accumulation of the rounding errors cannot be avoided in computation of the inverse solution.

Yet, the effect of perturbations and rounding errors can be minimized by a choice of such integer $p<n$

that a solution $\boldsymbol{T}_p$ close to the correct solution to the PPTR inverse problem is obtained by truncating (4.4) after adding p SVD components to the solution. The solution $\boldsymbol{T}_p$ is referred to as the truncated SVD solution and the method is referred to as truncated SVD (TSVD).[26]

4.2.2 υ-method

The υ-method[31] is an iterative method derived from the classical Landweber iterative method.[26] Landweber method has very slow convergence compared to the CG methods, but the υ-method is significantly accelerated by involving a weighted average of the last two iterates and allowing that weight factors μ_i and ω_i (Algorithm 4.1) depend on iteration number i. The υ-method is presented Algorithm 4.1. Here, υ is a prescribed real constant satisfying $\upsilon \int (0,1)$. Since convergence of the method depends on value υ, we performed some tests using different values of υ, and find optimal value $\upsilon = 0.99$ for our problem. The υ–method does not converge if $\|\boldsymbol{K}\|_2 > 1$, and the convergence is fastest if $\|\boldsymbol{K}\|_2$ is slightly smaller than 1. Therefore we assured the convergence by substituting $\boldsymbol{K}$ and $\boldsymbol{S}$ with a modified kernel matrix and signal vector, i.e. $\boldsymbol{A}$ and $\boldsymbol{b}$ (see 1st and 2nd line of Algorithm 4.1).), where ε is a small real constant (e.g., $\varepsilon = 10^{-3}$). The υ–method features the semiconvergence, where the regularization parameter is number of iterations i.

Algorithm 4.1: The *υ-method*. Vector $\boldsymbol{T}_{reg}$ minimizes the expression $\|\boldsymbol{S} - \boldsymbol{K}\,\boldsymbol{T}_i\|^2$. Vector $\boldsymbol{S}$ is provided as input.

```
$\boldsymbol{A} = \boldsymbol{K} / (\|\boldsymbol{K}\|_2 + \varepsilon)$;
$\boldsymbol{b} = \boldsymbol{S} / (\|\boldsymbol{K}\|_2 + \varepsilon)$;
i = 0;
$\boldsymbol{T}^{(0)} = 0$;
$\boldsymbol{r}^{(0)} = \boldsymbol{b}$;
repeat:
    $\mu_i = 1 + (i - 1)(2i - 3)(2i + 2\upsilon - 1) / [(i + 2\upsilon - 1)(2i + 4\upsilon - 1)(2i + 2\upsilon - 3)]$;
    $\omega_i = 4(2i - 2\upsilon - 1)(i - \upsilon - 1) / [(i - 2\upsilon - 1)(2i + 4\upsilon - 1)]$;
    $\boldsymbol{T}^{(i)} = \mu_i \boldsymbol{T}^{(i-1)} + (1 - \mu_i)\boldsymbol{T}^{(i-2)} + \omega_i \boldsymbol{A}^{\mathrm{T}} \boldsymbol{r}^{(i-1)}$;
    $\boldsymbol{r}^{(i)} = \boldsymbol{b} - \boldsymbol{A}\,\boldsymbol{T}^{(i)}$;
    i = i + 1;
until (stopping criterion)
$\boldsymbol{T}_{reg} = \boldsymbol{T}^{(i)}$;
```

4.2.3 Conjugate Gradients (CG)

The basic CG iteration scheme for non-selfadjoint matrices $\boldsymbol{K}$ is well known,[32] but several implementation variants exist. A comprehensive survey of different CG variants was provided by Hanke,[33] while a simple and understandable text about CG method was published by Shewchuk.[30] Based on preliminary testing, we have selected the CG least-square (CGLS) algorithm presented in Algorithm 4.2.[26]

An essential property of the CG iterates $\boldsymbol{T}^{(i)}$ with residual vectors $\boldsymbol{r}^{(i)} = \boldsymbol{S} - \boldsymbol{K}\,\boldsymbol{T}^{(i)}$ is that the corresponding vectors $\boldsymbol{K}^{\mathrm{T}} \boldsymbol{r}^{(i)}$ are orthogonal. An important consequence is that if the starting vector $\boldsymbol{T}^{(0)}$ is zero, then the solution norm $\|\boldsymbol{T}^{(i)}\|_2$ increases monotonically with i and the residual norm $\|\boldsymbol{r}^{(i)}\|_2$ decreases monotonically with i.[33] The CG method produces iteration vectors in which the spectral components associated with the large singular values converge faster than the remaining components, hence the CG features an inherent semiconvergence.

Algorithm 4.2: The *CG least-square* (*CGLS*) algorithm. Vector $\boldsymbol{T}_{reg}$ minimizes expression $||\boldsymbol{S} - \boldsymbol{K}\,\boldsymbol{T}_i||^2$. Vector $\boldsymbol{S}$ is provided as input.

```
$i = 0$;
$\boldsymbol{T}^{(0)} = 0$;
$\boldsymbol{r}^{(0)} = \boldsymbol{S} - \boldsymbol{K}\,\boldsymbol{T}^{(0)}$;
$\boldsymbol{d}^{(0)} = \boldsymbol{K}^{\mathrm{T}}\,\boldsymbol{r}^{(0)}$;
repeat:
    $\alpha_i = ||\boldsymbol{K}^{\mathrm{T}}\,\boldsymbol{r}^{(i-1)}||_2^2 \,/\, ||\boldsymbol{K}\,\boldsymbol{d}^{(i-1)}||_2^2$;
    $\boldsymbol{T}^{(i)} = \boldsymbol{T}^{(i-1)} + \alpha_i\,\boldsymbol{K}^{\mathrm{T}}\boldsymbol{r}^{(i-1)}$;
    $\boldsymbol{r}^{(i)} = \boldsymbol{r}^{(i-1)} - \alpha_i\,\boldsymbol{K}\,\boldsymbol{d}^{(i-1)}$;
    $\beta_i = ||\boldsymbol{K}^{\mathrm{T}}\,\boldsymbol{r}^{(i)}||_2^2 \,/\, ||\boldsymbol{K}^{\mathrm{T}}\,\boldsymbol{r}^{(i-1)}||_2^2$;
    $\boldsymbol{d}^{(i)} = \boldsymbol{K}^{\mathrm{T}}\,\boldsymbol{r}^{(i)} + \beta_i\,\boldsymbol{d}^{(i-1)}$ ;
    $i = i + 1$;
until(stopping criterion);
$\mathbf{T}_{\mathrm{reg}} = \mathbf{T}^{(\mathrm{i})}$;
```

4.3 Regularization

An ill-posed problem can be regularized by adding a regularization term to the problem (e.g. Tikhonov regularization),[34] which penalizes large solution estimates. This regularization approach suffers from low computational efficiency, because the reconstruction is repeated several times for different values of regularization parameter. But the early termination approach significantly reduces computational costs since each successive reconstruction algorithm step represents a new regularized solution. Regarding the accuracy of reconstruction results of PPTR inverse problem, both approaches are equal,[6] thus we use early termination. The regularization parameter in TSVD is the number p of right singular vectors $\boldsymbol{v}_i$ included in the regularized solution $\boldsymbol{T}^{(p)}$, while the iteration number i serves as the regularization parameter in CG and the υ-method.

Since the experiments can often not be repeated, we would like to extract as much information as possible from the given data. If we choose a regularization parameter smaller than the optimal parameter, we leave out too much information and the regularization error dominates. In this case the solution is over-regularized. On the other hand, if we choose a regularization parameter larger than optimal, then the perturbation error dominates and the solution is under-regularized.

So far we have presented three different reconstruction algorithms, but no method for selection of the regularization parameter. Although many parameter-selection methods exist,[26] we discuss below the discrepancy principle, the generalized cross validation and the L-curve method, which can be successfully applied to our inverse problem.

4.3.1 Discrepancy Principle

In practice various types of errors are present in $\boldsymbol{S}$ and $\boldsymbol{K}$. Common sources of error are measurement noise, approximations, errors due to the discretization process, and also the rounding errors. We denote the vector including all errors as $\boldsymbol{e}$. If knowledge or an estimate of the norm of signal perturbation $||\boldsymbol{e}||_2$ is available, the discrepancy principle suggests stopping the iteration when the corresponding residual norm is approximately equal to $||\boldsymbol{e}||_2$

$$\left\| \boldsymbol{S} - \boldsymbol{K}\boldsymbol{T}^{(i)} \right\|_2 = \delta_\mathrm{e} \tag{4.5}$$

where $\delta_\mathrm{e} \geq \|\boldsymbol{e}\|_2$. In general, the discrepancy principle tends to produce over-regularized solutions.

4.3.2 Generalized Cross-Validation

Generalized cross-validation (GCV) was first presented by Craven[35] and Golub.[36] GCV is an $\|\boldsymbol{e}\|_2$-free method for choosing the regularization parameter based on statistical considerations. The optimal regularization parameter i_opt is found at the minimum of the following GCV function $G(i)$

$$G(i) = \frac{\left\| \boldsymbol{S} - \boldsymbol{K}\boldsymbol{T}^{(i)} \right\|_2^2}{\left[n - \rho(i) \right]^2} \tag{4.6}$$

where $\rho(i)$ is the sum of all filter factors in the regularized solution $\boldsymbol{T}^{(i)}$ (see Appendix A). Unfortunately, the minimum can be very flat, which leads to numerical difficulties in computing the minimum of $G(i)$.

For TSVD, $\rho(i) = i$ and thus the GCV function is simplified to

$$G(i) = \frac{\left\| \boldsymbol{S} - \boldsymbol{K}\boldsymbol{T}^{(i)} \right\|_2^2}{(n - i)^2} \tag{4.7}$$

A different approach to computing the denominator in the GCV function, which is particularly attractive for iterative methods, is to approximate the denominator by a statistical estimate. This approach is called Monte Carlo GCV.[37] The idea is to simultaneously run the iterative method on the given left-hand side $\boldsymbol{S}$ and on a random left-hand side $\underline{\boldsymbol{S}}$ whose elements have a zero mean and standard deviation σ_0. If $\underline{\boldsymbol{T}}^{(i)}$ denotes the additional iteration vector corresponding to $\underline{\boldsymbol{S}}$, then

$$\sigma_0^2 \left[n - \rho(i) \right] = \underline{\boldsymbol{S}}^\mathrm{T} \left(\underline{\boldsymbol{S}} - \boldsymbol{K}\underline{\boldsymbol{T}}^{(i)} \right) \tag{4.8}$$

This estimate can be used in the GCV function. However, the Monte Carlo CGV doubles the amount of work in an iterative regularization method.

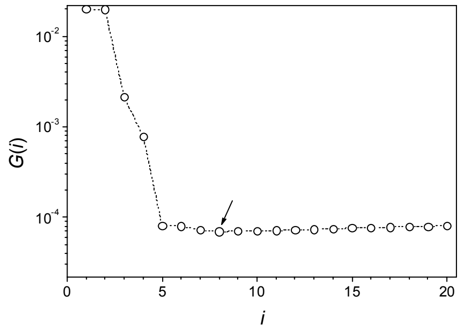

Figure 4.3: $G(i)$ as a function of added singular vectors i, when the unconstrained TSVD is applied to a simulated PPTR signal with $SNR = 100$ (Fig. 4.6). Arrow indicates the minimum.

Figure 4.3 shows the GCV function $G(i)$ (4.7) when the unconstrained TSVD is applied to a simulated PPTR signal with SNR = 100 (see Fig. 4.6). The minimum of the curve is indicated by the arrow (i = 8).

4.3.3 L-Curve

The L-curve criterion was first introduced by Lawson.[38] It is based on a parametric plot of logarithm of the norm $||\boldsymbol{T}^{(i)}||_2$ versus logarithm of the corresponding residual norm $||\boldsymbol{S} - \boldsymbol{K}\,\boldsymbol{T}^{(i)}||_2$, with the iteration count i as the parameter. The L-curve theoretically consists of an almost horizontal and a steeply ascending part. The horizontal part corresponds to over-regularized solutions and the ascending part corresponds to under-regularized solutions. The L-shaped corner of the L-curve appears for regularization parameter close to the optimal value, which balances the regularization and perturbation errors in the regularized solution $\boldsymbol{T}$ (see Hansen,[26] chapters 4 and 7).

Figure 4.4 shows the L-curve for the same example as in Fig. 4.3. It features a characteristic L-shape with a distinct corner at $i = 8$.

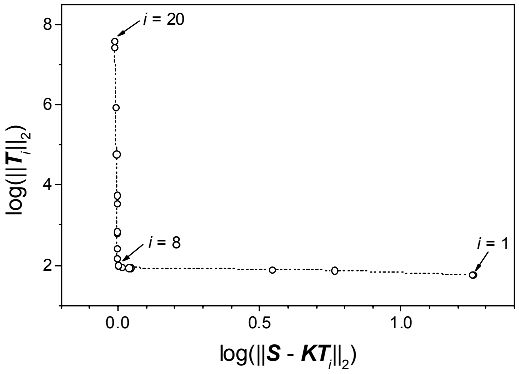

Figure 4.4: L-curve for the unconstrained TSVD applied to a PPTR signal with $SNR = 100$ (Fig. 4.6). Arrow indicates the corner of L-curve ($i = 8$).

4.3.3 Regularization and reconstruction algorithms: summary

To find which combinations of regularization selection method and reconstruction algorithm are optimal, we performed an extensive numerical simulation. We have combined the unconstrained TSVD, υ-method and CGLS with the above regularization parameter selection methods, and applied these combined algorithms to PPTR signals for different test objects presented in the last section of this chapter. Since the study was extensive, and the study details are not essential for this thesis, we only summarize the results.

Optimal results were obtained when the υ-method was combined with the Monte Carlo GCV, and CGLS was combined with the L-curve method, while TSVD yielded comparable results when combined with either GCV or L-curve. In contrast, the discrepancy principle was only useful if accurate noise information was available.

We have found that GCV and L-curve occasionally yield under-regularized solutions, which was also reported by Hansen.[26] Hence, we have included in our reconstruction codes also the discrepancy principle to improve their robustness.

4.4 Non-negativity constraint

One of the shortcomings of the discussed reconstruction algorithms is presence of unrealistic negative temperatures in the solutions. Because we know that the temperature changes in PPTR profilometry are strictly non-negative, it is very desirable that the reconstructed temperature profile $\boldsymbol{T}$ has only non-negative values. Thus we search for solution of a constrained minimization problem

$$\min \left\| \boldsymbol{S} - \boldsymbol{K}\,\boldsymbol{T} \right\|^2, \qquad \text{subjec to } T_i \geq 0, \ \text{for all}\, i \tag{4.9}$$

Milner *et al*[6] reported a successful implementation of the non-negativity constraint into the CG method. They observed significantly improved accuracy and increased robustness of reconstruction results, when the non-negatively constrained reconstruction algorithm was applied to the PPTR inverse problem. Unfortunately, the authors did not reveal the implementation details.

Different techniques for computing regularized non-negative solutions (images) to linear discrete ill-posed problems have been recently proposed in the literature. The projected Landweber method was discussed by Bertero and Boccacci.[39] Hanke *et al* suggested the use of a nonlinear transformation of the unknown variable, which eliminates the need to explicitly impose the constraint.[40] Nagy *et al* suggested a modified steepest descent method, referred to as MRNSD.[41] Calvetti *et al* proposed two iterative schemes, based on the generalized minimum residual method (GMRES) or the CGLS method.[42] Verkruysse *et al* demonstrated implementation of the non-negativity constraint into TSVD.[46] The efficiency of various iterative reconstruction algorithms was studied by Favati *et al.*[43]

In the following we present two approaches for implementation of the non-negativity constraint into the presented reconstruction algorithms.

In addition to these, we have also tested three algorithms that do not require any special non-negativity strategy. The expectation-maximization algorithm (EM)[44,41] and the image space reconstruction algorithm (ISRA)[45], both popular in astronomy and medical imaging, have yielded poor reconstruction results. The MRNSD[41] algorithm resulted in somewhat better solutions, but still significantly less accurate as compared to the reconstruction codes discussed below.

4.4.1 Projection

When projection is implemented into the reconstruction algorithm, all the negative components of iterative solutions $\boldsymbol{T}^{(i)}$ are set to zero in each step of the algorithm (i.e., $\boldsymbol{T}^{(i)}$ is cropped). This strategy can be successfully implemented into the υ-method, where semiconvergence is preserved.[26] The non-negatively constrained reconstruction algorithm based on the υ-method equals Algorithm 4.1, except that $T^{(i)}$ is cropped before the new residual vector $\boldsymbol{r}^{(i)}$ is calculated (line 10). In contrast, a direct implementation of non-negativity constraint in CGLS conflicts with underlying assumptions of the method and severely degrades its convergence and stability.

4.4.2 Projected-Restarted approach

In the projected-restarted (PR) approach, the unconstrained reconstruction algorithm runs in the inner loop, while the non-negativity constraint is applied in the outer iteration loop.[42] We now describe two new algorithms, where the PR approach is applied to the regularized CGLS and TSVD.

We begin with an unbiased starting approximation (i.e., $\boldsymbol{T}^{(0)} = 0$), which makes the initial residual vector ($\boldsymbol{r}^{(0)}$) equal to the signal vector $\boldsymbol{S}$. One full run of the inner loop (one of the unconstrained regularization methods) is then performed, yielding a temporary unconstrained solution $\boldsymbol{t}$. This vector is truncated to become the first non-negative approximate solution of the outer loop ($\boldsymbol{T}^{(1)}$). Only the new residual vector ($\boldsymbol{r}^{(1)} = \boldsymbol{S} - \boldsymbol{K}\boldsymbol{T}^{(1)}$) is then passed to the inner loop for another run. In this way, each successive run of the inner loop result $\boldsymbol{t}$ provides an unconstrained correction to the current outer solution. After the sum of the two is cropped (i.e., $(\boldsymbol{T}^{(1)} + \boldsymbol{t}) \geq 0$), we obtain an improved non-negative solution ($\boldsymbol{T}^{(2)}$). This sequence is repeated until a predefined convergence criterion is reached, or until the number of outer iteration steps exceeds a preset maximal number ($i_{\max}$). The last $\boldsymbol{T}^{(i)}$ represents the regularized solution of the minimization problem (2.11).

Algorithm 4.3 presents a practical realization of the PR approach for the regularized CGLS and TSVD reconstruction algorithms.

Algorithm 4.3: *Projected-restarted* (PR) approach combined with the CGLS or TSVD reconstruction algorithm. The non-negativity constraint is implemented in the outer loop, while the inner loop performs the unconstrained regularization using either unconstrained regularization algorithm. $(...)^+$ indicates the cropping operator.

```
$\boldsymbol{T}^{(0)} = 0$;
$\boldsymbol{r}^{(0)} = \boldsymbol{S}$;
i = 0;
repeat:
    $\boldsymbol{t}$ = CGLS($\boldsymbol{r}^{(i)}$) or TSVD($\boldsymbol{r}^{(i)}$);
    $\boldsymbol{T}^{(i+1)} = (\boldsymbol{T}^{(i)} + \boldsymbol{t})^+$;
    $\boldsymbol{r}^{(i+1)} = \boldsymbol{S} - \boldsymbol{K}\,\boldsymbol{T}^{(i+1)}$;
    i = i + 1;
until ($\|\boldsymbol{T}^{(i+1)} - \boldsymbol{T}^{(i)}\| / \|\boldsymbol{T}^{(i)}\| < \varepsilon$ or $i < i_{\max}$);
$\boldsymbol{T}_{reg} = \boldsymbol{T}^{(i)}$;
```

4.5 Performance of constrained reconstruction algorithms

In this section we present reconstruction results of different test objects obtained by our non-negatively constrained reconstruction algorithms with automatic regularization and results of other reported PPTR studies.

4.5.1 Hyper-Gaussian test profile

The performance of the dedicated CGLS reconstruction code is demonstrated here by re-evaluation of a test example from an earlier PPTR study,[18] where a general-purpose commercial optimization software was used (Solver, part of Microsoft Excel™). In order to provide an objective evaluation of the algorithm performance, we present the basic outline and simulation parameters from the earlier study.

The initial temperature profiles have a hyper-Gaussian form: $\Delta T(z, 0) = \Delta T_0 \exp[-2(z-z_0)^4/w^4]$ with ΔT_0 = 10 K, w = 0.1 mm and z_0 = 0.3 mm. PPTR signal is computed according to (2.11) and is represented as vector $\boldsymbol{S}$ with 250 equidistant components (Δt = 2 ms), augmented by normally distributed white noise (SNR = 300). Mismatch between the image and test object is evaluated by calculating normalized quadratic norm of the difference between the image and object vectors

$$\delta = \frac{\|\boldsymbol{T} - \boldsymbol{T}_0\|_2}{\|\boldsymbol{T}_0\|_2} \tag{4.10}$$

Figure 4.5 presents a comparison between the commercial (Fig.4.5a) and our dedicated (Fig.4.5b) reconstruction algorithm. Evidently, we have obtained a significantly improved reconstruction result (Fig.4.5b) for exact same test example and conditions. In particular, the broadening is substantially reduced and the pronounced deep artifact is completely eliminated from the image. The relative image error is δ = 0.46 for the earlier result, and is reduced almost 6 times (δ = 0.08) when the CGLS algorithm is used. Similar improvement is observed also for other test objects. [47] We also applied optimization algorithms implemented in Matlab 7 software (The MathWorks, Inc.) to different PPTR signals, and corresponding reconstruction results were significantly less accurate and less stable than those obtained by our dedicated algorithms.

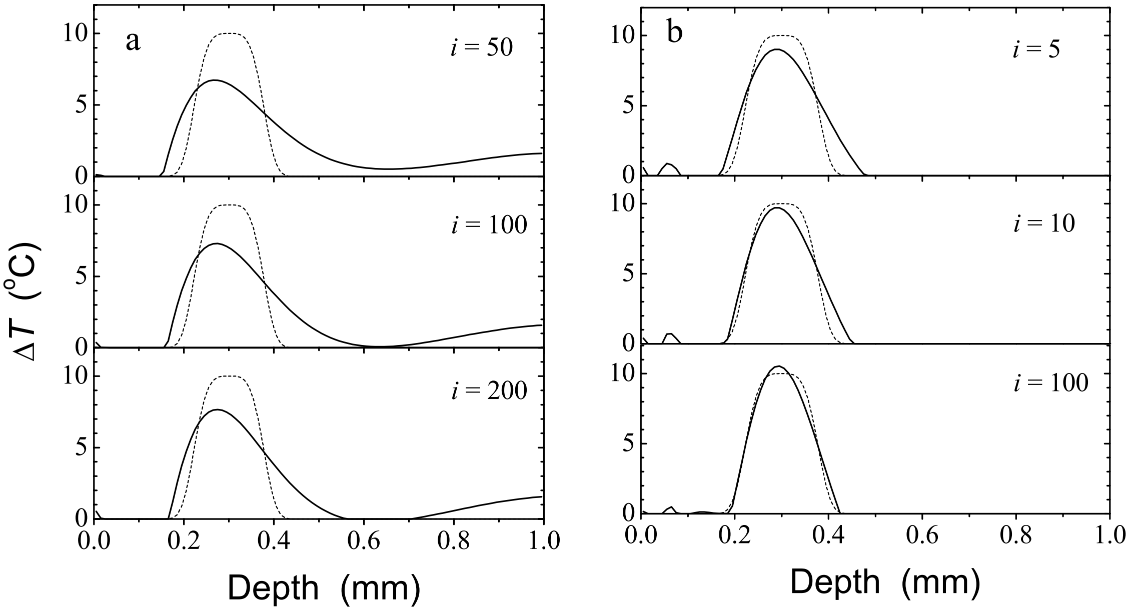

Figure 4.5: Temperature profiles as obtained (a) by the commercial software (Solver, part of Microsoft Excel™) in an earlier PPTR study,[18] and (b) by our dedicated non-negatively constrained reconstruction algorithm (PR-CGLS).[47] The results obtained after *i* steps of the iterative algorithm are presented.

Because the same computational platform was used in both studies (i.e., a personal computer with a 32-bit Microsoft Windows operating system), this improvement can be attributed to our dedicated reconstruction code. In addition, the use of Chebyshev approximation and consideration of numerical errors (see the Appendix B) enables computation of the kernel matrix elements with higher accuracy than the approach used in the earlier study.[18]

4.5.2 Two absorbing layers

Milner *et al*[6] used their non-negatively constrained reconstruction algorithm based on dedicated CG method and obtained prominently more accurate results as compared to other reported PPTR studies. We now compare the performance of our reconstruction algorithms by re-evaluating one of their examples.

The initial temperature profile features two temperature peaks due to radiative absorption

$$\Delta T(z,0) = \begin{cases} \Delta T_{\mathrm{E},} & z_{\mathrm{E1}} < z < z_{\mathrm{E2}} \\ \Delta T_{\mathrm{P}} \exp\left[-\mu_{\mathrm{a}}(z - z_1)\right], & z_{\mathrm{P1}} < z < z_{\mathrm{P2}} \\ 0, & \text{elsewhere} \end{cases} \tag{4.11}$$

where ΔT_{E} = 40 K, z_{E1} = 10 μm, z_{E2} = 50 μm, ΔT_{P} = 20 K, z_{P1} = 350 μm, z_{P2} = 1000 μm, and $\mu_{\mathrm{a}} = 5\ \mathrm{mm}^{-1}$.

The size of the kernel matrix $\boldsymbol{K}$ is 256 × 128 corresponding to time interval of Δt = 8 ms over 2.048 s and spatial resolution of Δz = 8 μm extending to a depth of 1.02 mm. The diffusion constant is $D = 0.11\ \mathrm{mm}^2\ \mathrm{s}^{-1}$, the IR absorption coefficient is $\mu = 50\ \mathrm{mm}^{-1}$, and the reduced heat loss coefficient is $h = 0.02\ \mathrm{mm}^{-1}$. The exact PPTR signal $\boldsymbol{S}_0$ corresponding to test problems is obtained using (2.9). Figure 4.6a presents temperature profile vector $\boldsymbol{T}_0$, and Figure 4.6b shows the calculated theoretical PPTR signal vector $\boldsymbol{S}_0$. Because the reconstruction results depend on specific realization of noise, we augment each theoretical signal $\boldsymbol{S}_0$ with 20 different realizations of zero-mean white noise at SNR = 100, 500, and 1000, with SNR is determined as

$$SNR = \langle \Delta S(t) \rangle \Big/ \langle e^2 \rangle^{1/2} \tag{4.12}$$

where <> represents a time average of either PPTR signal $\Delta S(t)$ or noise e^2.

From each signal vector $\boldsymbol{S}$, the temperature profile $\boldsymbol{T}$ is reconstructed using the kernel matrix $\boldsymbol{K}$ and three reconstruction algorithms. We applied the PR-TSVD algorithm with the GCV regularization parameter selection method, the PR-CGLS algorithm with L-curve, and the υ-method with the Monte Carlo GCV, since numerical simulation results show that these combinations are optimal (section 4.3). The maximum number of iterations is $i_{\max} = 20{,}000$ and the convergence criterion is set to $\varepsilon = 10^{-5}$.

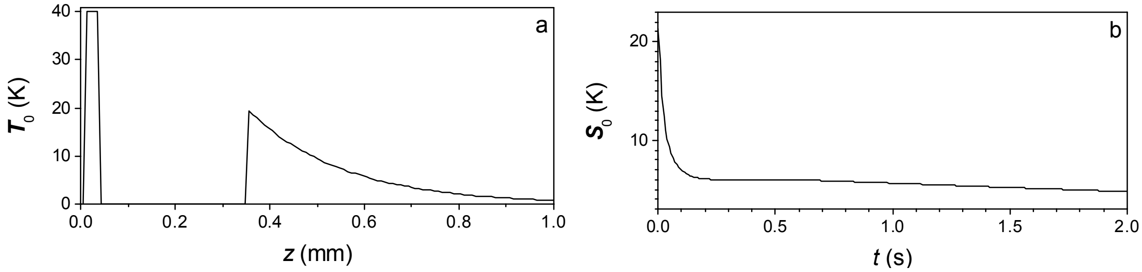

Figure 4.6: (a) Temperature profiles $\boldsymbol{T}_0$ and (b) corresponding theoretical PPTR signals $\boldsymbol{S}_0$ for the test object featuring two absorbing layers

Figure 4.7 presents a statistical analysis of 20 regularized solutions. Solid black lines connect the average solution values, while the gray bars indicate the standard deviation. At a given SNR, all three reconstruction algorithms result in comparable solutions. Standard deviation of the solution $\boldsymbol{T}$ decreases with increasing SNR for the PR-TSVD and PR-CGLS, but increases for the projected υ-method – likely due to more right singular vectors $\boldsymbol{v}_i$ included in the solution $\boldsymbol{T}$.

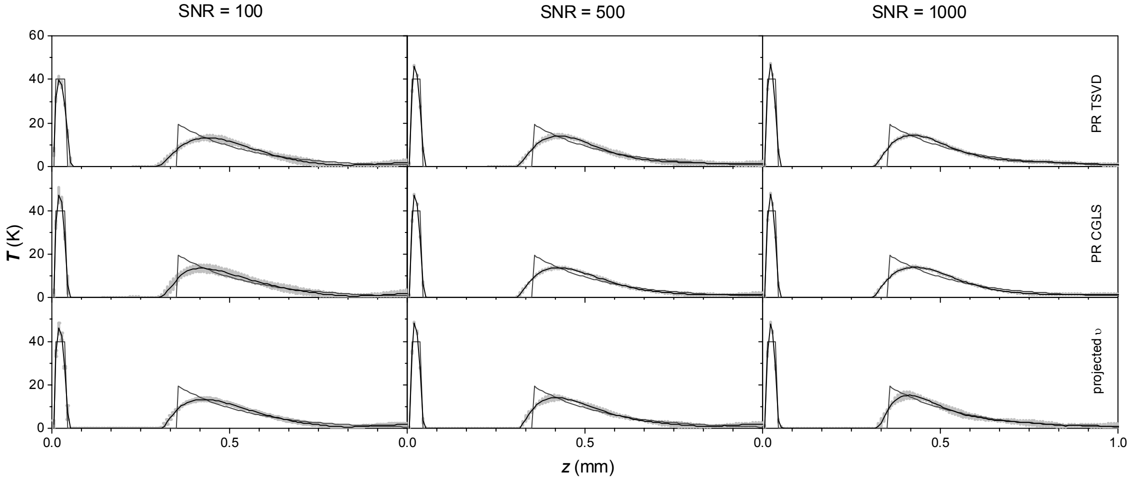

Figure 4.7: Statistical analysis of 20 regularized solutions $\boldsymbol{T}$ for the second test object obtained using the PR TSVD (*top row*), PR CGLS (*middle row*), and projected υ-method (*bottom row*). SNR levels are 100 (*left*), 500 (*center*), and 1000 (*right*). The actual object is presented for comparison (*dark-gray line*). Gray bars represent standard deviations.

The corresponding relative image errors are presented in Fig. 4.8. The υ-method results in the smallest image error (*dark-gray bars*; δ = 0.27, 0.26, and 0.24 at SNR = 100, 500, and 1000, respectively). With this method, we also obtain minimal standard deviations of δ and minimal $\delta_{\max}$, which is the maximal obtained image error value for the same example and SNR. However, the differences between δ obtained by different methods are insignificant at SNR = 500 and 1000.

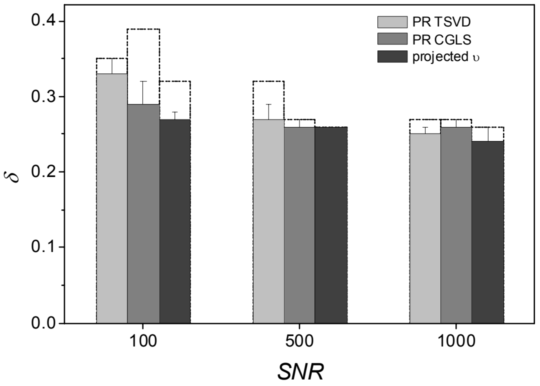

Figure 4.8: Relative image errors δ (Eq. 4.10) of images of the second test object obtained using the PR TSVD (*light-gray bar*), PR CGLS (*gray bars*), and υ-method (*dark-gray bars*). Corresponding maximal obtained image error δ is represented by dashed-line bar.

The temperature profiles reconstructed by our algorithms resemble the actual test object better than temperature profiles presented by Milner *et al*,[6] especially the superficial temperature peak. Furthermore, the average image error error for the υ-method and SNR = 100 (δ = 0.27) is markedly smaller than the relative image error (δ = 0.35) reported in the previous study, albeit the previous study was performed on the more accurate computer platform (64-bit workstation). Therefore we conclude that our dedicated algorithms perform better than the algorithm used in their study.

4.5.2 Simulated port-wine stain lesion

The third test object is the temperature profile obtained from a Monte Carlo simulation of optical transport in digitalized histology of port wine stain lesion.[12] This should provide a more realistic estimation of the reconstruction algorithm performance for real port-wine stain PPTR signals.

The temperature profile is represented as a vector $\boldsymbol{T}_0$ with 750 equidistant components (Δz = 2 μm) over a maximum depth of 1.5 mm (Fig. 4.9a). There are 2000 equidistant components (Δt = 1 ms) in PPTR signal vector $\boldsymbol{S}_0$ (Fig. 4.9b) over a 2 s time interval. The assumed tissue constants are $D = 0.11$ mm^2 s^{-1}, μ = 26 mm^{-1}, and $h = 0.02$ mm^{-1}.

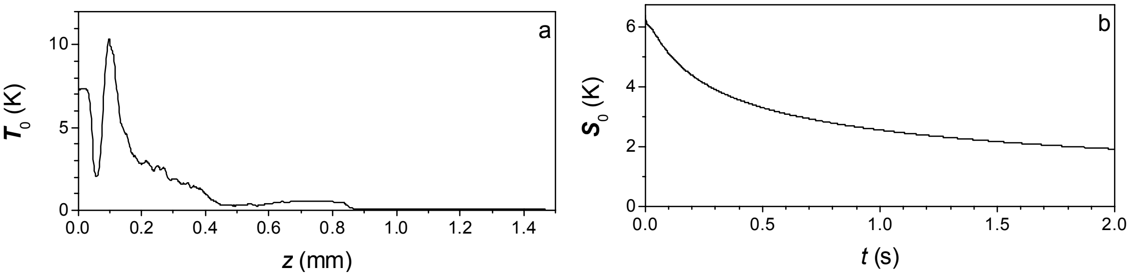

Figure 4.9: (a) Temperature profile $\boldsymbol{T}_0$ and (b) corresponding theoretical PPTR signal $\boldsymbol{S}_0$ for test object MCPWS.

Figure 4.10 shows a statistical analysis of 20 reconstruction results for the MCPWS test object and SNR = 100, 500 and 1000. Similarly to the above example, the reconstruction robustness increases with SNR, most markedly for the υ-method (Fig. 4.10, *bottom row*). At SNR = 100, PRCGLS and PRTSVD produce solutions with more detail than the average solution obtained by the υ-method – likely because of stronger regularization. At SNR = 500 and SNR = 1000, all reconstruction algorithms yield very similar results.

As seen in Figure 4.11, the PR CGLS algorithm results in minimal image errors ($\delta = 0.27 \pm 0.03$ and 0.19 ± 0.02) at SNR = 100 and 1000, while the υ-method is optimal at SNR = 500 ($\delta = 0.22 \pm 0.01$). CGLS and the υ-method also present acceptably small $\delta_{\max}$ (*dashed line*). In contrast, the PR TSVD produces reconstruction results with largest standard deviation of δ ($\sigma_\delta = 0.06$), and largest $\delta_{\max}$.

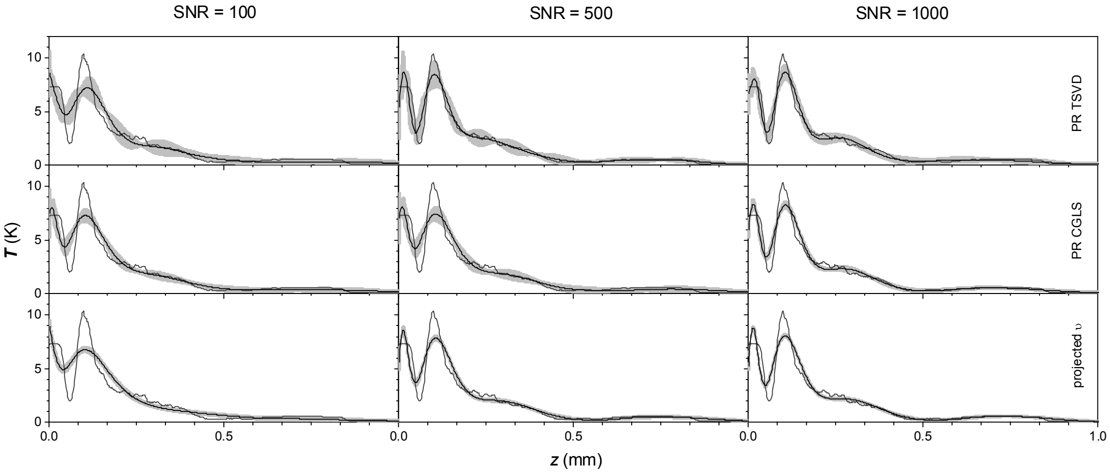

Figure 4.10: Statistical analysis of 20 regularized solutions $\boldsymbol{T}$ for MCPWS test object obtained using the PR TSVD (*top row*), PR CGLS (*middle row*), and projected υ-method (*bottom row*). SNR levels are 100 (*rigt*), 500 (*center*), and 1000 (*left*). The exact solution is presented for comparison (*dark-gray line*). Light-gray bars represent standard deviations.

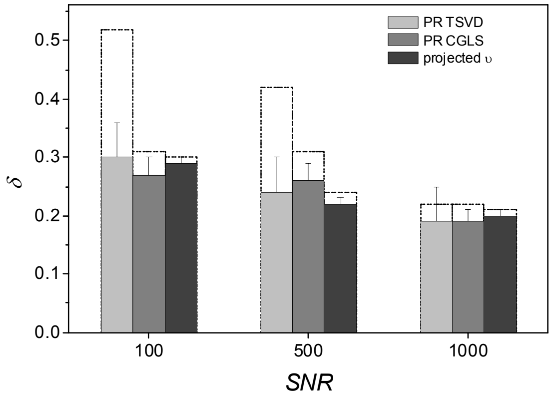

Figure 4.11: Relative image errors δ (Eq. 4.12) of images of MCPWS test object obtained using the PR TSVD (*light-gray bar*), PR CGLS (*gray bars*), and υ-method (*dark-gray bars*). Corresponding maximal obtained image error δ is represented by dashed-line bar.

4.6 Conclusions

Our dedicated reconstruction algorithms with implemented non-negativity constraint and regularization parameter selection method produce markedly more accurate solutions of the PPTR inverse problem than the general-purpose optimization software. Furthermore, our algorithms result in temperature profiles with smaller image errors than temperature profiles presented in an earlier PPTR study and obtained also by a dedicated non-negatively constrained reconstruction algorithm. All three presented algorithms generate similar reconstruction results, but the PR CGLS and projected υ-method yield somewhat smaller image errors and more stable reconstructions as compared to PR TSVD.

Chapter 5

Calibration of radiometric signal

In Chapter 2 we derived the expression for radiometric signal $s(t)$ corresponding to the sample temperature $T_b + \Delta T(z, t)$ (Eq. 2.5). The absolute temperature rise $\Delta T(z, t)$ can not be determined from $s(t)$, unless the exact value of constant C is known. Moreover, (2.5) must be linearized (Eq. 2.6) to obtain the PPTR inverse problem (2.11) which can be solved using the reconstruction algorithms described in Chapter 4. Yet, radiometric signal $s(t)$ does not depend linearly on $\Delta T(z, t)$.

In order to overcome these limitations, it is customary to transform radiometric signals $s(t)$ into radiometric temperature using a calibration process. The calibration eliminates the constant C and reduces the nonlinear dependence of $\Delta T(z, t)$ on $s(t)$, but some error due to linearization of (2.6) may still exist. Therefore, in all reported PPTR studies authors justied utilization of (2.11) only for relatively small temperature rises.[6,9,18] Because moderate temperature changes as compared to T_b can also be observed in temperature profiles reconstructed from PPTR signals measured on PWS birthmarks, we analyze the effect of linearization on the accuracy of reconstructed temperature profiles.

5.1 Linearization error in monochromatic approximation

The calibration process consists of fitting measured PPTR signals to a PPTR setup response to IR radiation emitted by a blackbody set to different temperatures T_{BB}. Here we assume that an IR detector detects emitted IR radiation in a narrow spectral band, thus constant values for wavelength λ, responsivity $R(\lambda)$, IR absorption coefficient μ, and constant C can be used. Such monochromatic approximation is used in almost all reported PPTR studies.

From (2.5), the expression for radiometric signal $s_{BB}(T_{BB})$ due to blackbody radiation at T_{BB} is

$$s_{BB}(T_{BB}) = C\ R(\lambda)\ B_\lambda(T_{BB})\ \Delta\lambda + D \tag{5.1}$$

where D accounts for dark current.

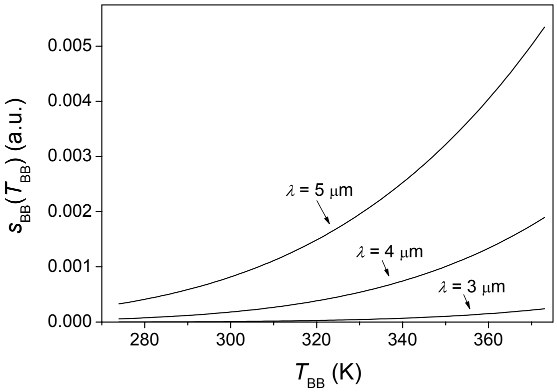

Figure 5.1: Radiometric signal $s_{BB}(T_{BB})$ as a function of blackbody temperature T_{BB} for three acquisition wavelengths λ (*see labels*). The detector responsivity is modeled as $R(\lambda) = R_p\ \lambda/\lambda_p$ with $\lambda_p = 5.0$ μm and $D = 0$.

Figure 5.1 presents blackbody radiometric signals $s_{BB}(T_{BB})$ as a function of T_{BB} for three wavelengths $\lambda = 3.0$, 4.0, and 5.0 μm. The detector responsivity $R(\lambda)$ is modeled as $R(\lambda) = R_p\ \lambda/\lambda_p$ with $\lambda_p = 5.0$ μm.

Linearization of (5.1) at a fixed T_{BB} results in an error, which increases with increasing temperature difference ΔT. So, when temperature is increased by $\Delta T = 20$ K, the expression linearized at $T_{\mathrm{BB}} = 300$ K yields 13% smaller values for $\lambda = 5.0$ µm, and even 24% smaller values for $\lambda = 3.0$ µm (see Fig. 5.1) as compared to the actual value of S_{BB}.

The expression (5.1) is fitted to the measured PPTR setup response to the IR radiation emited by the blackbody, and the constants C and D are determined, thus yielding a calibration curve $s_{\mathrm{BB}}(T)$. When calibrating radiometric signal $s(t)$, the corresponding radiometric temperature $S(t)$ is then found by matching each $s(t_i)$ to the calibration curve $s_{\mathrm{BB}}(T)$

$$s_{\mathrm{BB}}(S(t_i)) = s(t_i) \tag{5.2}$$

Thus the calibration procedure eliminates the constants C and D, and establishes a relation between $s(t)$ and radiometric temperature $S(t)$.

An expression for Planck's law of radiation is

$$B_\lambda(T) = \frac{2\pi hc^2}{\lambda^5\left(\exp(hc/\lambda k_{\mathrm{B}}T)-1\right)} \tag{5.3a}$$

which can be approximated with

$$B_\lambda(T) = \frac{2\pi hc^2}{\lambda^5}e^{-\frac{hc}{\lambda k_{\mathrm{B}}T}} \tag{5.3b}$$

since the exponential in $B_\lambda(T)$ is much larger than 1. Using (5.3b) we find an expression for a monochromatic PPTR signal

$$s(t) = \frac{2\pi C\Delta\lambda\mu R(\lambda)hc^2}{\lambda^5}\int_{z=0}^{\infty} e^{-\frac{hc}{\lambda k_B(T_{\mathrm{b}}+\Delta T(z,t))}-\mu z}\,\mathrm{d}z + D \tag{5.4a}$$

and an expression for the calibration curve

$$s_{BB}(T) = \frac{2\pi C\Delta\lambda R(\lambda)hc^2}{\lambda^5}e^{-\frac{hc}{\lambda k_B T}} + D \tag{5.4a}$$

We substitute (5.4a) and (5.4b) into (5.2) to get the expression for calibrated PPTR signal $s(t)$ in radiometric temperature units

$$\Delta S(t) = -\frac{hc}{\lambda k_{\mathrm{B}}\ln\int_{z=0}^{\infty}\mu\, e^{-\frac{hc}{\lambda k_{\mathrm{B}}(T_{\mathrm{b}}+\Delta T(z,t))}}e^{-\mu z}\,\mathrm{d}z} - T_{\mathrm{b}} \tag{5.5}$$

The calibration process eliminates the constant factor $2\pi C\Delta\lambda hc^2R(\lambda)$ and constant D. We expand the expression for $\Delta S(t)$ into Taylor series and neglect terms of the order $\Delta T(z, t)^2$ and higher, which results in a linearized expression for the PPTR signal

$$\Delta S_{\mathrm{L}}(t) = \mu\int_{z=0}^{\infty}\Delta T(z,t)\,e^{-\mu z}\,\mathrm{d}z \tag{5.6}$$

All factors involving λ and T_{b} are canceled in (5.6), so that the linearized calibrated signal $\Delta S_{\mathrm{L}}(t)$ depends on acquisition wavelength λ only indirectly, through the value μ.

We can estimate the linearization error by considering the quadratic term in Taylor series

$$N_2\left(\Delta T(z,t)\right) = \frac{1}{T_\mathrm{b}}\left(\frac{hc}{2\lambda k_\mathrm{B} T_\mathrm{b}} - 1\right) \times$$
$$\times \left\{ \mu \int_{z=0}^{\infty} \Delta T(z,t)^2 \, e^{-\mu z} \, \mathrm{d}z - \left(\mu \int_{z=0}^{\infty} \Delta T(z,t) \, e^{-\mu z} \, \mathrm{d}z \right)^2 \right\} \tag{5.7}$$

Assuming that $N_2(\Delta T(z, t))$ (5.7) is the largest contribution to the linearization error, we find an expression for the relative linearization error. First, we write the temperature rise as $\Delta T(z, t) = T_\mathrm{av} f(z, t)$, where T_av is average temperature rise and $f(z, t)$ is a normalized form function in the sense $\mu \int_{z=0}^{\infty} f(z,t)\, e^{-\mu z} \, \mathrm{d}z = 1$. Second, we divide (5.7) by (5.6) to obtain

$$\frac{N_2\left(\Delta T(z,t)\right)}{\Delta S_\mathrm{L}(t)} = \frac{T_\mathrm{av}}{T_\mathrm{b}}\left(\frac{hc}{2\lambda k_\mathrm{B} T_\mathrm{b}} - 1\right)\left[\mu \int_{z=0}^{\infty} f^2(z,t) e^{-\mu z} \, \mathrm{d}z - 1\right] \tag{5.8}$$

Evidently, the linearization error increases proportionally with T_av. Furthermore, the error increases with decreasing T_b and λ.

The above expression shows that for a sample with constant temperature T (i.e., $f(z, t) = 1$) the linearization error is zero; which indicates that the linearized expression $\Delta S_\mathrm{L}(t)$ is exact for homogenously heated samples. However, for non-homogenously heated samples (i.e., $f(z, t) \neq 0$) the linearization error persist in spite of optimal calibration. For example, we evaluate (5.8) for a Gaussian initial temperature profile $\Delta T(z) = T_0 \exp(-(z - z_0)^2/2w^2)$ with $T_0 = 20$ K, $z_0 = 100$ µm, and $w = 30$ µm for $\lambda = 3$ and 5 µm. Absorption coefficient $\mu = 26.5$ µm. Thus, we obtain the linearization error $N_2/\Delta S_\mathrm{L} = 20\%$ and 11% for $\lambda = 3$ and 5 µm, respectively. These errors are smaller than the corresponding errors for non-calibrated linearized radiometric signal (see Fig. 5.1). Since PPTR signal involves transient temperature rise $\Delta T(z, t)$, we perform a numerical simulation to consider evolution of the linearization error with time.

5.1.1 Numerical simulation

The initial temperature profiles have a hyper-Gaussian form: $\Delta T(z,0) = T_\mathrm{p} \exp[-2(z-z_0)^4/w^4]$ with $T_\mathrm{p} = 1 - 100$ K, $w = 30$ µm, and central depths $z_0 = 100$, 200, and 300 µm. The temperature profile $\Delta T(z', t)$ at depth z' and time t is calculated as a convolution of $\Delta T(z, 0)$ and the Green's function $G_\mathrm{T}(z, z', t)$ (Eq. 2.3). Then, $\Delta S(t)$ and $\Delta S_\mathrm{L}(t)$ are calculated by inserting $\Delta T(z, t)$ into (5.5) and (5.6) and completing the z integrals. We use numerical integration routines implemented in Mathematica 4.1 (Wolfram research, Champaign, IL) to compute signal vectors with 1000 components representing signal values acquired at a sampling rate 1000 s^{-1} for a total acquisition time of 1s. PPTR signals are simulated for $\lambda = 4.5$ µm, $\mu = 26.5$ mm^{-1}, and $T_\mathrm{b} = 303$ K. Thermal constants in $G_\mathrm{T}(z, z', t)$ are $D = 0.11$ mm^2/s and $h = 0.02$ mm^{-1}.

Figure 5.2 presents PPTR signals calculated using the exact (*solid line*) and the linearized (*dashed line*) expressions for test objects with $z_0 = 100$ µm and $T_\mathrm{p} = 1$, 10, and 100 K (*see the labels*). For $T_\mathrm{p} = 100$ K, the exact signal features an initial spike (*see the arrow*), which is not present in the linearized signal. This difference between the simulated signals appears only at small times ($t < 20$ ms); while both signals are equal at later times. For the lower T_p (1 and 10 K), both signals are equal at al t.

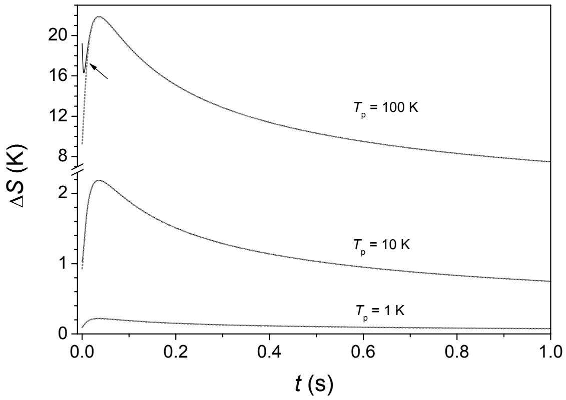

Figure 5.2: Theoretical calibrated PPTR signals for hyper-Gaussian test objects with z_0 = 100 µm, and T_p = 1, 10, and 100 K (*see labels*). The exact $\Delta S(t)$ (Eq. 5.5; *solid line*) and linearized PPTR signals $\Delta S_L(t)$ (Eq. 5.6; *dashed line*) are presented.

In order to find how the linearization error affects temperature profiles, we simulate the exact PPTR signals (Eq. 5.5). Then we reconstruct initial temperature profiles $\Delta T(z, 0)$ from these signals using the linearized expression for PPTR signal (Eq. 2.11) and the monochromatic approximation (Eq. 2.9). The reconstruction algorithm used is the υ-method (chapter 4). We simulate PPTR signals for test objects located at z_0 = 100 µm with T_p = 1–100 K, and test objects with T_p = 50 K located at z_0 = 100-300 µm. Figure 5.3 presents the reconstructed temperature profiles (*solid line*) and the actual test objects (*dashed line*) for comparison.

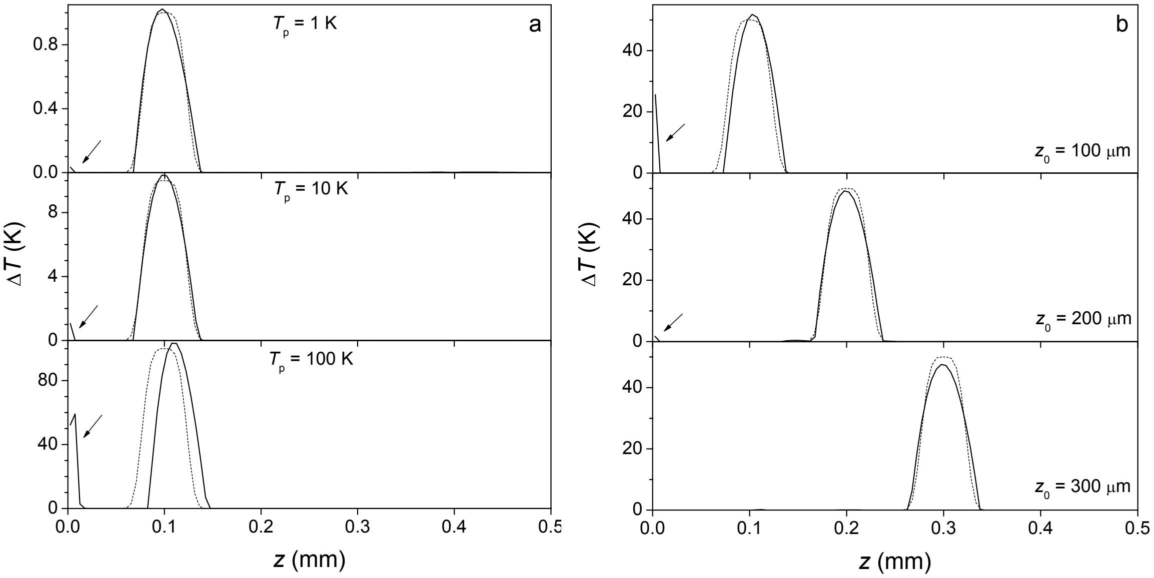

Figure 5.3: Reconstructed temperature profiles ΔT obtained from the exact PPTR signals $\Delta S(t)$ for (a) test objects located at z_0 = 100 µm with T_p = 1–100 K (*see labels*), and (b) test objects located at z_0 = 100–300 µm with T_p = 50 K (*see labels*). The actual objects (*dashed line*) are plotted for comparison. Arrows indicate surface artifacts due to the linearization error.

When reconstructed test object is located at z_0 = 100 µm (Fig. 5.3a), the reconstruction results are not significantly deteriorated for T_p = 1 and 10 K, but we can observe a small artifact near the object surface (*see the arrows*). In contrast, reconstruction of test object with T_p = 100 K (*bottom*) results in a severely deformed temperature profile, and a significant surface artifact. Moreover, the temperature profile is shifted deeper as compared to original depth (z_0 = 100 µm).

The effect of linearization error is reduced as z_0 increases (Fig. 5.3b). The distinct surface artifact in reconstructed temperature profile of test object with z_0 = 100 μm (*top*) and T_p = 50 K, diminishes as z_0 is increased to 200 μm (*center*), and disappears for z_0 = 300 μm (*bottom*). The shift of temperature peak (~3 μm) is also present only for the temperature profile located at z_0 = 100 μm.

Occasionally, we observe such initial spikes in measured PPTR signals. Because the temperature profile reconstruction is performed using the linearized expression (5.6), superficial artifacts due to the linearization error can appear in reconstructed temperature profiles, especially when large temperature amplitudes are involved.

In addition to the above reconstruction results, we present a systematic analysis of the linearization error. Figure 5.4 shows the normalized linearization error defined as $(\Delta S(t) - \Delta S_L(t))/\langle\Delta S(t)\rangle$ for all simulated hyper-Gaussian test objects. In general, the normalized linearization error increases with increasing T_p. However, the error practically vanishes in 10–100 ms for all depths z_0 and temperatures T_p. Specifically, for T_p = 100 K the linearization error is reduced below 1% in 20 ms and 46 ms for z_0 = 100 and 200 μm, respectively. The linearization errors for the test objects with z_0 = 300 μm feature peak values at t = 40–50 ms, but are significantly smaller than for z_0 = 100 and 200 μm.

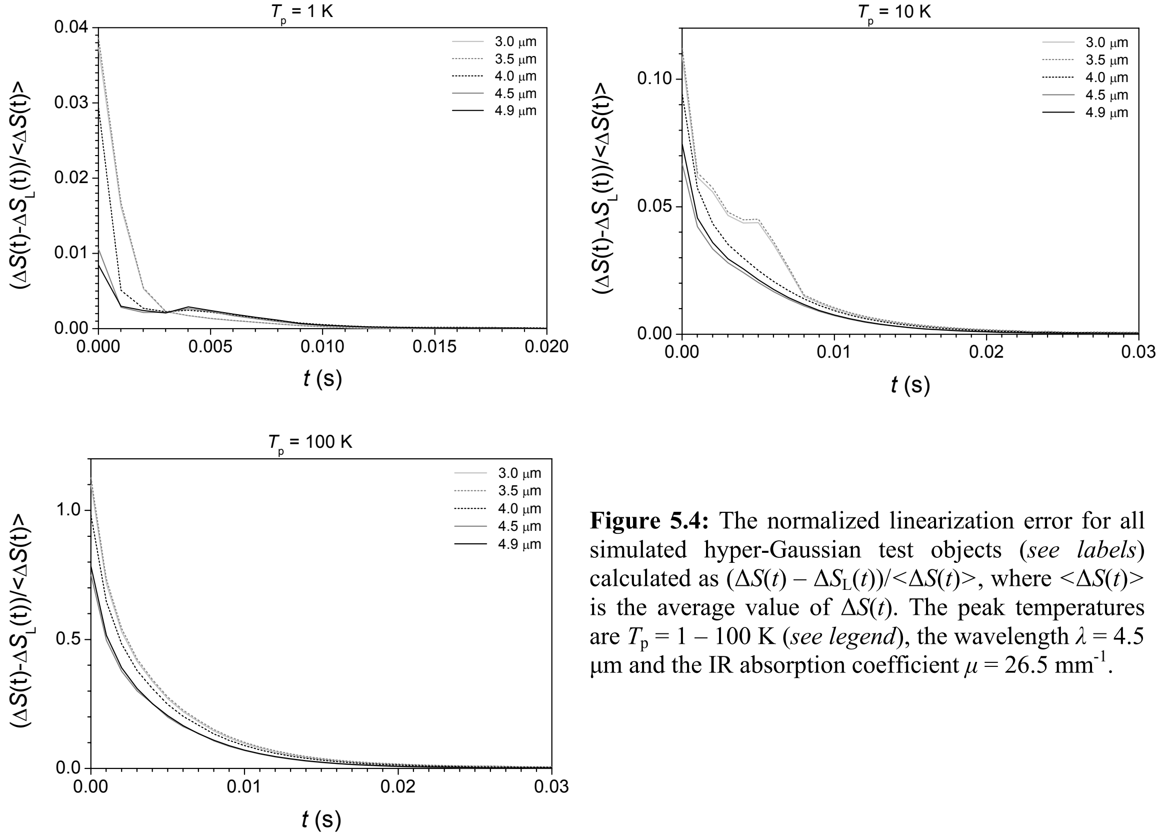

Figure 5.4: The normalized linearization error for all simulated hyper-Gaussian test objects (*see labels*) calculated as $(\Delta S(t) - \Delta S_L(t))/\langle\Delta S(t)\rangle$, where $\langle\Delta S(t)\rangle$ is the average value of $\Delta S(t)$. The peak temperatures are T_p = 1 – 100 K (*see legend*), the wavelength λ = 4.5 μm and the IR absorption coefficient μ = 26.5 mm^{-1}.

5.2 Broad-band signal acquisition

Since the monochromatic calibration is accurate only for very narrow spectral bands,[18,47] we analyze next the calibration process involving broadband signal acquisition. From (2.5), radiometric signal due to blackbody radiation at T_{BB} is

$$s_{BB}(T_{BB}) = C \int_{\lambda_l}^{\lambda_h} R(\lambda)\, B_\lambda(T_{BB})\, d\lambda + D \qquad (5.9)$$

where λ_l and λ_h are the lower and the upper limit wavelengths, respectively. Analogous to the monochromatic calibration, the expression (5.9) is fitted to the measured broad-band PPTR setup response to the IR radiation emited by the blackbody, and the constants C and D are determined, thus yielding a broad-band calibration curve $s_{BB}(T)$. The broad-band radiometric temperature $S(t)$ is then found by matching each $s(t_i)$ to the calibration curve $s_{BB}(T)$ according to (5.2). By using the Taylor series expansion, the linearized expression for the calibrated spectrally composite PPTR signal is

$$\Delta S_L(t) = \int_{\lambda_l}^{\lambda_h} R(\lambda)\, B_\lambda'(T_b)\, \mu(\lambda) \int_{z=0}^{\infty} \Delta T(z,t)\, e^{-\mu(\lambda)z}\, dz\, d\lambda \Bigg/ \int_{\lambda_l}^{\lambda_h} R(\lambda)\, B_\lambda'(T_b)\, d\lambda \qquad (5.10)$$

With broad-band signal acquisition, the factors involving specific spectral properties (i.e., $R(\lambda)$, $B_\lambda'(T_b)$, $\mu(\lambda)$) and T_b do not cancel out in the linearized calibrated PPTR signal $\Delta S_L(t)$ (5.12). Because we can not derive the linearization in the spectrally composite PPTR signals $\Delta S(t)$ analytically, we perform a numerical simulation.

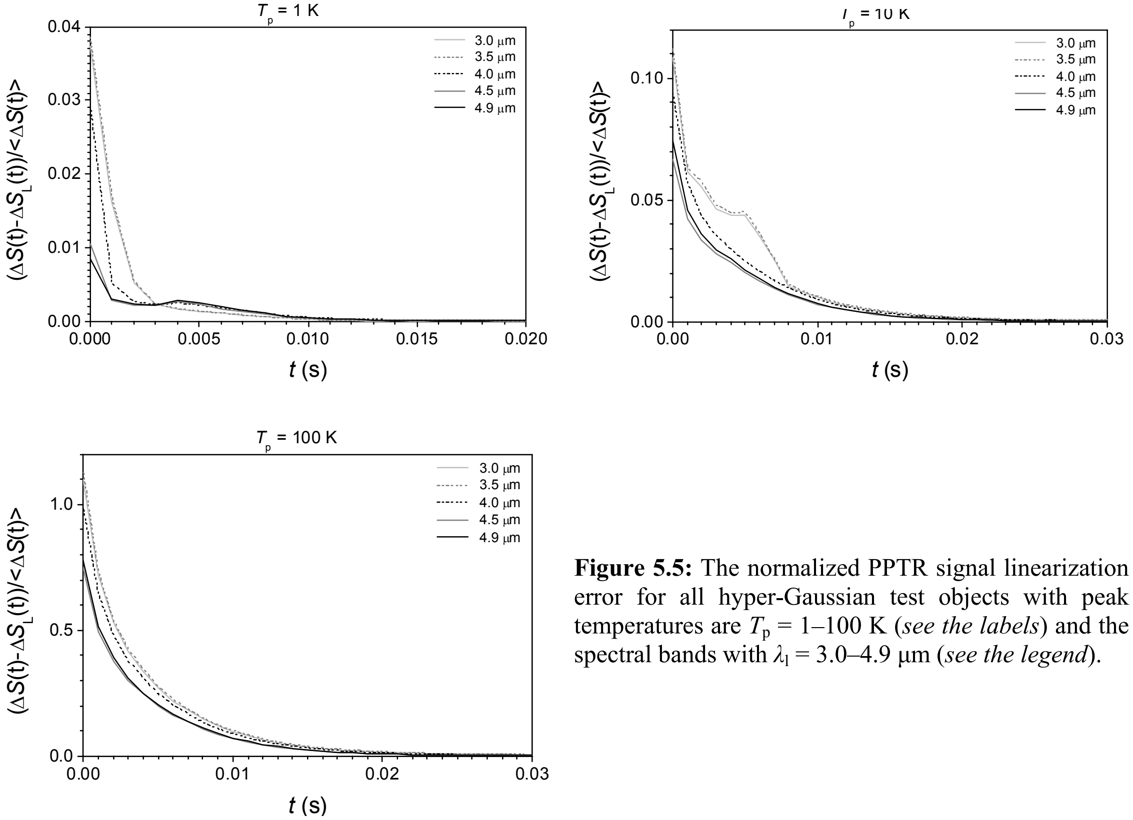

Figure 5.5: The normalized PPTR signal linearization error for all hyper-Gaussian test objects with peak temperatures are T_p = 1–100 K (*see the labels*) and the spectral bands with λ_l = 3.0–4.9 μm (*see the legend*).

Figure 5.5 present the obtained relative linearization errors calculated as in subsection 5.1.1. Similarly to the monochromatic case, the linearization error practically vanishes in 20–30 ms, and increases with the temperature amplitude T_p for all spectral bands. In addition, the linearization error progressively decreases, when the spectral acquisition band is reduced from λ_l = 3.0–5.0 μm to λ_l = 4.9–5.0 μm.

The initial temperature profiles $\Delta T(z, 0)$ have a hyper-Gaussian form, as in subsection 5.1.1. The profile central depth is fixed at z_0 =100 μm, where the monochromatic linearization error was found to be largest. Detector spectral responsivity is modeled as $R(\lambda) = R_p\ \lambda/\lambda_p$, and the IR absorption coefficient $\mu(\lambda)$ is modeled as 75% of the values for water[48] sampled with spectral interval of 0.1 μm.

The exact spectrally composite PPTR signals $\Delta S(t)$ are computed in three steps. First, the radiometric signal $s(t)$ is found by completion of the z and λ integrals (Eq. 2.5). Second, the blackbody radiometric signal $\Delta s_{BB}(T_{BB})$ is determined for T_{BB} = 273–373 K by completion of the λ integral (Eq. 5.9). Finally, $\Delta S(t)$ is calculated by fitting $s(t_i)$ to the calibration curve $s_{BB}(T)$ (Eq. 5.2) at each time $t_i = i\ \Delta t$.

Meanwhile, the corresponding linearized spectrally composite PPTR signal $\Delta S_L(t)$ is computed by completion of the z and λ integrals in (5.10). All computations were performed using Mathematica 4.1.

Table 5.1 lists the maximum linearization error and the time $t_{1\%}$, when the linearization error drops below 1% of the maximum value for the entire-spectral band of the InSb detector (λ = 3.0–5.0 μm) and a reduced spectral band (λ = 4.5–5.0 μm).[18,49] Maximal linearization error for λ_l = 3.0 μm is on average 50% larger than the corresponding error for λ_l = 4.5 μm. $t_{1\%}$ increases with T_p, and is smaller for λ_l = 4.5 μm than for λ_l = 3.0 μm.

Table 5.1: Maximal normalized linearization error $(\Delta S(t) - \Delta S_L(t))/<\Delta S(t)>$ and time $t_{1\%}$, when the linearization error drops below 1% of the maximum. Results are presented for spectral bands with λ_l = 3.0 μm and 4.5 μm, and for the monochromatic PPTR signals with λ = 4.5 μm and z_0 = 100 μm (Fig. 5.5).

	λ = 3.0–5.0 μm		λ = 4.5–5.0 μm	
T_0 (K)	Error	$t_{1\%}$ (ms)	Error	$t_{1\%}$ (ms)
1	0.04	1	0.01	0
2	0.05	2	0.03	1
5	0.06	3	0.03	2
10	0.11	8	0.07	6
20	0.15	13	0.13	9
50	0.52	16	0.35	14
100	1.10	20	0.75	16

5.3 Conclusions

All nonlinearity between the radiometric signal and the radiometric temperature is eliminated, when a calibration in monochromatic approximation is performed. In linearized calibrated PPTR signals the factors involving the acquisition wavelength (i.e., $B_\lambda(T_b)$ and $R(\lambda)$) cancel out from the resulting expression. The linearized expression is exact for samples with homogenous temperature distribution, but for samples with non-homogenous temperature distribution the linearization produces a linearization error.

In general, the linearization error is significant for absorbing structures located at shallow depths and short after laser pulse. The error increases with increasing peak temperature, which is predicted by the analytical expression (5.8). This expression also indicates that linearization error decreases with increasing acquisition wavelength λ and baseline temperature T_b.

Due to the linearization error we can observe in reconstructed temperature profiles superficial artifacts, which can be easily mistaken for superficial absorbing structures.

Same trends are obtained for the spectrally composite calibrated PPTR signals. In addition, we observe also that the linearization error increases with spectral acquisition band broadening.

Since temperature amplitudes are in general moderate, and most of absorbing structures (i.e., blood vessels) are deeper in the sample, the linearization error in typical PPTR temperature profiling in human skin is small. The error can be additionally reduced by appropriate spectral filtering.

Chapter 6

Effective infrared absorption coefficient

Reconstruction of temperature profiles from PPTR signals involves tissue absorption coefficient at the detected IR wavelength, $\mu(\lambda)$. In general, soft biological tissues feature a pronounced spectral variation $\mu(\lambda)$ in mid-IR. Yet, all reported PPTR studies utilized a fixed effective value (μ_{eff}) to reduce computational complexity of the reconstruction process, albeit broad-band signal acquisition was used almost invariably to increase signal-to-noise ratio (SNR). In earlier PPTR studies two approaches of analytical estimation of μ_{eff} were presented,[6,9] but no study has been done to find which approach is better. However, implications of monochromatic approximation for PPTR temperature profiling were analyzed numerically for specific case of two spectral bands of an InSb detector.[18]

In this chapter, we focus on determination of the optimal effective value μ_{eff} for samples that exhibit a significant spectral variation $\mu(\lambda)$ within the IR detection band. Taking into account spectral characteristics of three common IR radiation detectors, we simulate realistic PPTR signals for four hyper-Gaussian temperature profiles centered at different depths below the sample surface. From each PPTR signal, the initial temperature profile is then reconstructed using the approximation with a constant μ_{eff}. Analysis of the mismatch between the actual and reconstructed temperature profiles at different values μ_{eff} enables determination of the optimal effective value, μ_{opt}.

Because determination of μ_{opt} from numerical simulations is very tedious, we propose a novel analytical approach to the same task. Based on an implicit equation derived earlier[11,18], this approach enables a direct estimation of μ_{opt} from spectral properties of the sample and radiation detector. In a systematic analysis, involving multiple acquisition spectral bands for each IR radiation detector, our analytically assessed values μ_{opt} match the numerical results very well, unlike the previously used analytical estimates.[6,9]

6.1 InSb detector

6.1.1 Numerical simulation

All initial temperature profiles ("objects") in our simulation examples have a hyper-Gaussian form: $\Delta T(z,0) = \Delta T_0 \exp[-2\,(z-z_0)^4/w^4]$ with $\Delta T_0 = 10$ K and $w = 0.1$ mm. With z_0 varied from 0.1 to 0.4 mm, these profiles represent laser-induced temperature rise in subsurface vascular plexus (such as PWS) at different depths in skin. The corresponding vectors $\boldsymbol{T}_0$ represent temperature values at 100 equidistant positions over a depth of 1 mm.

Each vector $\boldsymbol{S}_0$ has 1000 components, representing signal values acquired at a sampling rate of 1000 s^{-1} (for a total acquisition time of 1 s). It is obtained by multiplying $\boldsymbol{T}_0$ with a spectrally composite matrix $\boldsymbol{K}$. Based on (2.7) and (5.10), each matrix element of the latter is computed as a sum of $N = 100$ monochromatic kernel functions $\kappa(z, t)$ (Eq. 2.10) evaluated at equidistant wavelengths λ_k within the spectral acquisition band λ_l–λ_h

$$K(z_i,t_j) = \frac{\sum_{k=1}^{N} R(\lambda_k)\, B_{\lambda_k}'(T_{\mathrm{b}})\ \mu(\lambda_k)\ \kappa\left[z_i, t_j, \mu(\lambda_k)\right]\ \Delta z}{\sum_{k=1}^{N} R(\lambda_k)\, B_{\lambda_k}'(T_{\mathrm{b}})} \tag{6.1}$$

where Δz denotes depth discretization. The absorption spectrum of human skin is modeled by adding 75% of $\mu(\lambda)$ for water[48] and 25% of $\mu(\lambda)$ for collagen[51] (Fig. 6.1a). The thermal constants in $\kappa(z,t)$ are set to[52] $D = 1.1 \times 10^{-7}$ m^{2}s^{-1} and $h = 0.02$ mm^{-1}.

InSb quantum radiation detector has peak sensitivity wavelength of $\lambda_p = 5.3$ μm and cut-off at $\lambda_c = 5.6$ μm. The corresponding spectral responsivity $R(\lambda)$ is modeled as increasing linearly with λ up to λ_p, then linearly decreasing to 10% of the maximal value at λ_c (Fig. 6.1b). The lower spectral limit (λ_l) is varied between 3.0 μm and λ_p, while λ_h is fixed at the respective λ_c. This simulates application of different cut-on filters to narrow the detection spectral band[18,50]. No noise is added to the simulated signals, because it would induce inconsistencies in the analysis.

From each signal vector, the initial temperature profile is reconstructed using a range of simplified kernel matrices based on (2.9) and employing different effective values μ_{eff}. We apply the PR-CG method (chapter 4) to solve the inverse problem (2.11). The minimum in dependence of relative image error δ (4.10) on μ_{eff} indicates the optimal effective value (μ_{opt}) for a given combination of object, detector and acquisition spectral band.

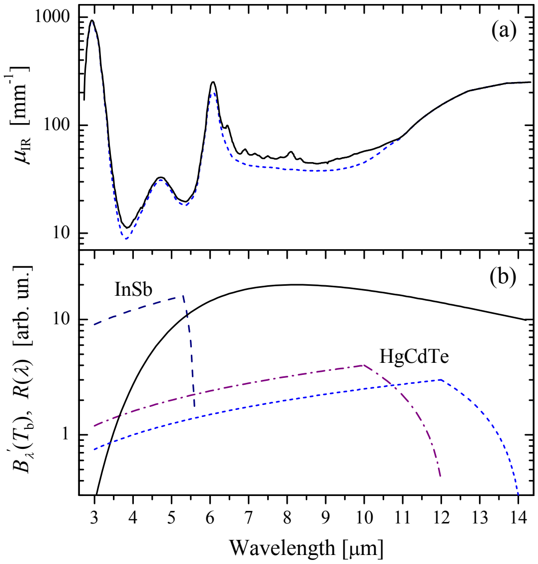

Figure 6.1: (a) Model absorption coefficient of skin in mid-IR spectral region, μ (*solid line*), computed as 75% of μ for water[48] (*short dash*) increased by 25% of μ for collagen[51]. (b) Temperature derivative of Planck's radiation formula at $T_b = 300$ K (*solid line*) and spectral sensitivity $R(\lambda)$ of a typical InSb detector (*dashed line*), and two HgCdTe detectors with peak sensitivity at 10 μm and 12 μm (*dash-dot* and *short-dash line*, respectively).

Figure 6.2 presents three results, obtained from a simulated PPTR signal for the hyper-Gaussian object centered at $z_0 = 0.3$ mm (*dashed line*) and employing the entire acquisition spectral band of the InSb detector (3.0–5.6 μm). Reconstructions were performed using the simplified, quasi-monochromatic kernel matrices based on (2.9) with varying μ_{eff}. At a sub-optimal value ($\mu_{\text{eff}} = 20.0$ mm^{-1}, *top graph*), the tails of the profile are squeezed and peak temperature is markedly overshot. The best match is obtained with $\mu_{\text{eff}} = 22.3$ mm^{-1} (*center*), while an overestimated value ($\mu_{\text{eff}} = 25.0$ mm^{-1}, *bottom*) results in a narrowed peak with blurred tails.

Figure 6.3 presents the dependence of relative image error δ (Eq. 4.10) on μ_{eff}, as obtained for four hyper-Gaussian profiles centered at different depths z_0 (see labels in the graphs). The optimal μ_{eff} for each object is indicated by the minimum of the respective dependence (arrows). The results in Fig. 6.3a represent the case where the entire spectral band of the InSb detector is used. With a narrowed acquisition spectral band ($\lambda_l = 4.5$ μm; Fig. 6.3b), the four optimal values $\mu_{\text{opt}}(z_0)$ lie closer together and the respective image errors are significantly smaller.

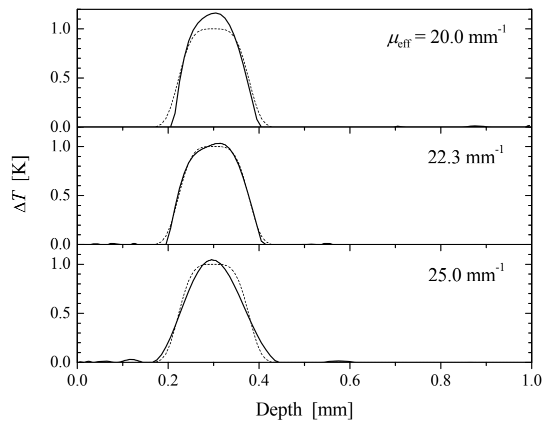

Figure 6.2: Temperature depth profiles (*solid lines*) reconstructed from simulated PPTR signal employing the entire spectral band of the InSb detector (3.0–5.6 μm). The values of μ_{eff} used in reconstruction were, respectively, too low (*top*), near-optimal (*center*), and too high (*bottom; values indicated in the graphs*). The initial temperature profile is plotted for comparison (*dashed line*).

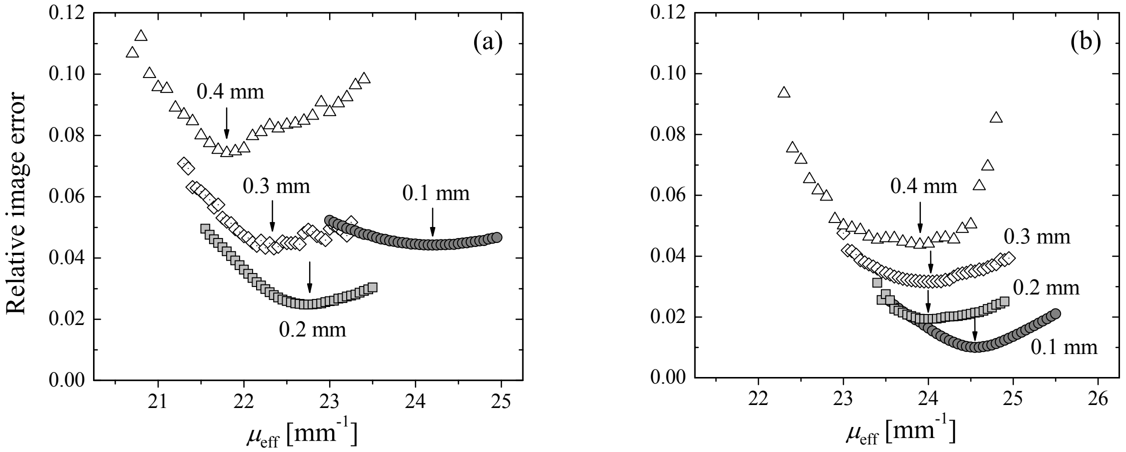

Figure 6.3: Relative image error (δ) as a function of μ_{eff} used for reconstructions of spectrally composite PPTR signals with acquisition band of: (a) 3.0–5.6 μm, and (b) 4.5–5.6 μm. Different symbols represent the results obtained for objects centered at different depths z_0 (indicated in the graphs); arrows indicate the optimal values for each object, $\mu_{opt}(z_0)$.

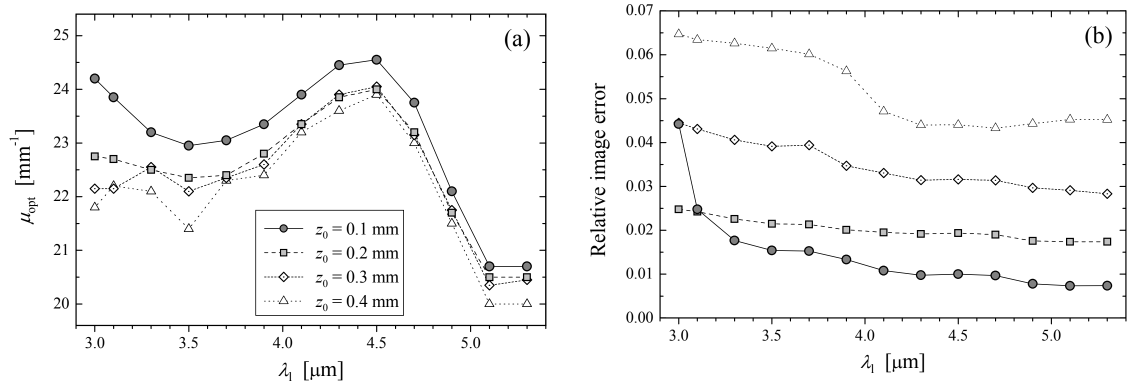

Figure 6.4: (a) Optimal effective absorption coefficient $\mu_{opt}(z_0)$ for objects centered at different depths z_0 (see the legend) as a function of lower spectral limit λ_l. The upper limit is fixed at λ_h = 5.6 μm. (b) Relative image errors (δ) for the reconstruction results from figure 6.4a.

The results from such analyses with the lower limit wavelength λ_l varied from 3.0 to 5.3 μm are collected in Fig. 6.4. The optimal effective values $\mu_{\text{opt}}(z_0)$ vary with λ_l, as dictated by spectral dependences $\mu(\lambda)$, $R(\lambda)$, and $B_\lambda'(T_b)$ in the respective acquisition bands (Fig. 6.4a). At the same time, the spread of values $\mu_{\text{opt}}(z_0)$ obtained for the four test objects diminishes with increasing λ_l. Relative image errors (δ) for the same reconstruction results show a general trend of decreasing with increasing λ_l for all four test objects (Fig. 6.4b).

6.1.2 Analytical approach

Our approach to determine the optimal effective value μ_{eff} directly from sample IR absorption spectrum $\mu(\lambda)$, detector spectral sensitivity $R(\lambda)$, and acquisition spectral band (λ_l, λ_h), is based on relation[18]

$$\mu_{\text{eff}}\; e^{-\mu_{\text{eff}}\, z} = \int_{\lambda_l}^{\lambda_h} R(\lambda)\, B_\lambda'(T_b)\, \mu(\lambda)\, e^{-\mu(\lambda) z}\, \mathrm{d}\lambda \Bigg/ \int_{\lambda_l}^{\lambda_h} R(\lambda)\, B_\lambda'(T_b)\, \mathrm{d}\lambda \tag{6.2}$$

This implicit equation is obtained by substituting $\mu(\lambda)$ in (2.6) with a spectrally constant value μ_{eff} and requiring that the obtained expression equals the r.h.s. of (2.6) for abritrary $\Delta T(z,t)$.

We begin by evaluating the first integral on the r.h.s. of (6.2) at 500 equidistant depths z_i (from 0.001 to 0.500 mm) using Simpson's rule[32]. For each z_i, equation (6.2) is then solved for μ_{eff} using the Jacobi iterative method. The solution $\mu_{\text{eff}}(z)$ is in general double-valued and varies with depth z (see Fig. 6.5). This demonstrates that a single value μ_{eff}, which could replace spectrally variable $\mu(\lambda)$ to yield the correct kernel function, does not exist. The optimal effective value, providing the closest approximation to the augmented kernel function is therefore determined from $\mu_{\text{eff}}(z)$ in the following manner.

After selecting a reasonable starting approximation, $\mu_{\text{opt}}^{(0)}$, we calculate a weighted average

$$\mu_{\text{opt}} = \frac{\sum_i \mu_{\text{eff}}(z_i)\; \mathrm{e}^{-\mu_{\text{eff}}(z_i) z_i}}{\sum_i \mathrm{e}^{-\mu_{\text{eff}}(z_i) z_i}} \tag{6.3}$$

In computing both sums, only the value $\mu_{\text{eff}}(z_i)$ from the solution branch that is closer to $\mu_{\text{opt}}^{(0)}$ is considered at each depth z_i. Using the obtained value, $\mu_{\text{opt}}^{(1)}$, as improved approximation, the procedure is then repeated in the same manner. The successive approximations $\mu_{\text{opt}}^{(m)}$ converge toward the optimal effective absorption coefficient, μ_{opt}.

The exponential weight function, $\exp[-\mu_{\text{eff}}(z)\, z]$, was selected because the contribution of emitters from various depths z to the radiometric signal (Eq. 2.6) at any time t is governed by Beer's law. After figuring out how to deal with the obtained relation (Eq. 6.2) involving the two-valued function $\mu_{\text{eff}}(z)$, everything fell into place.

Figure 6.5 presents solutions $\mu_{\text{eff}}(z)$ of the implicit Eq. (6.2) for four acquisition spectral bands of the InSb detector (see the caption). The variation of μ_{eff} with depth (z) is most prominent for the widest acquisition band (Fig. 6.5a), and almost absent in the nearly monochromatic case (Fig. 6.5d). The dashed lines indicate the corresponding optimal values μ_{opt} assessed using our analytical approach (Eq. 6.2). For the four presented examples they amount to 23.0 mm^{-1}, 23.2 mm^{-1}, 24.5 mm^{-1}, and 20.7 mm^{-1}, respectively. It may seem odd that the optimal μ_{eff} depends also on the object depth, z_0. But this is just a reminder that no constant value μ_{eff} used in Eq. (2.9) can entirely replicate the effect of the spectrally composite $K(z,t)$ (2.8).

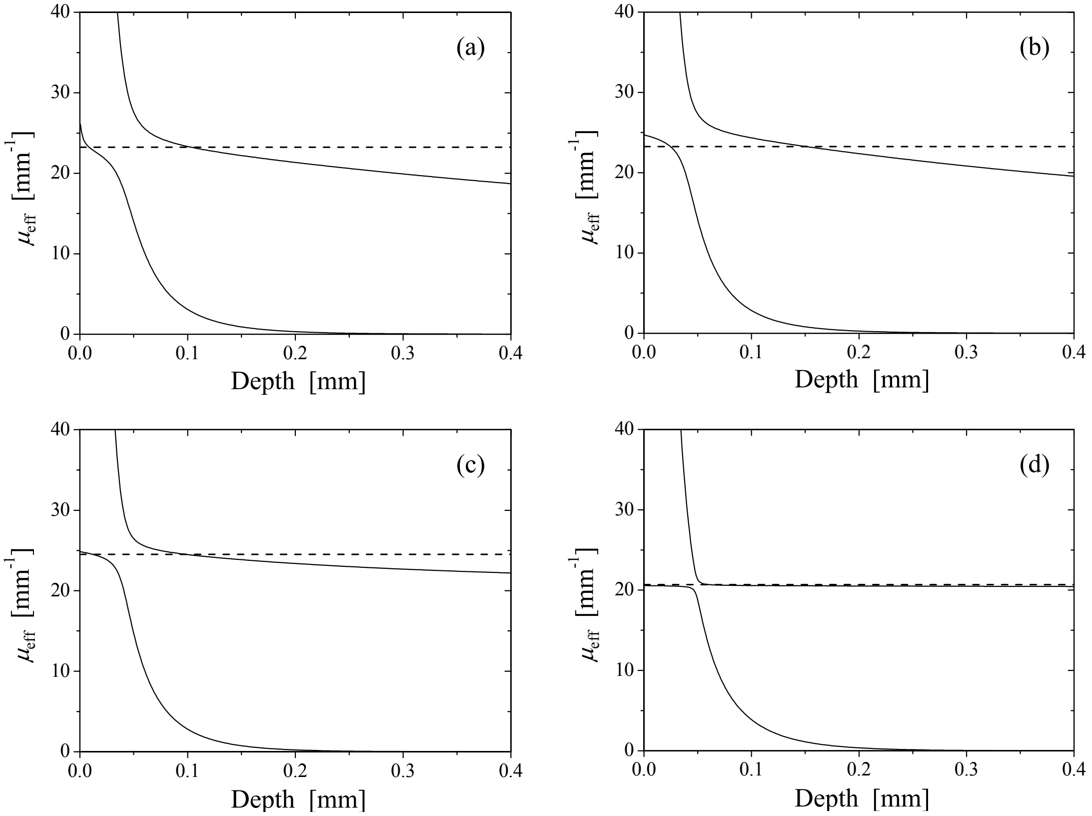

Figure 6.5: Effective absorption coefficient $\mu_{\rm eff}(z)$ (Eq. 6.2) computed for InSb detector and detection band of: (a) 3.0–5.6 μm, (b) 3.9–5.6 μm, (c) 4.5–5.6 μm, and (d) 5.1–5.6 μm. Dashed lines indicate the corresponding values $\mu_{\rm opt}$ determined using Eq. (6.3).

Figure 6.6 presents the analytically assessed optimal values, $\mu_{\rm opt}$ (Eq. 6.3), as a function of the lower limit wavelength, $\lambda_{\rm l}$ (solid line). For all included values $\lambda_{\rm l}$, the analytical estimate falls within the range of values $\mu_{\rm opt}(z_0)$ obtained for the four test objects in numerical simulations (grey vertical stripes). Difference between the arithmetic mean of the latter (open circles) and $\mu_{\rm opt}$ (Eq. 6.3) does not exceed 0.6 mm^{-1} for any spectral band under test. For the most important case, employing the entire spectral band of the InSb detector ($\lambda_{\rm l}$ = 3.0 μm), the difference is only 0.25 mm^{-1} or 1.1% of the target value.

For objective PPTR profiling of arbitrary samples, one would namely wish to obtain equally good performance at all subsurface depths. In reality, however, images of deeper objects are increasingly blurred due to higher susceptibility to experimental noise (chapters 7 and 11). To account for this, we consider also a weighted average which favors shallower test objects (black squares). The weight z_0^{-1} was selected because it approximates scaling of the PPTR signal amplitude from a thin subsurface layer.[9] By considering a weighted average of $\mu_{\rm opt}(z_0)$ at each $\lambda_{\rm l}$, $\mu_{\rm opt}$ (Eq. 6.3) falls within 0.3 mm^{-1} off the mark for all detection bands included in the analysis.

Two formerly applied analytical estimates perform significantly worse in such a comparison. The weighted average of $\mu(\lambda)$ with the weight set to $R(\lambda)$[53,9] amounts to 62.3 mm^{-1} in the most relevant case of $\lambda_{\rm l}$ = 3.0 μm, overshooting the average of numerical values $\mu_{\rm opt}(z_0)$ by 174% (Fig. 6.6, short-dash line). The more elaborate expression used by Milner *et al*[6,7]

$$\tilde{\mu}_{\rm eff} = \int_{\lambda_{\rm l}}^{\lambda_{\rm h}} R(\lambda)\, B_\lambda'(T_{\rm b})\, \mu(\lambda)\, {\rm d}\lambda \Bigg/ \int_{\lambda_{\rm l}}^{\lambda_{\rm h}} R(\lambda)\, B_\lambda'(T_{\rm b})\, {\rm d}\lambda \tag{6.4}$$

provides a better match to the numerical data (dash-dot line). Nevertheless, it exceeds the optimal value for unfiltered InSb detector by a significant margin of 2.4 mm^{-1} (or 13%).

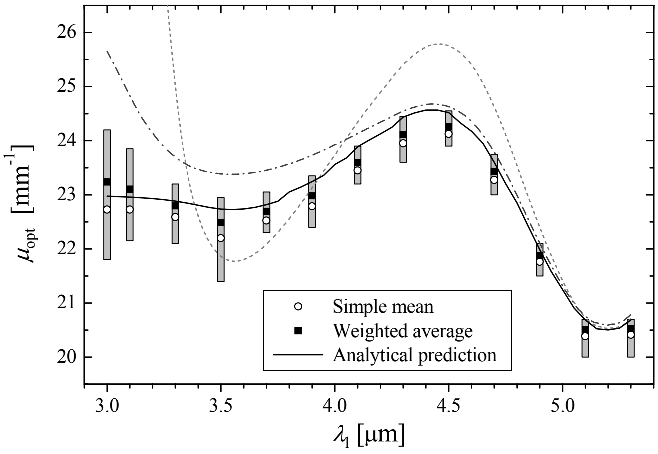

Figure 6.6: Analytically assessed values μ_{opt} as a function of the lower limit wavelength (λ_l) (*solid line*). Grey stripes indicate the range of $\mu_{\text{opt}}(z_0)$ values obtained for the four test objects in numerical simulations; simple means and weighted averages of these values are marked by open circles and black squares, respectively. Two formerly used analytical estimates are plotted for comparison (*dash-dot and short-dash lines*).

6.2 HgCdTe detectors

We present similar analysis to the above for two HgCdTe detectors, also commonly used for PPTR temperature profiling. First HgCdTe detector has peak sensitivity at λ_p = 10 µm, the upper spectral limit (λ_h) is fixed at the cut-off wavelength of the detector, λ_c = 12 µm, while the lower limit is varied between 3.0 µm and λ_p.

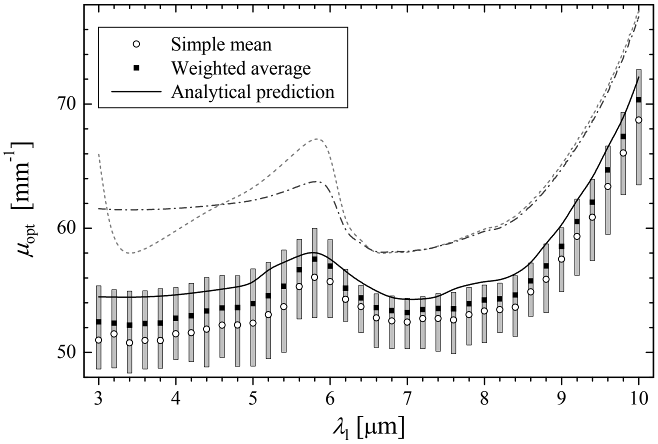

Figure 6.7: Analytically assessed μ_{opt} (Eq. 6.2) as a function of λ_l (*solid line*) for the HgCdTe detector with peak sensitivity at 10 µm. Grey stripes indicate the range of $\mu_{\text{opt}}(z_0)$ values obtained for the four test objects in numerical simulations; simple means and weighted averages of these values are marked by open circles and black squares, respectively. Two formerly used analytical estimates are plotted for comparison (*dash-dot and short-dash lines; see text for details*).

Figure 6.7 presents the analytically assessed optimal absorption coefficient value, μ_{opt} (Eq. 6.3), as a function of the lower limit wavelength, λ_l (solid line). For all included spectral bands, the analytical estimate falls within (or just marginally deviates from) the range of values $\mu_{\text{opt}}(z_0)$ obtained for the four test objects in numerical simulations (grey vertical stripes). For the maximal spectral band (λ_l = 3.0 µm), the mismatch between μ_{opt} (Eq. 6.3) and simple mean of the latter (open circles) is 3.5 mm^{-1}. If the weighted average is taken as the target value (black squares), the mismatch is only 2.0 mm^{-1} (3.8%). Clearly, our analytical estimate μ_{opt} (Eq. 6.3) provides a much better fit to the numerical data than the earlier used $\tilde{\mu}_{\mathrm{eff}}$ (Eq. 6.4) or convolution of $\mu(\lambda)$ with $R(\lambda)$ (dash-dot and short-dash lines, respectively) for all 36 spectral bands included in this part of the study.

For the HgCdTe detector with peak sensitivity at $\lambda_p = 12$ µm, our analytical estimate μ_{opt} (Eq. 6.3) (Fig. 6.8, solid line) falls within the range of numerically determined values $\mu_{\mathrm{opt}}(z_0)$ (grey stripes) for each of the included spectral bands. The match is particularly good if the weighted average of the four $\mu_{\mathrm{opt}}(z_0)$ is considered at each λ_l (black squares). In contrast, the earlier used analytical estimates $\tilde{\mu}_{\mathrm{eff}}$ (Eq. 6.4) and weighted average of $\mu(\lambda)$ with weight $R(\lambda)$ (dash-dot and short-dash lines, respectively) deviate significantly from the numerical results even for moderately wide detection bands (e.g., $\lambda_l = 10$ µm). With further decrease of λ_l, the mismatch between $\tilde{\mu}_{\mathrm{eff}}$ (Eq. 6.4) (dash-dot line) and simple mean of the numerical $\mu_{\mathrm{opt}}(z_0)$ (open circles) stays large and amounts to 25 mm^{-1} (or 43% of the target value) at $\lambda_l = 3.0$ µm.

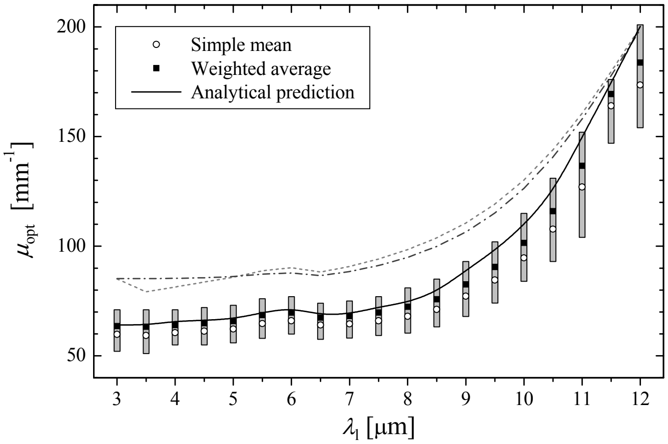

Figure 6.8: Same as Fig. 9.7, but for HgCdTe detector with peak sensitivity at $\lambda_p = 12$ µm.

6.3 Discussion

Figure 6.2 illustrates how a ~10% deviation from the optimal value μ_{eff} deteriorates the reconstructed temperature profile (top, bottom). In soft biological tissue, such as human skin with $\mu(\lambda)$ in mid-IR varying by two orders of magnitude (Fig. 6.1), determining the optimal value μ_{eff} to such a narrow margin is certainly a nontrivial task. In a separate numerical study,[47] white noise in the simulated signal (SNR = 300) suspended the high dependence of relative image error (δ) on μ_{eff} only within a very narrow interval around μ_{opt}. At deviations larger than 2–3% of the optimum value, the influence on δ was clearly present, rather than buried in the effect of noise, as is believed quite often.

Being aware of the spectral variation $\mu(\lambda)$ in their gel samples, Prahl *et al*[53,9] estimated the effective value μ_{eff} by averaging $\mu(\lambda)$ of water over the 8–12 µm detection band, using spectral sensitivity $R(\lambda)$ of the HgCdTe detector as a weight. The closest match to such experimental conditions is found in Fig. 6.8 (short dash line, $\lambda_l = 8.0$ µm), which suggests that their estimate of μ_{eff} may have been too high. Of course, this comparison does not provide any indication of the possible implications of such deviation for their results. In fact, at such high values of μ_{eff} we would expect only a minimal effect on profiling, likely limited to the most superficial 10 µm of the sample. On the other hand, Fig. 6.6 leaves no doubt that applying the same approach to the commonly used InSb detector with $\lambda_l = 3.0$ µm would be disastrous.

Milner *et al*[6,7] applied a more elaborate expression $\tilde{\mu}_{\mathrm{eff}}$ (Eq. 6.4) to HgCdTe detector used at 7–11 µm, and 10–14 µm, respectively. As indicated by Figs. 6.7 and 6.8 (dash-dot line), the improvement over the previous approach is only marginal. This can be attributed to the weak spectral variation of $B_\lambda'(T_b)$ in this part of the spectrum (Fig. 6.1b). On the other hand, a dramatic improvement is obtained for InSb detector at 3–5 µm (see Fig. 6.6, dash-dot vs. short-dash line) where $B_\lambda'(T_b)$ exhibits a large spectral variation. Nevertheless, the remaining discrepancy between $\tilde{\mu}_{\mathrm{eff}}$ (Fig. 6.6, dash-dot line) and numerically determined $\mu_{\mathrm{opt}}(z_0)$ at $\lambda_l = 3.0$ µm (grey stripe) suggests that the value used for temperature profiling in human skin by Milner *et al*[6] may have been overestimated. The possible effect of such a discrepancy can be guessed from Fig. 6.2 and extrapolation of data in Fig. 6.3(a) - while keeping in mind the possible differences between the model functions $\mu(\lambda)$ and $R(\lambda)$ in the two studies.

The values μ_{opt} (Eq. 6.3) obtained with our novel analytical approach in general provide a much better fit to the numerical results than the previously used estimates (Figs. 6.6–6.8; solid, short-dash, and dash-dot lines, respectively). (The results converge towards the right end of Figs. 6.6 and 6.8). Moreover, μ_{opt} (Eq. 6.3) fall within the range of values $\mu_{\mathrm{opt}}(z_0)$ obtained in the numerical simulations (grey stripes) for most of the 68 detector/spectral band combinations tested in this study. The same is rarely the case for either earlier approach.

Spectral variation of $\mu(\lambda)$ in water is most pronounced in the lower part of detection band for all three detectors in this study (Fig. 6.1). Narrowing of the acquisition band with a cut-on filter significantly improves the validity of quasi-monochromatic approximation (Eq. 2.9). This is evidenced by the decrease of relative image error (δ) for all test objects (Figs. 6.3b, 6.4b). The four optimal values $\mu_{\mathrm{opt}}(z_0)$ lie closer together (Figs. 6.3b, 6.4a), which should further improve the accuracy of depth profiling when absorbers are distributed at varying (or multiple) subsurface depths.

On the other hand, narrower spectral bands will in general result in smaller PPTR signal amplitude and thus decrease SNR. The optimal detection band for given experimental conditions (i.e., $\mu(\lambda)$, $R(\lambda)$) can thus be determined only by consideration of the related experimental noise. Such analysis is presented in Chapters 9 and 10.

Finally, broad-band IR detection is commonly employed also in other PTR techniques, such as measurements of thermal diffusivity, depth profiling of sample thermal conductivity, or non-destructive evaluation using measurements in frequency domain. To our knowledge, most of these techniques also assume an effective absorption coefficient value μ_{eff} in the involved signal analysis. Selection of μ_{eff} and its influence on the results deserve some thought when these techniques are applied to biological tissues or other materials with significant variation of $\mu(\lambda)$ in the detection band. Because rather general relations describing formation of the radiometric signal were involved in our determination of μ_{opt} (Eq. 6.3), the same or slightly adapted approach might provide viable values might be applicable also to some PTR techniques beyond PPTR temperature profiling.

6.4 Conclusions

The presented approach enables analytical determination of viable effective IR absorption coefficients to be used in reconstruction of temperature profiles from PPTR signals at any combination of sample spectral properties, radiation detector, and acquisition spectral band. This is particularly important in samples with large spectral variation $\mu(\lambda)$ in mid-IR, such as most biological tissues, where previously used analytical estimates are not sufficiently accurate.

Chapter 7

Sampling rate

Signal sampling rate is one of the experimental parameters involved in PPTR temperature profiling. Reported PPTR studies in biological tissues[6,7,18,19,49] utilized a wide range of sampling rates ($f = 125$–$1700\ \mathrm{s}^{-1}$), but the reasons for selecting the actual sampling rates were not discussed. Basic relation, which illustrates how the axial resolution Δz depends on sampling time Δt, is the well known expression for the heat diffusion length $\Delta z = \sqrt{4D\,\Delta t}$. Evidently, the axial resolution increases with sampling frequency. However, this relation does not include the effects of μ, h and noise.

In this chapter we study the effect of sampling rate on the accuracy of reconstructed PPTR temperature profiles. We simulate PPTR signals with different sampling rates for different temperature profiles, and then reconstruct initial temperature profiles.

7.1 Methods

We consider a temperature profile resulting from radiative absorption in a layer of width w located at depth z_1

$$\Delta T_0(z) = \begin{cases} \Delta T_0 \exp(-k\left[z - z_1\right]), & z_1 \le z \le z_1 + w \\ 0, & \text{otherwise} \end{cases} \tag{7.1}$$

The corresponding theoretical PPTR signal is determined analytically by substitution of (7.1) into (2.7) and completing of the z integral[6]

$$\begin{aligned} S_0(t) = \frac{\Delta T_0\, \mathrm{e}^{k z_1}}{2} \Bigg(& e^{-kz - z^2/4Dt} \left\{ \frac{\mu\, \mathrm{erfcx}(u_+)}{\mu - \mathrm{k}} - \frac{\mu\, \mathrm{erfcx}(u_-)}{\mu + \mathrm{k}} \right. \\ & \left.\left. + \frac{2\mu h}{h-k}\left[\frac{\mathrm{erfcx}(u_1)}{h-k} - \frac{\mathrm{erfcx}(u_+)}{\mu - k}\right] + \frac{2\mu k(\mu + h)\,\mathrm{erfcx}(u_2)}{(\mu+k)(\mu-k)(hk)} \right\} \right)_{z_1}^{z_1+w} \end{aligned} \tag{7.2}$$

where k represents light absorption coefficient and $u_2 = k\sqrt{Dt} + z/\sqrt{4Dt}$. This temperature profile is convenient for our simulation, because exact PPTR signal values $S_0(t_i)$ can be calculated by simple evaluation of (7.2) at time t_i.

We select the parameter values $\Delta T_0 = 30$ K and $w = 50$ µm, and we vary z_1 from 50 µm to 500 µm and sampling rate f from $100\ \mathrm{s}^{-1}$ to $10{,}000\ \mathrm{s}^{-1}$. The total acquisition time is 1.0 s for all simulated signals. The thermal parameters are $D = 0.143\ \mathrm{mm}^2/\mathrm{s}$ and $h = 0.02\ \mathrm{mm}^{-1}$, while the effective absorption coefficient is $\mu = 27\ \mathrm{mm}^{-1}$, which corresponds to the entire spectral band of the InSb detector and agar substrate (chapter 8).

Theoretical signals $\boldsymbol{S}_0$ calculated for temperature profiles with $z_0 = 50$, 100, 200 and 400 µm are augmented with 10 different realizations of realistic noise. The noise is characterized by $f_\mathrm{c} = 15$ Hz, $\alpha = 1.3$ and $NE\Delta T = 6.7$ mK determined at $f = 10{,}000\ \mathrm{s}^{-1}$ (section 3.5). Based on (3.3) and (3.4), noise amplitudes for smaller sampling rates are scaled as

$$NE\Delta T(f) = 6.7\,\text{mK}\sqrt{\frac{f}{10{,}000\,s^{-1}}} \tag{7.3}$$

Initial temperature profiles $\boldsymbol{T}$ are reconstructed from simulated PPTR signals using the monochromatic kernel $\boldsymbol{K}$ (2.9) with the above parameters. Reconstruction results consist of 200 temperature values over a depth range of 1.0 mm (Δz = 5 μm). A maximum of 5000 iterations of the projected υ-method are allowed per signal.

7.2 Results

7.2.1 Noiseless signals

Figure 7.1 presents temperature profiles reconstructed from noiseless PPTR signals $\boldsymbol{S}_0$ at sampling rate 100 (*left*), 1000 (*center*) and 10,000 s^{-1} (*right*). Each reconstruction result is obtained after 5000 iterations of the reconstruction algorithm.

Clearly, increasing the sampling rate improves quality of reconstruction results. All temperature profiles reconstructed from PPTR signals with f = 100 s^{-1} are markedly broader and attenuated as compared to temperature profiles reconstructed from PPTR signals with f = 1000 s^{-1} and f = 10,000 s^{-1}. The quality of reconstruction results additionally improves, when f is increased from 1000 to 10,000 s^{-1}. Thus, temperature profile located at z_1 = 50 μm roughly resembles sharp edges of the actual object (*gray line*).

All tested sampling rates f = 100–10,000 s^{-1} yield equivalent peak temperature depths Z, except for test object located at z_1 = 50 μm. For this object, in images corresponding to f = 5000 and 10,000 s^{-1} we observe some features of the lower edge of test object.

Figure 7.2 presents the determined relative image error δ (Eq. 4.10) and width W as a function of z_1. For all test objects, the relative image error δ decreases as sampling frequency increases (Fig. 7.2a). However, the increase is more notable for f = 100–1000 s^{-1} than for f larger than 1000 s^{-1}. Optimal δ are obtained for f = 10,000 s^{-1}. Similar trend is observed for width W (Fig. 7.2b).

The above results agree well with the dependence of Δz on f following from the heat diffusion length equation. But, the simulation involving noiseless signals do not correspond to real PPTR temperature profiling. Therefore we must include realistic noise in simulated PPTR signals to estimate, how the accuracy of reconstructed temperature profiles depends on f for real PPTR temperature profiling.

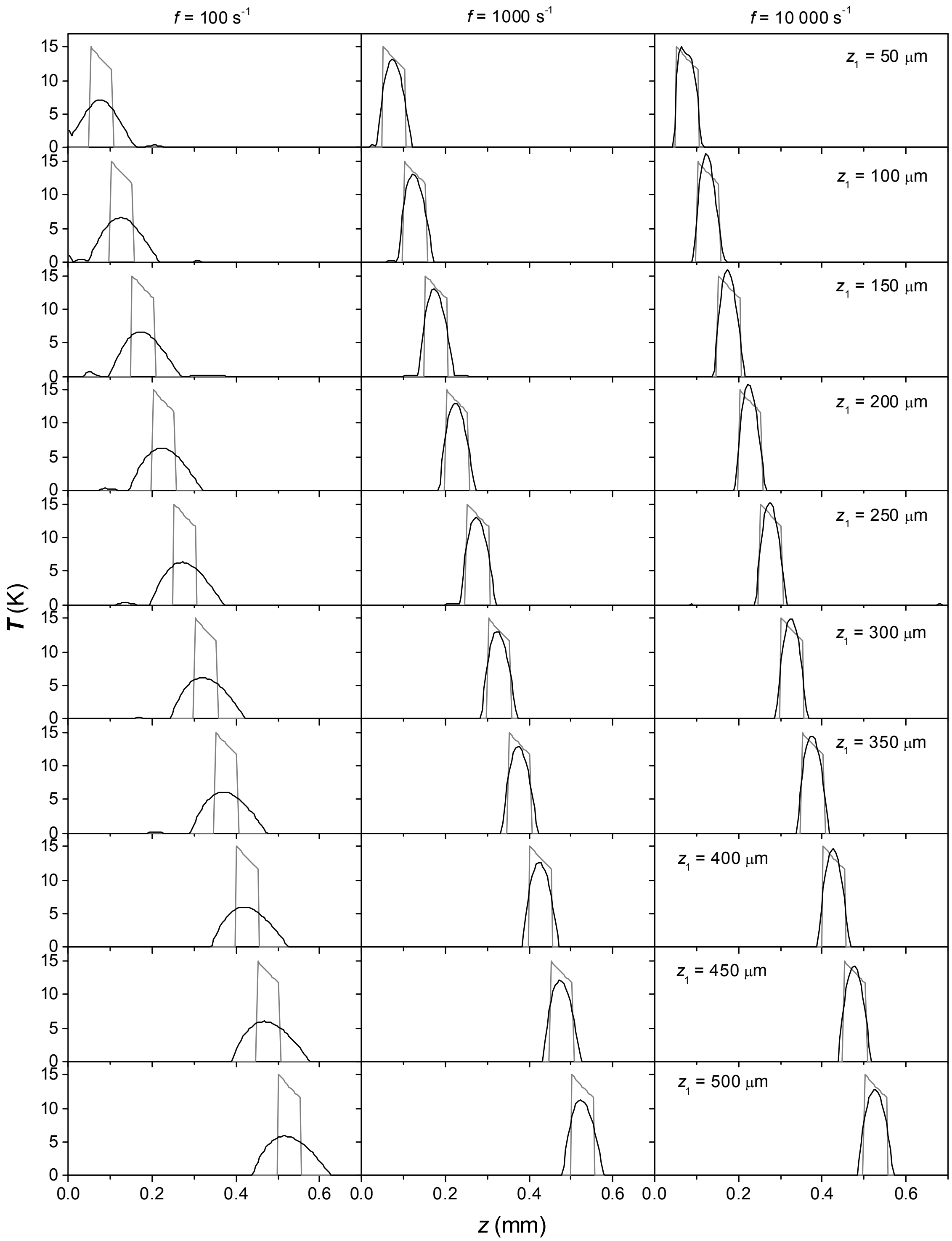

Figure 7.1: Temperature profiles reconstructed from theoretical signals for test objects located at different depths z_1 (*see labels*). Results for sampling rates 100 (*left*), 1000 (*center*) and 10,000 s^{-1} (*right*) are presented. The actual test objects are plotted for comparison (*gray line*).

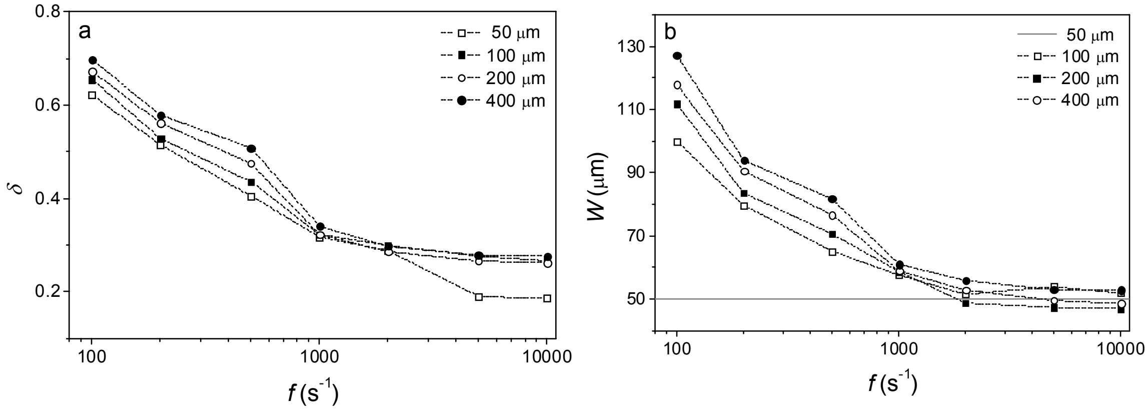

Figure 7.2: (a) Relative image error δ (Eq. 4.12) and (b) full-width at half-maximum of the temperature profiles *W*. Results for samplig rates f = 100–10 000 s^{-1} are presented (*see legend*). Gray line in (b) indicates the actual width (50 μm).

7.2.2 Signals with noise

Figure 7.3 presents simulated PPTR signals with realistic noise for f = 100 (*left*), 1000 (*center*) and 10,000 s^{-1} (*right*). Four test objects located at z_1 = 50–400 μm (*see labels*) are considered. Evidently, PPTR signals become more noisy as f increases (Fig. 7.4).

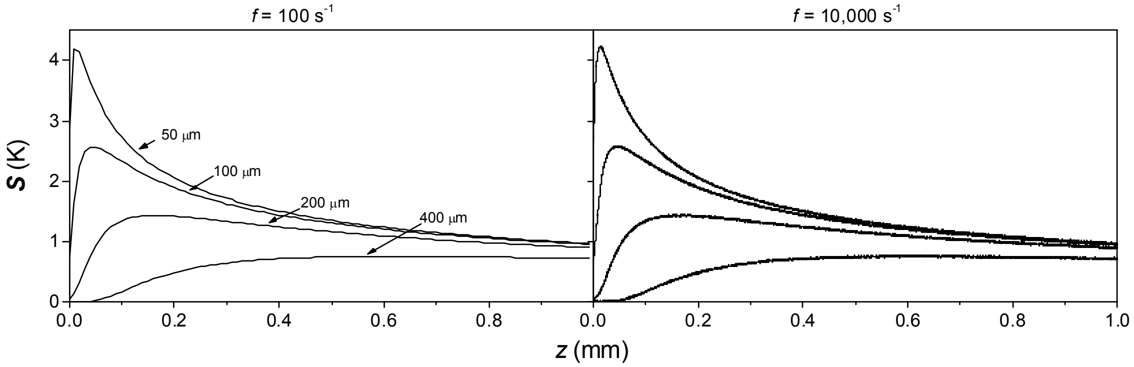

Figure 7.3: Simulated PPTR signals for test objects with z_1 = 50, 100, 200 and 400 μm (*see labels*) and sampling rates of 100 (*left*), 1000 (*center*) and 10,000 s^{-1} (*right*) augmented by realistic noise.

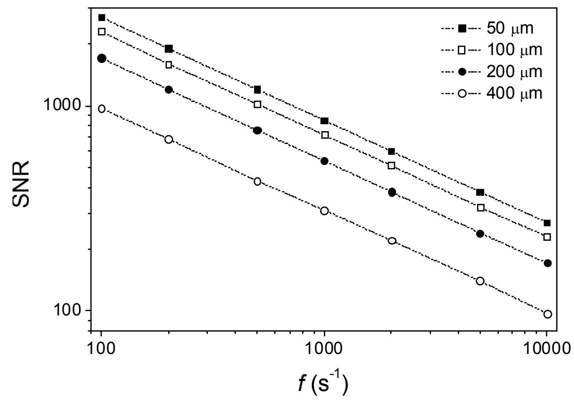

Figure 7.4: SNR of the simulated PPTR signals as a function of sampling frequency f for test objects with z_1 = 50 (*solid squares*), 100 (*open squares*), 200 (*solid circles*) and 400 μm (*open circles*).

Figure 7.5 presents statistical analysis of the reconstruction results for three sampling rates. While images for $f = 100\ \mathrm{s}^{-1}$ (*left column*) are similar to images reconstructed from noiseless signals with $f = 100\ \mathrm{s}^{-1}$ (Fig. 7.1, *left column*) for all depths, the images of objects located at $z = 200$ and 400 μm for $f = 1000$ and $10{,}000\ \mathrm{s}^{-1}$ are evidently broadened and attenuated as compared to corresponding images reconstructed from noiseless signals (Fig. 7.1, *center* and *right*). Both effects are more expressed for $f = 10{,}000\ \mathrm{s}^{-1}$ due to smaller SNR.

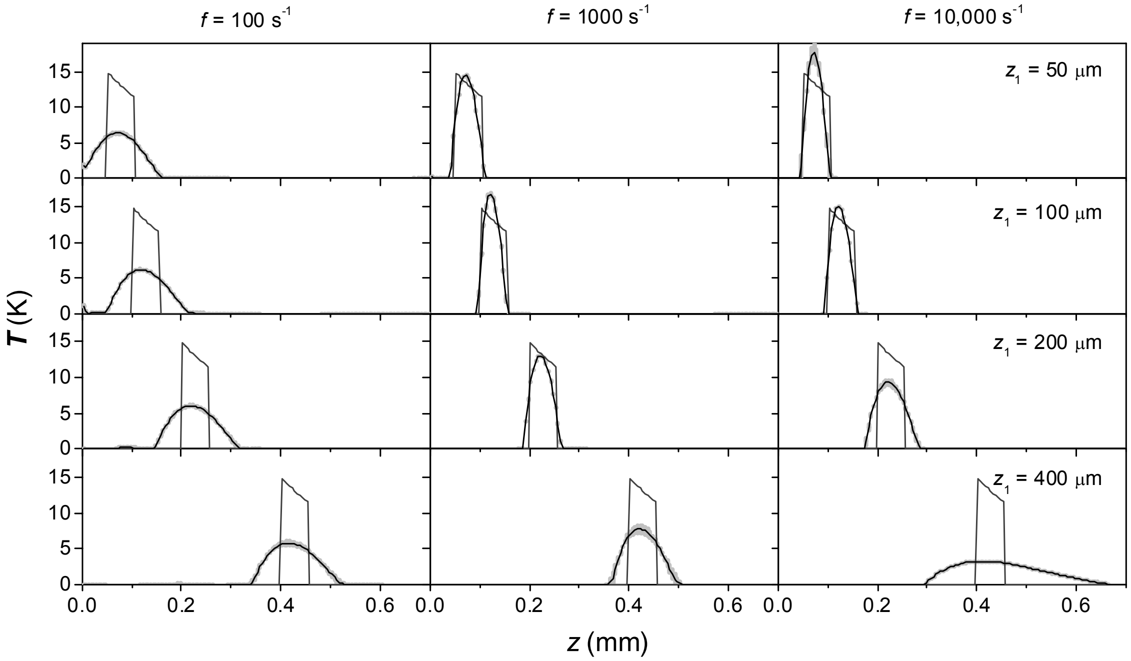

Figure 7.5: Average temperature profiles (*black lines*) and standard deviations (*light-gray spots*) reconstructed from 10 simulated PPTR signals with different noise realizations. Images of test objects with z_1 = 50–400 μm (*see labels*) are reconstructed from PPTR signals with $f = 100$ (*left*), $1000\ \mathrm{s}^{-1}$ (*center*) and $10{,}000\ \mathrm{s}^{-1}$ (*right*). The actual test objects (*dark-gray line*) are plotted for comparison.

In general, the accuracy of determined peak temperature depths Z is similar for $f = 1000$ and $10{,}000\ \mathrm{s}^{-1}$. However, for the deepest test object ($z_1 = 400$ μm) Z obtained for $f = 10{,}000\ \mathrm{s}^{-1}$ is markedly less accurate than for $f = 1000\ \mathrm{s}^{-1}$.

Relative image error δ and temperature peak width W as function of sampling rate for PPTR signals with noise are presented in Fig. 7.6. For test objects with $z_1 = 50$ and 200 μm, we obtain the smallest image errors ($\delta = 0.29$ and 0.31 for $z_1 = 50$ and 200 μm, respectively) at $f = 1000\ \mathrm{s}^{-1}$ (Fig. 7.6a), while the largest sampling rate $f = 10{,}000\ \mathrm{s}^{-1}$ is optimal for object with $z_1 = 100$ μm ($\delta = 0.28$). On average, with f increased above the optimal f image error δ increases due to decreased SNR, and with f decreased below the optimal f image error δ decreases due to insufficient information in PPTR signal. Similar trends are observed for width W (Fig. 7.6b).

In contrast to results obtained from noiseless signals, low SNR significantly deteriorates images reconstructed from PPTR signals with large sampling rates. While shallow test objects ($z_1 = 100$ μm) benefit from large f, deeper test objects ($z_1 = 200$ μm) are reconstructed more accurately at moderate sampling rates ($f = 1000$–$2000\ \mathrm{s}^{-1}$). Low sampling rates ($f = 100$–$200\ \mathrm{s}^{-1}$) yield robust and comparable reconstruction results for all depths z_1, but markedly less accurate as compared to these obtained at moderate sampling rates.

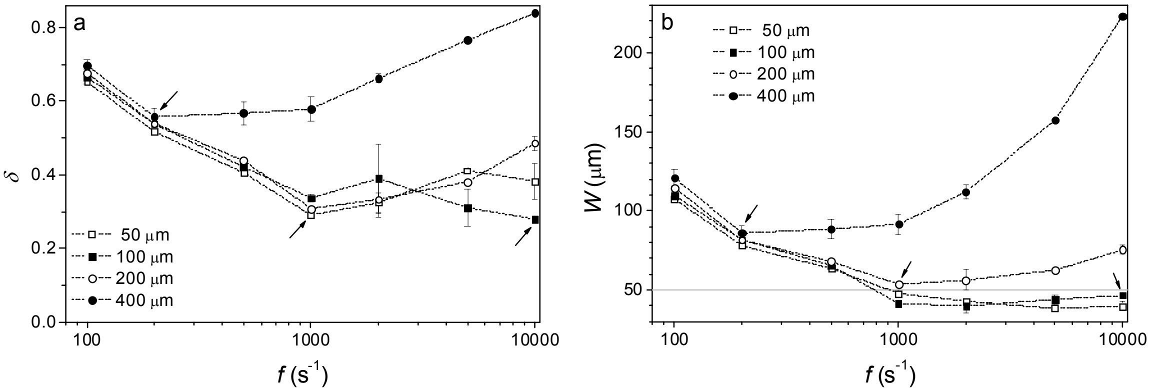

Figure 7.6: (a) Relative image error δ, (b) full-width at half-maximum W, and (c) peak temperature T_p as a function of sampling rate f for test objects located at z_l = 50–400 µm (*see legend*) and PPTR signals with noise. Gray line indicates (b) the actual width (50 µm) and (c) the actual peak temperature. Arrows point to optimal values.

7.3 Discussion

Temperature profiles reconstructed from PPTR signals augmented with noise are markedly less accurate when large f is used. The results in Fig. 6.5 indicate that high sampling rate (f = 10,000 s^{-1}) is preferred only for shallow object (z_l = 100 µm), while deeper temperature profiles are reconstructed more accurately with moderate sampling rates (f = 1000–2000 s^{-1}). Equal trends are observed also for parameters of temperature profiles (Fig. 6.6). The image error δ as well the excessive width W are more prominent at high sampling rates (f = 5000 and 10,000 s^{-1}) as compared to moderate sampling rates (f = 1000 and 2000 s^{-1}). Both, δ and W, increase with increasing depth Z for these sampling rates, while they are almost independent of Z for small sampling rates (f = 100 and 200 s^{-1}). Thus, low sampling rates can be used to reconstruct deep objects (z_l > 500 µm), where signals with larger f are significantly deteriorated by noise. In general, the optimal sampling frequency depends also on noise amplitude and depth discretization.

Considering the results of this study, a good alternative to fixed sampling rate used in PPTR temperature profiling would be a non-uniform spacing in time (i.e., binning) as suggested by Sathyam and Prahl[9]. This would also reduce the signal vector lengths and kernel matrix size, thus reducing computational costs.

7.4 Conclusions

When temperature profiles are reconstructed from PPTR signals with large SNR, higher sampling rates always yield better reconstruction results. But in presence of realistic noise, high sampling rates ($f \approx$ 10,000 s^{-1}) are optimal for shallowest temperature profiles ($z \leq$ 100 µm) only, while moderate sampling rates ($f \approx$ 1000 s^{-1}) are optimal for other temperature profiles. However, for our PPTR system f = 1000 s^{-1} offers acceptable reconstruction results for all depths. In general, optimal sampling rate depends on specifics of experimental system and properties of the studied samples.

Chapter 8

Tissue phantoms

It is important for evaluation of PPTR temperature profilometry of human skin to develop reliable phantoms with well defined geometry that suitably mimic optical and thermal properties as well infrared absorption of human skin. The development of tissue phantom for PPTR involves the choice of matrix composition and absorber. In addition, one may also add scattering particles. An excellent review of tissue phantoms for medical optics is provided by Pouge and Patterson[54], while Pifferi *et al*[55] suggested directions for designing and characterization of tissue phantoms for biomedical optics.

Here we show preparation of agar and collagen tissue phantoms, including gel layer and absorption layer preparation. In addition, we present measured IR spectrum of both types of gel and write corresponding heat diffusion constants.

8.1 Hydrogel layer

Since the main component of human skin and both gels is water, matrix composition of tissue phantoms used for PPTR temperature profiling should have similar thermal and IR absorption properties as human skin. Tissue phantoms composed of thin collagen films are a perfect match for real skin.[7] Due to good optical and thermal properties collagen and polcrylamide gels were also used for a PPTR temperature profiling.[9] In our studies we use agar and collagen gels.

8.1.1 Agar gel

Agar gel was prepared by dissolving 0.15 mg of agar powder in 6 ml of distilled water, thus obtaining the agar solution with weight percent of agar 2.5 wt.%. When the agar powder was completely dissolved, the polymerization was initiated by heating the mixture to the boiling point in a microwave oven.

Individual gel layers were produced by injecting the agar solution onto a wetted microscope slide with two identical spacers positioned near the ends of the slide (Fig. 8.1). To prevent the entrance of air bubbles, which were present mostly on the surface of the agar mixture, into the agar layer and to precisely control the quantity of the agar solution, a syringe was used. A second slide was placed on top of the agar mixture and gently pressed against the spacers. When polymerization was complete, the top slide was carefully removed, exposing the gel layer of uniform thickness (Fig. 8.2).

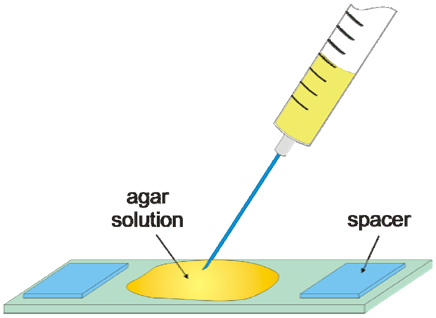

Figure 8.1: Schematic of agar layer preparation.

Figure 8.2: Prepared agar layer with scatterers (TiO_2) on a microscope glass slide.

Agar layers without scatterrer are transparent to visible light, because they are mostly composed of water. In contrast, agar gel is not transparent to infrared radiation. The sample infrared spectrum is required for PPTR temperature profiling, therefore we measured the IR spectrum of the prepared agar gel using an IR spectroscope. The measured agar gel absorption coefficient μ as a function of wavelength λ is presented in Figure 8.3. The agar spectrum (*black line*) agrees well with the spectrum of water (*gray line*) for λ = 3–6 µm, while at larger wavelengths protein peaks are present.

Another important quantity is the thermal diffusivity constant D of agar gel. Reported values of diffusivities are D = 0.140 ± 0.007,[56] 0.1427,[57] and 0.138 mm^2/s [58] for 2.5% agar gel. All reported values are a little smaller when compared to the thermal diffusivity constant of water (D = 0.145 mm^2/s at T = 25° C) [59]. In our studies, we have found that D = 0.143 mm^2/s for agar gel yields optimal reconstruction results.

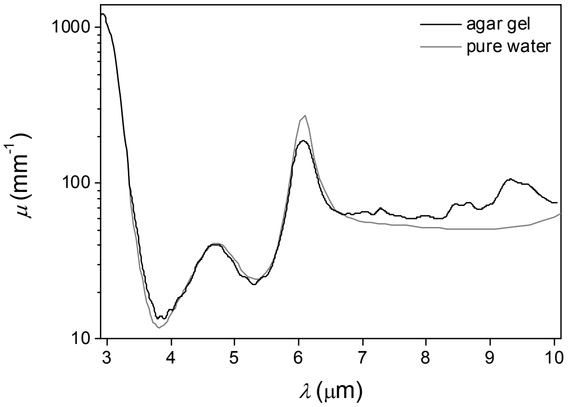

Figure 8.3: Measured IR absorption coefficient μ of the agar gel *(black line*). Absorption spectrum of water (*gray line*)[48] is plotted for comparison.

7.1.2 Collagen gel

To obtain the gelatin solution with 25 weight percent of gelatin, we dissolved 1.25 g of gelatin powder (bovine skin, Sigma-Aldrich) in 3.75 ml of water with 0.2% of formaldehyde. Inclusion of formaldehyde increases the melting temperature of the gelatin matrix by increasing the crosslinking of the fibers while preserving the thermal and spectral properties.[54] This allows the collagen phantoms to be used at room temperature.

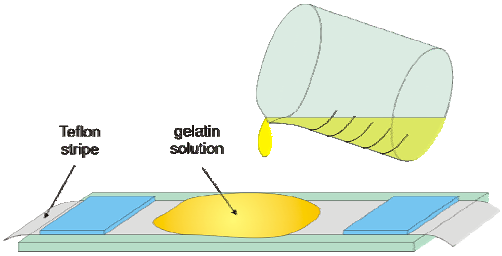

Figure 8.4: Schematic of gelatin layer preparation.

We prepared the collagen layer by dissolving the gelatin powder in water at 70° C in water bath.[60] When the gelatin powder was completely dissolved under vigorous stirring for 2 min, the homogenous viscous solution was carefully poured onto a microscope slide with two identical spacers positioned near the ends of the slide (Fig. 8.4). The slide was covered by a thin Teflon stripe, since collagen gel sticks on glass substrate very strongly. A second microscope slide covered by a Teflon stripe was placed on top of the gelatin solution and gently pressed against the spacers. When the gelatin was cooled down to room temperature, we first carefully removed the top slide and then the top Teflon stripe to expose the gel layer. Because of the large viscosity of gelatin, we could not use a syringe.

Figure 8.5 presents the measured IR spectrum of the gelatin gel. The gelatin spectrum (*black line*) is about 75% of water spectrum (*gray line*) at λ = 3–6 μm, while at larger wavelengths protein absorption peaks dominate.

The thermal diffusivity D of the gelatin gel is assumed to be that of human skin (D = 0.11 mm^2/s), based on similar water content to that in human skin.

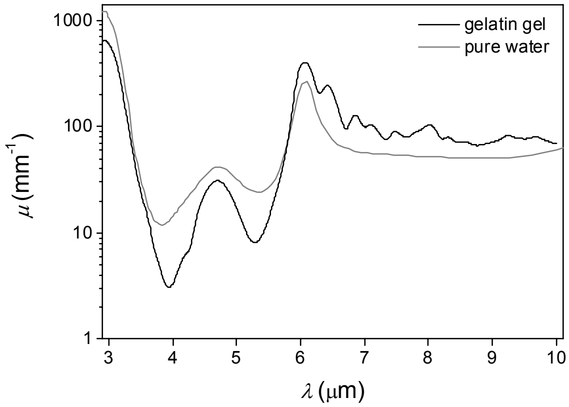

Figure 8.5: Measured IR absorption coefficient μ of the gelatin gel *(black line*). Absorption spectrum of water (*gray line*)[48] is plotted for comparison.

8.1.3 Scatterer

Human skin is a highly turbid medium with the reduced scattering coefficient of dermis[61] μ_s' = 4 mm^{-1} and of epidermis μ_s' = 12 mm^{-1}. To better mimic skin properties, scattering particles were added to our tissue phantoms. Since gelatin and agar phantoms were used for a short period only and then discarded, we used inexpensive titanium dioxide (TiO_2) scattering particles. To obtain the above scattering coefficient we mixed 4 mg and 12 mg of TiO_2 (Sigma-Aldrich) into 1 ml of gel solution. These concentrations of TiO_2 were found experimentally by measuring spectrum of visible light transmitted through thin gel layers with different concentrations of scatterers. Figs. 8.2, 8.7 and 8.9 presents agar layers with TiO_2 particles.

8.2 Absorbing layer

When we first started preparing tissue phantoms, we prepared the absorbing layers by powdering the surface of the gel layer with small amounts of fine carbon black powder, which was then cowered by another gel layer (Fig. 8.6). Carbon black powder was selected because it is hydrophobic and, therefore, does not diffuse into the gel, enabling preparation of stable thin absorbing layers.[49]

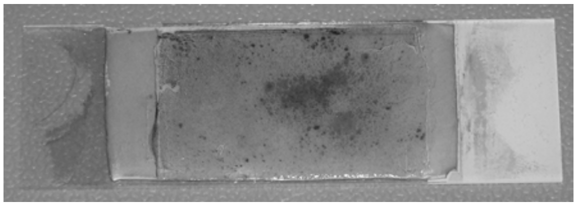

Figure 8.6: Fine carbon black powder absorbing layer on a agar substrate covered by a thin (~100 μm) agar gel layer with scatterers.

Very thin absorbing layers can be prepared by placing a thin absorbing foil over the hydrogel layer. We used polyethylene foil of thickness ~10 μm. Since foil is crushed during preparation of tissue phantom (see Fig. 8.7), the effective thickness ((~20 μm) is larger than the actual thickness.

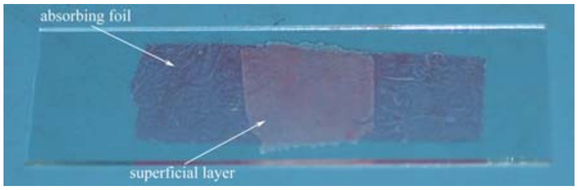

Figure 8.7: Absorbing foil covered by a thin (~100 µm) agar gel layer with scatterers.

Thicker absorbing layers (*d* > 30 µm) were prepared as a hydrogel layer with addition of black India ink as the absorber. Both techniques of absorbing layer preparation resulted in absorbing layers of well defined geometry and of homogenous absorber distribution.

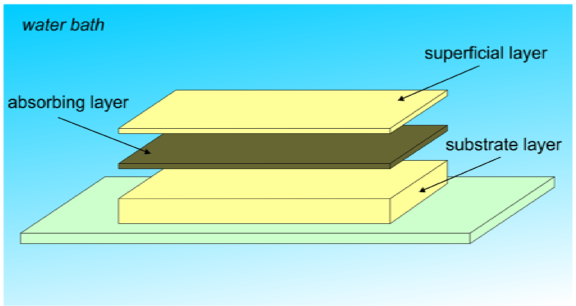

Figure 8.8: Schematic of a tissue phantom with a single absorbing layer. Water bath prevents the formation of air bubbles between adjacent layers.

We put the prepared absorbing and hydrogel layers in water bath, where we constructed the tissue phantom (Fig. 8.8). Water bath effectively prevents formation of air bubbles between the adjacent layers. Finally, the composed tissue phantom was carefully removed from the water bath. Figure 8.9 presents a finished tissue phantom with a single absorbing foil as the absorbing layer.

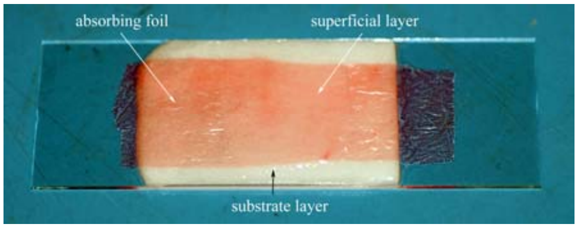

Figure 8.9: Finished tissue phantom with a single absorbing foil as the absorbing layer.

If tissue phantoms are not immediately used in an experiment, they must be kept sealed in airtight enclosures such as plastic bags or containers to prevent drying. Keeping the phantoms in vegetable oil has also been reported as an excellent way to preserve the water content.[62]

Chapter 9

Spectral filtering

Numerical simulations in Chapter 6 show how narrowing of the acquisition band improves the validity of quasi-monochromatic approximation (Eq. 2.9) and therefore improves the reconstruction results. However, this causes a reduction in signal, therefore lower SNR, which adversly affects the reconstruction results. Hence, the optimal detection band for given experimental conditions can be determined only by considering the related experimental noise.

9.1 Experiments in agar tissue phantoms

9.1.1 Materials and methods

Agar gel tissue phantoms

Three tissue phantoms evaluated in this study (samples A, B, and C) consisted of a 1–2 mm thick gel substrate, thin absorbing layer, and one superficial gel layer of varying thickness. Absorbing layers were prepared by powdering the agar gel layer surface with fine carbon black powder. Details of the agar layer preparation were presented in Chapter 8. The subsurface depths of the absorbing layers were approximately 130, 280, and 450 μm, respectively, which corresponded to the location of a vascular network in shallow, medium, and deep port-wine stain birthmarks, respectively. One tissue phantom (sample D) included two absorbing layers at approximate depths of 240 and 440 μm. In this sample, TiO_2 powder was homogeneously dispersed in the substrate to enhance optical scattering. The increased light fluence in the deeper absorbing layer resulted in two temperature peaks with comparable amplitudes, despite strong attenuation of the incident laser pulse by the upper absorbing layer.[63]

Pulsed photothermal profiling

For each PPTR measurement, the sample was irradiated with a single 1.5 ms long 585 nm pulse from a pulsed dye laser. Radiant exposure near the center of a 10 mm diameter laser spot was ~3 J/cm^2. Radiation emitted from the center of the irradiated area was collected on the focal-plane array of a fast IR camera (Phoenix, Indigo, Santa Barbara, CA, USA) using a macro IR objective with magnification $M = 1$. By limiting the data read-out to a 128 × 64 pixel sub-window and setting the integration time to $t_{\mathrm{int}} = 0.5$ ms, the acquisition rate was 1083 frames per second. The acquisition time was set to 1 s after the laser pulse.

Radiometric signals were obtained from 3 different sites on each sample, separated by a few millimeters to prevent thermal interference between successive measurements. On each test site, up to three radiometric signals were acquired using the entire spectral band of the IR camera ($\lambda = 3.0$–5.6 μm) and also with a custom long-pass IR filter (cut-on at 4.5 μm, Barr Associates, Westford, MA) fitted to the collection optics.[18] The response of each array element was calibrated using a computer-controlled black body (BB701, Omega Engineering, Stamford, CT, USA). Finally, the PPTR signals $\boldsymbol{S}$ (in absolute radiometric temperature units) were obtained by averaging data from 40 × 40 detector elements (active area $A = 1.2 \times 1.2$ mm^2) and subtracting the baseline value.

Initial temperature profiles $\boldsymbol{T}$ (images) were reconstructed using the monochromatic approximation (Eq. 2.9) and the PR-CG reconstruction algorithm (chapter 4). Elements of the monochromatic kernel matrix $\boldsymbol{K}$ were calculated using the thermal parameter values $D = 0.134$ mm^2/s and $h = 0.02$ mm^{-1}. The effective absorption coefficient was determined as $\mu_{\text{eff}} = 28.0\ \text{mm}^{-1}$ for broad-band signal acquisition ($\lambda = 3.0$–$5.6\ \mu$m) and $\mu_{\text{eff}} = 30.2\ \text{mm}^{-1}$ for the narrowed spectral band (4.5–5.6 μm). These values were determined from IR spectral properties of the sample (Fig. 8.3) and radiation detector (Fig. 9.1) following the approach presented in Chapter 6. Each reconstruction result consisted of 140 temperature values over a depth range of 0.7 mm (discretization step $\Delta z = 5\ \mu$m).

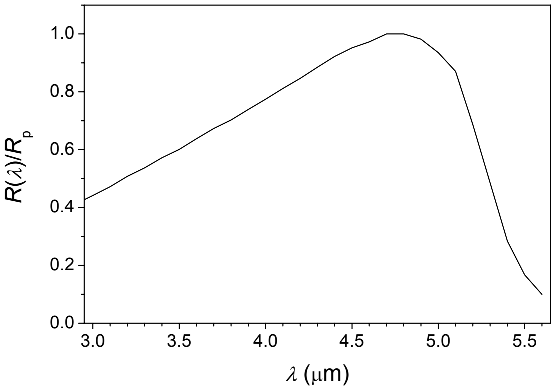

Figure 9.1: Relative responsivity of an InSb detector (J10, Judson Technologies, Montgomeryville, PA) in mid-IR spectral region.

Optical coherence tomography and histology

Several cross-sectional images per sample were acquired using an OCT system[64] with a central source wavelength of 1.3 μm. The axial and lateral scanning lengths were set to 800 μm and 2 mm, respectively. The images were saved in JPEG format (400×634 pixels) for further analysis. For purposes of presentation and analysis, the axial dimensions within the sample were corrected using an estimated index of refraction (1.32). Distance from the sample surface to the center of the absorbing layer was determined at six equidistant positions in each image.

Finally, thin vertical sections were cut from the sample using a pair of blades and placed onto a clean microscope slide. The sections were inspected under a microscope at magnifications 4, 20, and 40, and photographed using a charge-coupled device (CCD) camera (resolution 552×744). Depth of the absorbing layer was determined from the microphotographs at ten locations per sample.

9.1.2 Experimental results

Pulsed photothermal profiling

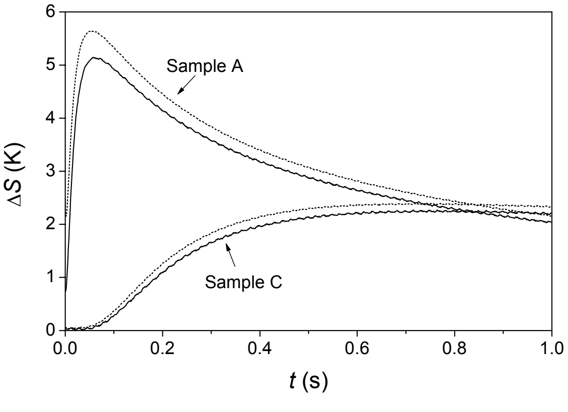

Figure 10.2: PPTR signals acquired from agar gel samples A and C using the entire spectral band ($\lambda = 3.0$–5.6 μm; *dashed lines*) and the reduced spectral band (4.5–5.6 μm; *solid lines*).

Figure 9.2 presents PPTR signals acquired from samples A and C. PPTR signals acquired using the entire spectral band (λ = 3.0–5.6 µm; *dashed lines*) differ in shape from those obtained using the reduced spectral band (λ = 4.5–5.6 µm; *solid lines*).

Noise amplitude in PPTR signals is $NE\Delta T$ = 6.5 and 10.9 mK for the full and reduced spectral band, respectively. *SNR* values are summarized in Table 9.1 for all measured PPTR signals.

Table 9.1: Signal-to-noise ratios (*SNR*) for PPTR signals obtained from four agar gel samples (A–D) using the full (*left column*) and reduced spectral bands (*right column*).

	SNR	
Sample	λ = 3.0–5.6 µm	λ = 4.5–5.6 µm
A	496	245
B	456	285
C	295	155
D	482	277

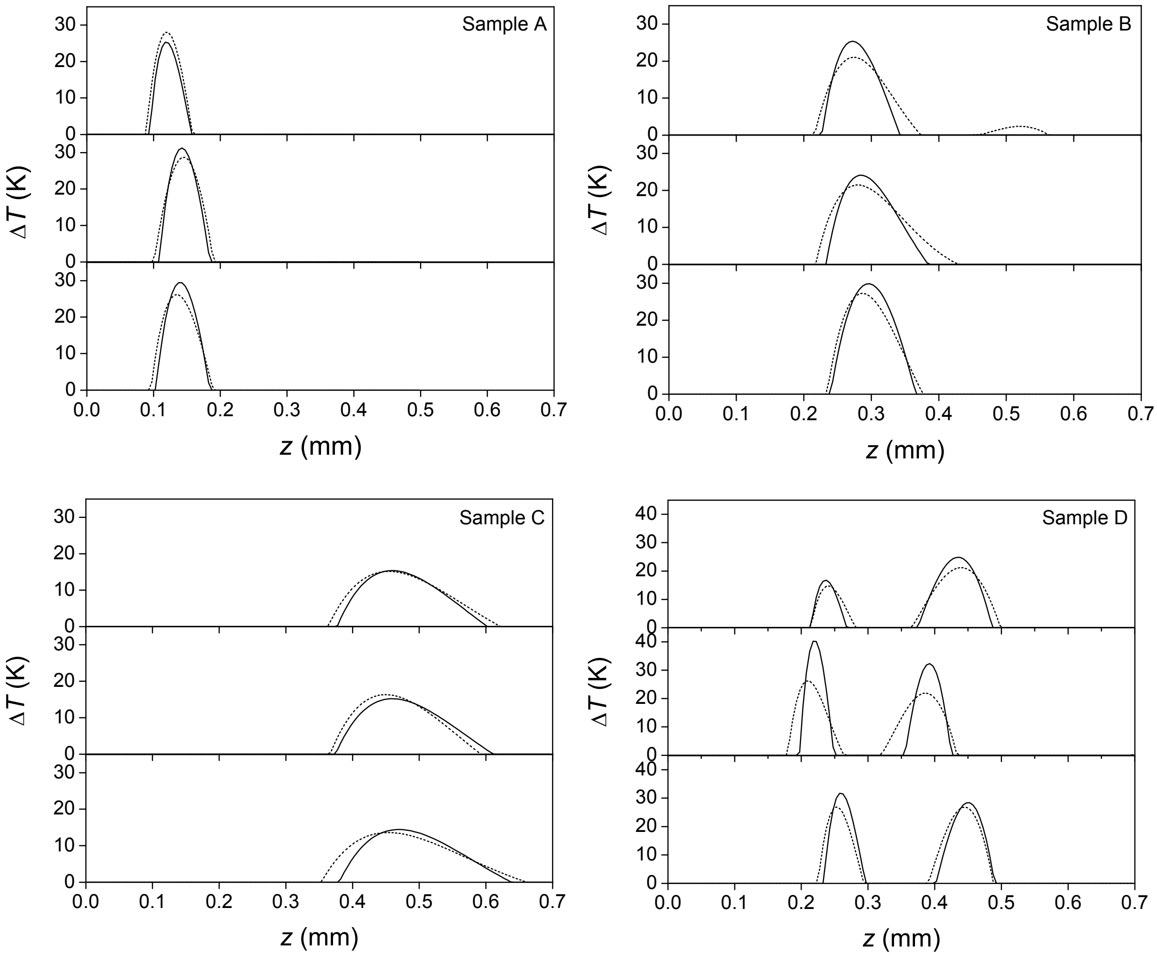

Figure 9.3: Reconstructed temperature profiles from three sites on samples A–D. Corresponding PPTR signals were obtained using the full-spectrum acquisition (λ = 3.0–5.6 µm, *dashed line*) and reduced-spectrum acquisition (λ = 4.5–5.6 µm, *solid line*), respectively.

Figure 9.3 presents temperature profiles reconstructed from PPTR measurements on three different sites on samples A–D, using the entire (*dashed line*) and reduced spectral band (*solid line*). Peak temperature depths *Z* determined on the same site with the two approaches do not differ significantly. The observed variation between different sites on the same sample is due to non-uniform thickness of the superficial gel layer. Yet, temperature profiles obtained with the reduced-spectrum acquisition appear narrower as compared to the full-spectrum acquisition. This effect is particularly evident in samples A and D.

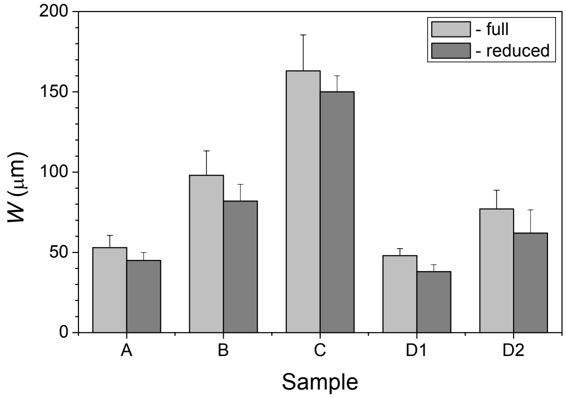

Figure 9.4: Average widths of absorbing layers *W* and standard deviations (*error bars*) for samples A–C and both absorbing layers in sample D (D1 and D2). Temperature profiles were reconstructed from PPTR signals acquired using the full-spectrum (*light gray*) and the reduced-spectrum acquisition (*dark gray*).

Table 9.2: Average peak temperature depths (*Z*) and full-widths at half-maximum (*W*) of the absorbing layers as determined for the full- (*left column*) and reduced-spectrum acquisition (*right column*).

Sample		$\lambda = 3.0–5.6$ μm		$\lambda = 4.5–5.6$ μm	
		Z (μm)	*W* (μm)	*Z* (μm)	*W* (μm)
A		123	45	126	40
		146	55	143	45
		135	60	138	50
B		276	95	273	70
		283	115	278	90
		288	85	288	85
C		448	165	458	140
		453	140	458	150
		453	185	468	160
D	1st	243	45	223	36
		253	53	258	35
		208	46	213	43
	2nd	443	90	431	77
		443	75	453	48
		388	67	396	61

Average peak temperature depths *Z* and full-widths at half-maximums *W* as determined from all test sites using both experimental approaches are summarized in Table 9.2. Depths *Z* determined using the full-spectrum reconstruction results do not differ significantly from depths determined from the reduced-spectrum acquisition. In samples A and B, the difference between the corresponding depths is smaller than the temperature profile discretization ($\Delta z = 5$ μm), and slightly larger in samples C and D (~10 μm). But, lobe widths *W* are significantly larger when the full-spectrum acquisition is used (Table 9.2, *left column*), as compared to reduced-spectrum acquisition (*right column*).

This difference in the broadening effect is illustrated in Figure 9.4, where average widths W and standard deviations are presented for all samples and both acquisition approaches. Clearly, widths W for the reduced-spectrum acquisition (*dark gray*) are smaller as compared to widths for the full-spectrum acquisition (*light gray*).

Optical coherence tomography and histology

An OCT cross-sectional image of sample A (Fig. 9.5a) shows clearly the sample surface (upper arrow) and the absorbing layer (lower arrow) due to strong scattering of incident laser light at these two boundaries. Blurring of both boundary lines, which amounts to ~20 μm precludes, accurate and reliable determination of the top layer's thickness. If the center of each line is selected to represent the boundary location, the average depth of the absorbing layer is determined as 120 μm with a standard deviation of 15 μm. Sample B (Fig. 9.5b) displays the largest variation of the top layer thickness, which is determined as 290 ± 32 μm.

Characteristic "ringing" artifacts are present around the surface line in the image of sample D (Fig. 9.5c; top arrow). Nevertheless, both absorbing layers are easily discernible (mid- and bottom arrow, respectively), and their average depths are determined at 240 and 412 μm. Pronounced optical scattering due to TiO_2 particles in the gel substrate underneath the deeper absorbing layer is clearly visible in the image. The OCT results from all samples are presented in Table 9.3.

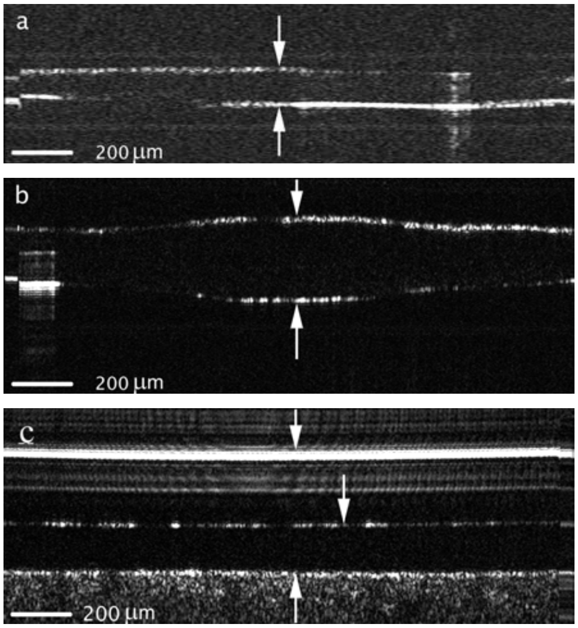

Figure 9.5: OCT images of tissue phantoms: (a) sample A and (b) sample B. The upper arrow indicates the sample surface, and the lower one indicates the absorbing layer. (c) Sample D: The middle arrow indicates the first absorbing layer, and the bottom one indicates the deeper absorbing layer. The substrate (*underneath the latter*) shows scattering due to TiO_2 particles.

Figure 9.6a presents histology of sample C under an optical microscope. Sample surface is indicated by the top arrow. Carbon powder granules are confined to the boundary between the top agar layer and the thicker substrate layer (note the 500 μm scale bar). The absorbing layer depth varies with location, resulting in an average value of 450 μm with a standard deviation of 30 μm.

Histology of sample D is presented in Fig. 9.6b. The upper arrow indicates the sample surface and the middle arrow the first absorbing layer. The optically scattering substrate layer underneath the second absorbing layer (bottom arrow) appears darker in this transillumination microphotograph. The absorbing layer depths as determined from histology in all samples are presented in Table 9.3.

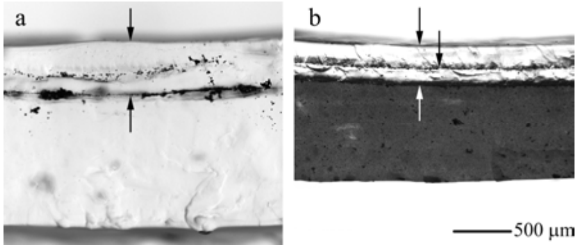

Figure 9.6: Histology of (a) sample C: The upper arrow indicates the sample surface, and the lower arrow indicates the absorbing layer. (b) Sample D: The upper arrow indicates the sample surface, the middle arrow the upper absorbing layer, and the bottom arrow the deeper absorbing layer. The substrate layer in sample D appears darker because of pronounced optical scattering (microscope objective, 4×).

Table 9.3: Average depths and widths of the absorbing layers as determined with three measurement techniques.

Sample	PPTR,3–5 μm		PPTR,3–5 μm		OCT		Histology
	Z (μm)	*W* (μm)	*Z* (μm)	*W* (μm)	*Z* (μm)	*W* (μm)	*Z*(μm)
A	135 ± 12	53 ± 8	136 ± 9	45 ± 5	120 ± 15	20	125 ± 15
B	282 ± 6	98 ± 15	280 ± 8	82 ± 10	290 ± 32	20	287 ± 15
C	451 ± 3	163 ± 23	461 ± 6	150 ± 10	472 ± 15	30	450 ± 30
D 1st	235 ± 24	48 ± 4	231 ± 24	38 ± 4	240 ± 3	40	200 ± 4
2nd	425 ± 32	77 ± 12	427 ± 29	62 ± 15	412 ± 7	40	340 ± 4

9.2 Numerical simulation

9.2.1 Methods

Initial temperature profiles in our numerical simulation have a hyper-Gaussian form: $\Delta T(z, 0) = \Delta T_0 \exp[-2\,(z-z_0)^4/\mathrm{w}_0^4]$. To simulate the experimental data, we select the parameter values $\Delta T_0 = 30$ K and $w_0 = 30$ μm and set z_0 to 133 μm (object A), 282 μm (object B), and 468 μm (object C). An additional test profile is composed of two hyper-Gaussian lobes of width w_0 centered at $z_1 = 223$ μm and $z_2 = 403$ μm (object D). The corresponding vectors $\boldsymbol{T}_0$ consist of 140 values evaluated at equidistant depths within a depth of 0.7 mm. Theoretical signals vectors $\boldsymbol{S}_0$ are calculated from $\boldsymbol{T}_0$ using Eq. (2.11). These have 1083 components which represent PPTR signal values acquired at a sampling rate of 1083 s^{-1}.

We simulated different spectral acquisition bands, with the lower wavelength limit λ_l varied from 3.0 to 5.0 μm and the upper wavelength limit fixed at the InSb radiation detector cut-off wavelength (Fig. 9.1), $\lambda_h = 5.6$ μm. The corresponding kernel matrices $\boldsymbol{K}$ are calculated by dividing each spectral acquisition band into N intervals of width 0.02 μm and adding up their contributions using (6.1), where $\mu(\lambda)$ is IR absorption spectrum of agar gel.

Each theoretical PPTR signal $\boldsymbol{S}_0$ is augmented by realistic noise. To calculate noise equivalent temperature rise $NE\Delta T$ for each simulated spectral band, we must first determine the total noise amplitude n_t. In the following, we apply the parameters of the experimental system: active area of the detector $A = 1.44 \times 10^{-2}$ cm^2, collection half angle $\theta = 11.3°$, frequency bandwidth $\Delta f = 1000$ Hz, and baseline temperature $T_b = 298$ K. Peak responsivity of the InSb radiation detector is estimated to $R_p = 3.0$ A/W. For simplicity, we set both ε and C to 1 (Eq. 3.11), because their influence on the simulation results is minimal. Using the relation, which follows from (2.6) and (3.11)

$$NE\Delta T = \frac{n_\mathrm{t}}{C\,\varepsilon\,A\sin^2\theta \int_{\lambda_\mathrm{l}}^{\lambda_\mathrm{h}} R(\lambda)\,B_\lambda'(T_\mathrm{b})\,\mathrm{d}\lambda} \tag{9.1}$$

we can determine n_t from the experimentally determined $NE\Delta T$ values (6.5 and 10.9 mK for spectral bands of λ = 3.0–5.6 μm and 4.5–5.6 μm, respectively). The result is almost identical for both spectral bands, $n_\mathrm{t} = 3.0 \times 10^{-10}$ A, since the shot noise amplitudes n_sh computed by using (3.4) and (3.11) are markedly smaller than n_t ($n_\mathrm{sh} = 2.0 \times 10^{-11}$ A and 1.7×10^{-11} A for λ_l = 3.0 and 4.5 μm, respectively). Hence, we calculate $NE\Delta T$ using (9.1) with $n_\mathrm{t} = 3.0 \times 10^{-10}$ A for all simulated spectral bands. In addition, the presence of $1/f$ noise is characterized by a corner frequency f_c = 330 Hz and an exponent $\alpha = 1$ (Eq. 3.5), so we simulate noise that contains appropriate contributions of zero-mean white noise and $1/f$ noise.

Initial temperature profiles $\boldsymbol{T}$ are reconstructed from simulated PPTR signals using the monochromatic approximation. Elements of the monochromatic kernel matrix $\boldsymbol{K}$ (2.9) are calculated using the effective absorption coefficient values μ_eff, determined separately for each spectral band as presented in Chapter 6.1.2.

Because reconstruction results are very sensitive to specific noise realizations, each theoretical signal $\boldsymbol{S}_0$ is augmented with 10 different realizations of noise and the results are analyzed statistically.

9.2.2 Simulation results

Simulated PPTR signals for test objects A–C are presented in Fig. 10.6 for acquisition spectral bands with λ = 3.0–5.6 μm, 4.5–5.6 μm and 5.0–5.6 μm. The narrowest spectral band (*right*) presents a significantly larger $NE\Delta T$ as compared to the entire spectral band (*left*).

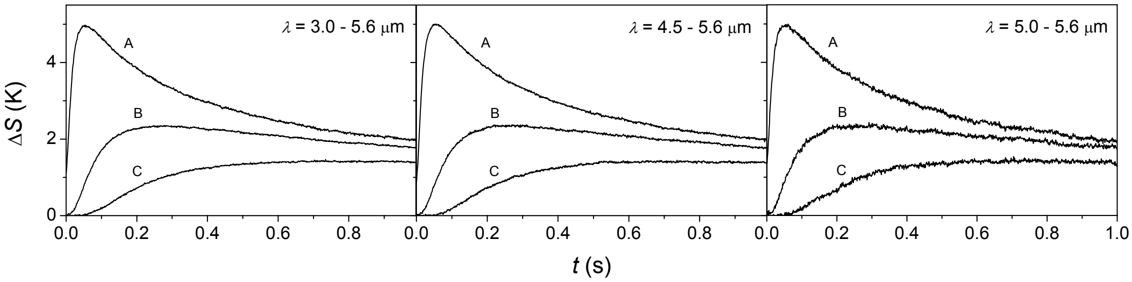

Figure 9.6: Simulated PPTR signals for test objects A–C and spectral bands λ = 3.0–5.6 μm (*left*), 4.5–5.6 μm (*center*) and 5.0–5.6 μm (*right*). All signals are augmented by realistic noise.

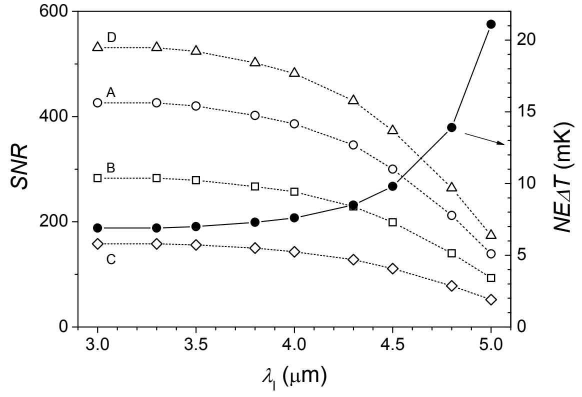

Figure 9.7: $NE\Delta T$ for the simulated spectral acquisition bands (*solid circles*) as a function of λ_l. *SNR* of the simulated PPTR signals (*open symbols*) decreases with λ_l for all test objects (A–D).

Figure 9.7 presents the $NE\Delta T$ values (9.1) as a function of λ_l (*solid circles*). $NE\Delta T$ increases monotonically from 6.9 mK at λ_l = 3.0 μm to 21.1 mK at λ_l = 5.0 μm. Consequently, SNR of simulated PPTR signals decreases with λ_l for all test objects (*open symbols*).

Effective IR absorption coefficients μ_{eff} (6.3) for the simulated spectral acquisition bands are presented in Fig. 9.8. The values μ_{eff} vary between 25.0 mm^{-1} and 30.2 mm^{-1}, as dictated by spectral dependences of $\mu(\lambda)$, $R(\lambda)$ and $B_\lambda(T_b)$ in the corresponding spectral bands.

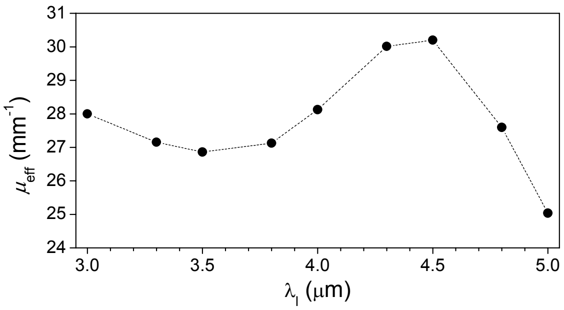

Figure 9.8: Effective IR absorption coefficient μ_{eff} as a function of λ_l for the simulated spectral bands.

Figure 9.9 presents statistical analysis of reconstruction results for three spectral acquisition bands: λ = 3.0–5.6 μm (*left column*), 4.5–5.6 μm (*center*), and 5.0–5.6 μm (*right*). In each panel, black lines connect the average temperature values and light-gray bars indicate standard deviations. The actual test objects are depicted for comparison (*dark-gray lines*).

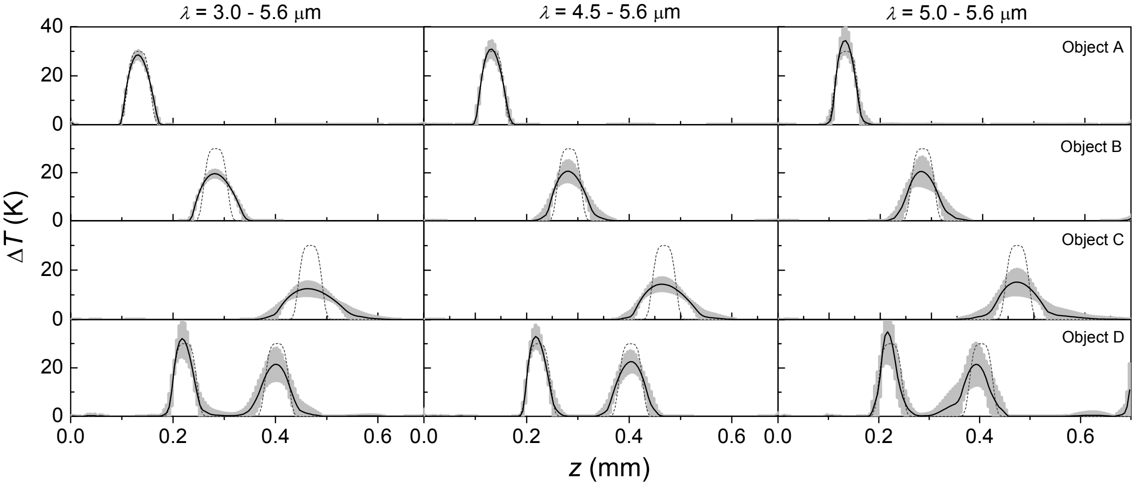

Figure 9.9: Average temperature profiles (*black lines*) and standard deviations (*light-gray bars*) reconstructed from 10 simulated PPTR signals with different noise realizations. Images of four test objects (*see the labels*) are reconstructed from PPTR signals with spectral bands: λ = 3.0–5.6 μm (*left*), 4.0–5.6 μm (*center*) and 5.0–5.6 μm (*right*). The actual test objects are plotted for comparison (*dashed lines*).

For the reduced spectral bands (*center and right*), reconstructed temperature profiles of object A (*top row*) are narrower and higher as compared to the full spectral band (*left*). Similar trends are observed for objects B and C (*2nd and 3rd row, respectively*), while object D (*bottom row*) is reconstructed optimally, when the spectral band with λ = 4.5–5.6 μm is used. But spectral band reduction compromises the stability of the reconstruction results (i.e., increased standard deviation), due to reduced SNR.

Figure 9.10a presents relative image errors δ as a function of λ_l. For object A (*circles*), the minimal average error is obtained at λ_l = 3.8 μm (δ = 0.088; *note the arrow*). With λ_l increased above λ_l = 4.0 μm, δ increases progressively due to decreasing SNR (δ = 0.19 at λ_l = 5.0 μm). With λ_l decreased below 3.8 μm, δ increases monotonically due to increasing deficiency of the monochromatic approximation, reaching $\delta = 0.14$ at $\lambda_l = 3.0$ μm. The same trend is present also for standard deviation of δ. Standard deviation presents a minimum at $\lambda_l = 3.8$ μm ($\sigma_\delta = 0.02$) and significantly increases when spectral band is ether broadened ($\sigma_\delta = 0.05$ at $\lambda_l = 3.0$ μm) or narrowed ($\sigma_\delta = 0.10$ at $\lambda_l = 5.0$ μm).

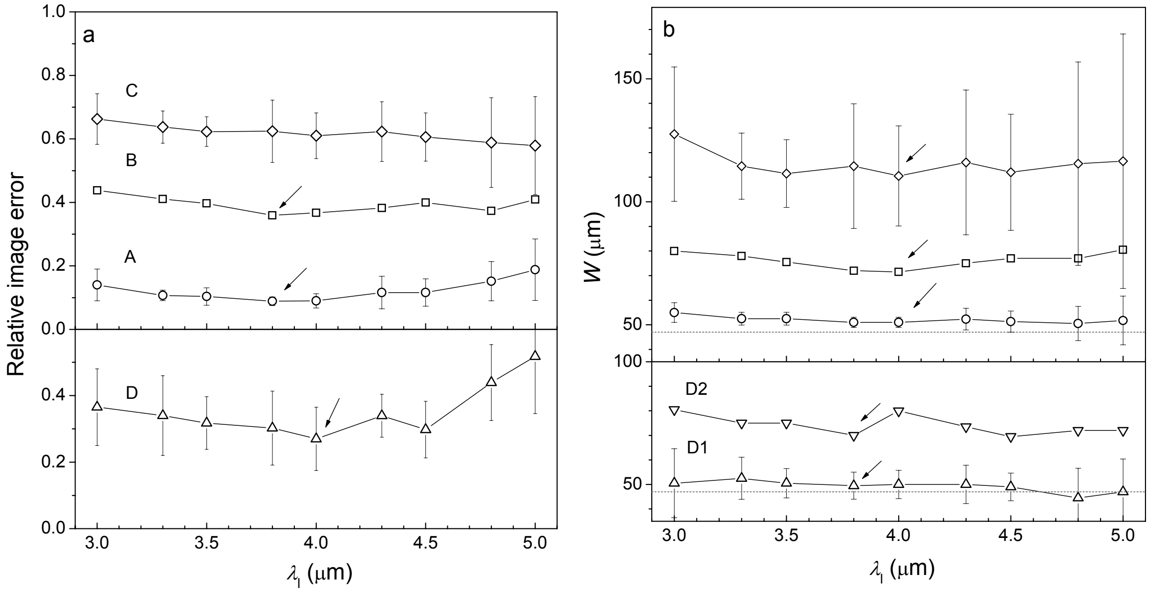

Figure 9.10: (a) Relative image error δ as a function of λ_l for test objects A (*circle*), B (*square*), C (diamond) and D (*triangle*). (b) Analogous results for the full-width at half maximum of reconstructed temperature peaks (*W*). The widths of both peaks are analyzed for object D (D1, D2; bottom). Standard deviations are presented as error bars. Dotted lines in (b) indicate the actual object width, $W = 47$ μm. Arrows indicate minimums of δ and *W*.

Similar trend is observed for object B (Fig. 9.10a, *squares*), where the minimum $\delta = 0.36$ at $\lambda_l = 3.8$ μm is markedly larger as compared to test object A due to the broadening. Standard deviation σ_δ tends to increase with λ_l ($\sigma_\delta = 0.04$, 0.08 and 0.19 at $\lambda_l = 3.0$, 3.8 and 5.0 μm, respectively). Relative image errors δ for object C (*diamonds*) decrease with λ_l, albeit this trend is almost concealed by large standard deviations σ_δ.

The minimum of δ for test object D (*bottom*) is obtained at $\lambda_l = 4.0$ μm ($\delta = 0.27$; arrow), while values within the range $\lambda_l = 3.5$–4.5 μm can be considered adequate due to large standard deviations ($\sigma_\delta \sim 0.11$). For λ_l outside of this range, δ and its standard deviation both tend to increase, in particular toward larger λ_l ($\delta = 0.52 \pm 0.17$ at $\lambda_l = 5.0$ μm).

The difference between δ of full-spectrum acquisition and δ of the filtered approach with $\lambda = 4.0$–5.6 μm (Table 10.4) is most prominent for objects A ($\delta_{\mathrm{full}} = 14\%$ and $\delta_{\mathrm{reduced}} = 9\%$) and D ($\delta_{\mathrm{full}} = 37\%$ and $\delta_{\mathrm{reduced}} = 27\%$).

As demonstrated in Figure 9.10b, the reconstructed temperature profiles are in general broader than the test objects ($W = 47$ μm; *note the dashed line*). For test object A (*circles*) the optimal result ($W = 51$ μm; *arrow*) is fairly accurate. The indicated optimal degree of spectral filtering ($\lambda_l = 3.8$–4.0 μm) is the same as that from analysis of image errors (Fig. 9.10a, *circles*), although the minimum is less pronounced. The image widths *W* increase in particular for broader spectral bands (lower λ_l), and standard deviations σ_W increase when λ_l is changed from the optimal range in either direction (but more so toward larger λ_l).

The reconstructed images of test objects B and C (Fig. 9.10b, *squares* and *diamonds*, respectively) are much broader than for object A. The closest match ($W = 72$ μm and 111 μm, respectively) is obtained at $\lambda_l = 4.0$ μm and the general trends appear equivalent to those observed for object A, although they are almost concealed by large standard deviations.

For the two-lobed test object D (Fig 9.10b, bottom), the results from the first peak (*up triangles*) suggest the optimal value around λ_l = 3.5–4.5 μm, if both widths W and their standard deviations are considered. For the second peak, the trends in $W(\lambda_l)$ are concealed by large standard deviations σ_W, which tend to increase toward both ends of the explored spectral range.

Average peak temperature depths Z and widths W (together with standard deviations) are presented in Table 9.4 for all test objects and spectral bands with λ_l = 3.0 (unfiltered), 4.0 (near-optimal) and 4.5 μm (as used in the experiments; section 9.1). The depths Z deviate from the actual central depths z_0 by 1% (object C) or less (objects A, B, and D2), and ~2% for the first peak of object D, regardless of the spectral acquisition band. When we compare the optimal results to widths W determined for the full spectral band (λ_l = 3.0 μm), we find that spectral filtering reduces W by 7 ± 1%, 10 ± 3%, 13 ± 8%, 2 ± 1% and 14 ± 11% for test objects A, B, C, the 1st peak and the 2nd peak of D, respectively.

Table 9.4: Average depths Z and widths W of reconstructed temperature profiles determined for the full (λ = 3.0–5.6 μm), near-optimal (4.0–5.6 μm) and reduced spectral band as used in the experiments (4.5–5.6 μm). The actual width W for all objects is 47 μm, the central depth z_0 is given in the first column.

Sample			3.0–5.6 μm		4.0 –5.6 μm		4.5–5.6 μm	
		z_0 (μm)	Z (μm)	W(μm)	Z (μm)	W(μm)	Z (μm)	W(μm)
A		133	133 ± 0	55 ± 4	133 ± 0	51 ± 2	132 ± 1	51 ± 4
B		283	283 ± 0	80 ± 7	282 ± 2	72 ± 8	281 ± 3	77 ± 18
C		468	462 ± 0	128 ± 27	465 ± 3	111 ± 20	464 ± 2	112 ± 24
D	1st	223	218 ± 2	51 ± 14	219 ± 2	50 ± 6	218 ± 3	49 ± 6
	2nd	403	403 ± 5	81 ± 20	405 ± 4	70 ± 13	405 ± 5	72 ± 12

In contrast, spectral filtering has a larger effect on image width, W. As illustrated in Fig. 9.11, the reconstructed images are on average broader and more sensitive to the presence of noise when using the full spectral band (λ_l = 3.0 μm) as compared to either narrowed spectral band (λ_l = 4.0 μm or 4.5 μm), for all test objects. The difference between the latter spectral bands is not very large, although the near-optimal spectral band (λ_l = 4.0 μm) yields smaller widths W (except for the superficial peak in sample D, D1), and smaller standard deviations σ_W (except for the deep peak in sample D, D2).

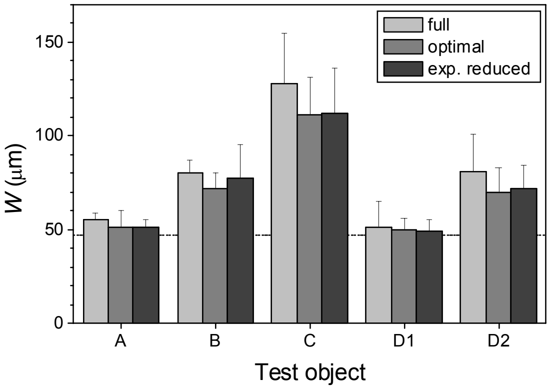

Figure 9.11: Average widths W of temperature lobes in reconstructed images of all test object for the full (λ_l = 3.0 μm), near-optimal (λ_l = 4.0 μm) and reduced spectral band as used the experiments (λ_l = 4.5 μm). Bars indicate standard deviations, dotted line indicates the correct object width (W = 47 μm).

Quality of reconstructed image is in general diminished by two independent effects, deficiency of monochromatic approximation and the presence of noise in PPTR signals. To highlight their respective roles, we perform analysis for test objects A with varied peak temperature, ΔT_0 = 5–60 K. *SNR* values of simulated PPTR signals for these test objects are presented in Fig. 9.12a.

As seen in Fig. 9.12b, reconstruction of the object with the lowest amplitude (ΔT_0 = 5 K) is optimal when using the full spectral band (3.0–5.6 µm). Reconstruction of this object is compromised primarily by the high level of noise in the PPTR signal (SNR = 70). For all other test objects, image errors show distinct minimums (around λ_{l} = 4.0–4.5 µm) when reduced spectral acquisition bands are used.

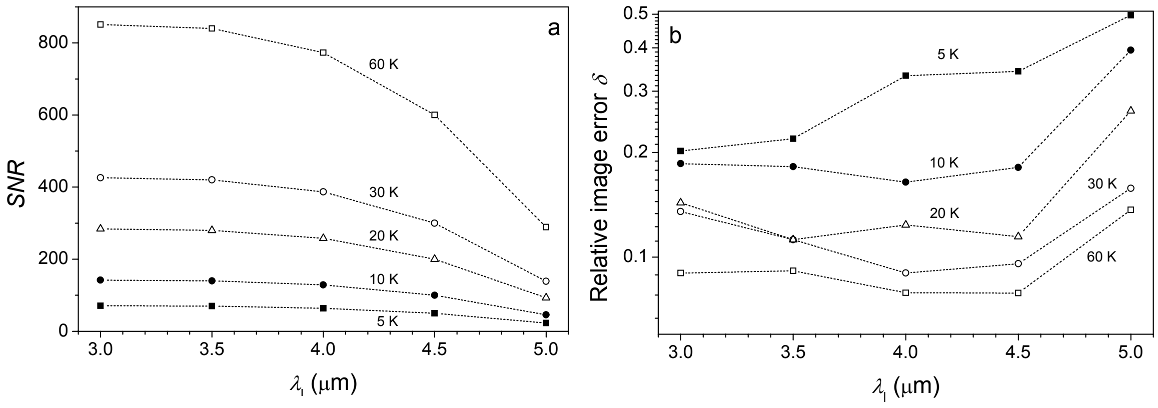

Figure 9.12: (a) *SNR* values for test objects with peak temperature ΔT_0 from 5 K to 60 K. (b) Relative image errors δ (*in logarithmic scale*) for the spectral bands with λ_{l} = 3.0, 3.5, 4.0, 4.5 and 5.0 µm.

Figure 9.13 presents statistical analysis of the widths *W* for the same range of amplitudes (ΔT_0 = 5–60 K) and three acquisition spectral bands. Similarly to Fig. 9.11, the full-spectrum approach (λ = 3.0–5.6 µm) invariably yields larger widths *W* than the reduced-spectrum approach, thus resulting in worse reconstructions. In contrast to relative image error δ (Fig. 9.11b), widths *W* determined for the experimental reduced spectral band (λ = 4.5–5.6 µm) are more accurate and feature smaller standard deviations as compared to the theoretically optimal spectral band (λ = 4.0–5.6 µm), although the difference does not appear significant

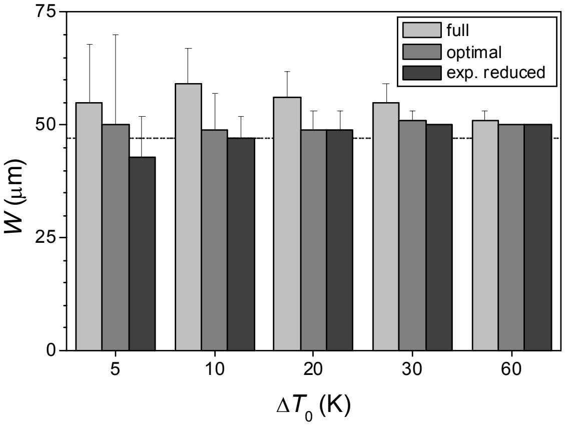

Figure 9.13: Average widths *W* and standard deviations for test objects with peak temperature ΔT_0 = 5–60 K and for the full (λ_{l} = 3.0 µm), optimal (λ_{l} = 4.0 µm) and experimental reduced spectral bands (λ_{l} = 4.5 µm). Bars indicate standard deviations, dotted line indicates the correct object width (*W* = 47 µm).

9.3 Discussion

The depths of peak temperature *Z* in tissue phantoms reconstructed from PPTR measurements using the full and the reduced-spectrum acquisition are very similar (Tables 9.2 and 9.3). The absorbing layer depths assessed from PPTR measurements matched adequately the results from OCT and histology (see Table 9.3). These findings are supported by our numerical simulation results where peak temperature depths Z deviate from the actual object depths z_0 by less than 2% (see Table 9.4). The experimental and numerical simulation results confirm that selection of the spectral band does not significantly influence the accuracy of peak temperature depth, Z.

Experimental results show that appropriate spectral filtering of PPTR signals improves the quality of reconstructed temperature profiles. In sample A, temperature profiles reconstructed from experimental PPTR signals with the reduced-spectrum acquisition are significantly narrower (W = 45 ± 5 μm) as compared to the full-spectrum acquisition (W = 53 ± 8 μm). Hence, spectral filtering reduces W by 15 ± 4% in sample A (see Table 9.2). The advantage of spectral filtering is less apparent, but still present, in samples B and C (W is reduced by 16 ± 7% and 8 ± 3% for samples B and C, respectively). Samples B and C feature deeper absorbing layers, so the temperature profiles are increasingly broadened regardless of the spectral acquisition band, as presented in Chapter 11. In sample D, with two absorbing layers (Table 9.2), both temperature peaks obtained with spectrally narrowed acquisition are on average markedly narrower than for the full-bandwidth approach (by 21 ± 5% and 20 ± 10% for the 1st and the 2nd peak, respectively).

Similar trends are found also in results of numerical simulation. For all test objects, the minimal differences between determined widths W and the actual value W = 47 μm are obtained for the spectral acquisition bands with λ_l = 3.8–4.0 μm. Standard deviations of the widths σ_W are also smallest for $\lambda \approx$ 4.0–5.6 μm (Table 9.4). This indicates that appropriate spectral filtering improves robustness of PPTR temperature profiling, despite the related decrease in SNR. The accuracy of determined width W in general decreases with increasing SNR (Fig. 9.13). However, for a given test object and temperature rise optimal widths W and minimal standard deviations σ_W are obtained with appropriate filtering. Thus, we conclude that appropriate spectral filtering (e.g., λ_l = 3.8–4.0 μm) reduces the profile broadening in a large range of realistic SNR values.

For test objects with different ΔT_0, distinct minimums are present for narrowed spectral bands (i.e., 4.0–5.6 μm, see Fig. 10.12b), except for the object with ΔT_0 = 5 K. For the latter, the high amount of noise in simulated PPTR signals concealed the dependence of δ on spectral band.

The effects of noise and monochromatic approximation deteriorate reconstruction quality in PPTR profiling. The former is most expressed for narrow spectral bands, while the latter is most expressed for broad spectral bands (see Chapter 6). Thus in general, an optimal spectral band exists which yields a minimal reconstruction error. Results of the numerical simulations suggest that the optimal spectral acquisition bandwidth is λ_l = 3.8–4.2 μm for the simulated objects and PPTR system. In general, the optimal spectral band depends on object structure, peak temperature and experimental system characteristics.

9.4 Conclusions

In PPTR temperature profiling of agar tissue phantoms, spectral filtering reduces the reconstruction error δ and broadening of temperature peaks, especially for shallower and more complex absorbing structures. A suitable amount of spectral filtering is thus beneficial, despite the associated reduction of SNR. However, spectral filtering is not beneficial, when PPTR signals are significantly deteriorated by noise. For the simulated objects and PPTR system, results of numerical simulations suggest an optimal spectral band with λ_l = 3.8–4.2 μm. In general, the optimal spectral band depends on specifics of experimental system, spectral property of tissue and temperature profile.

Chapter 10

Spectral filtering in collagen samples

In the previous chapter we showed that appropriate spectral filtering improves reconstruction results, when the monochromatic approximation is used. Albeit this approximation reduces computational costs, it results in the deficiency, which deteriorates reconstruction results, especially for absorbing structures close to the sample surface. But when the exact IR absorption spectrum is known, a spectrally composite kernel matrix can be computed and applied to reconstruction of temperature profiles.

The study presented in Chapter 9 involved agar tissue phantoms, which are different from our intended application, temperature profiling in human skin. The differences include different IR absorption spectrum, heat diffusion constant and complexity of the temperature profile. In this chapter we present a follow-up study involving numerical simulation and experimental studies on collagen tissue phantoms, which more realistically resemble human skin. Besides the monochromatic approximation we use also spectrally composite kernel matrices and compare reconstruction results obtained by these two approaches.

10.1 Numerical simulation

The initial temperature profiles in our numerical simulation have a hyper-Gaussian form: $\Delta T(z, 0) = \Delta T_0 \exp[-2 (z-z_0)^4/\mathrm{w}_0^4]$. We set the parameter values $\Delta T_0 = 30$ K and $w_0 = 33$ µm and choose z_0 to be 50 µm (test object A), 110 µm (B), 280 µm (C), 430 µm (D) or 640 µm (E). An additional test profile (AC) is composed of two hyper-Gaussian lobes of width w_0 centered at $z_1 = 50$ µm and $z_2 = 280$ µm. Theoretical signal vectors $\boldsymbol{S}_0$ are calculated from $\boldsymbol{T}_0$ using Eq. (2.11), and have 1000 components, which represent PPTR signal values acquired at a sampling rate of 1000 s^{-1}.

We simulate different spectral acquisition bands, with $\lambda_\mathrm{l} = 3.0$–5.0 µm and $\lambda_\mathrm{h} = 5.6$ µm (InSb detector; Fig. 3.3). The corresponding kernel matrices $\boldsymbol{K}$ are calculated by dividing each spectral acquisition band into N intervals of width 0.02 µm and adding up their contributions in accordance with (6.1). We use the IR absorption spectrum of gelatin tissue phantoms (Fig. 8.6), and apply thermal parameter values $D = 0.11$ mm^2/s and $h = 0.02$ mm^{-1}.

For comparison of PPTR profiling performance utilizing different spectral acquisition bands, we augment simulated PPTR signals with realistic noise. We use specifications of our PPTR system (chapter 3), determined noise parameters ($n_\mathrm{t} = 3\times10^{-10}$ A, $f_\mathrm{c} = 15$ Hz and $\alpha = 1.3$) and emissivity $\varepsilon = 1$, which is representative of human. Noise-equivalent temperature rises ($NE\Delta T$) are calculated using Eq.(9.1). Because reconstruction results are very sensitive to specific noise realizations, we augment each theoretical signal $\boldsymbol{S}_0$ with 30 different realizations of noise, yielding PPTR signals $\boldsymbol{S}$.

Initial temperature profiles $\boldsymbol{T}$ are reconstructed from simulated PPTR signals $\boldsymbol{S}$ using both the monochromatic kernel matrix, $\boldsymbol{\kappa}$ (2.10) and spectrally composite kernel matrix, $\boldsymbol{K}$ (6.1). Elements of the matrix $\boldsymbol{\kappa}$ are calculated using the effective absorption coefficient values μ_eff (6.3), determined separately for each spectral band. We use the projected υ-method (chapter 4) to reconstruct temperature profiles $\boldsymbol{T}$, which consist of 200 temperature values over a depth range of 1.0 mm (discretization step $\Delta z = 5$ µm).

10.1.2 Results

Simulated PPTR signals $\boldsymbol{S}$ for test objects A–E are presented in Figure 10.1 for spectral acquisition bands of λ = 3.0–5.6 μm (*left*) and λ = 5.0–5.6 μm (*right*).

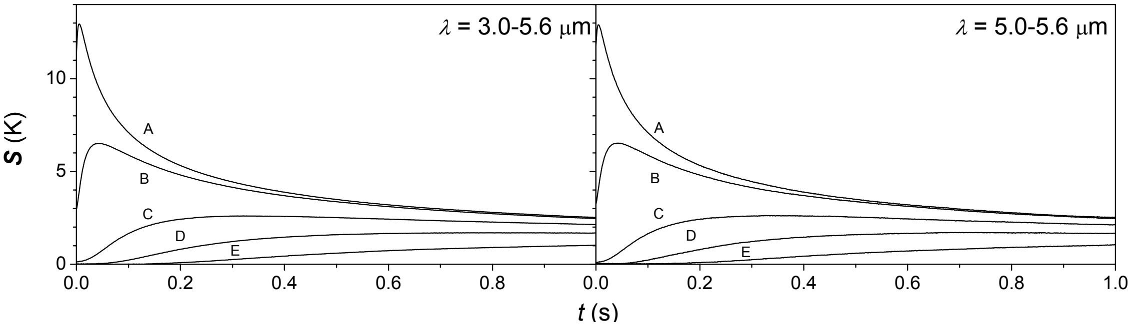

Figure 10.1: Simulated PPTR signals for test objects A–E and spectral bands of λ = 3.0–5.6 μm (*left*) and λ = 5.0–5.6 μm (*right*). All signals are augmented by realistic noise.

Figure 10.2 presents *NE*Δ*T* (9.1) as a function of λ_l (*solid circles*). The values increase from 3.3 mK at λ_l = 3.0 μm to 7.1 mK at λ_l = 5.0 μm. Consequently, SNR computed from simulated PPTR signals decrease with λ_l, albeit not monotonically due to different realizations of 1/f noise (*empty symbols*).

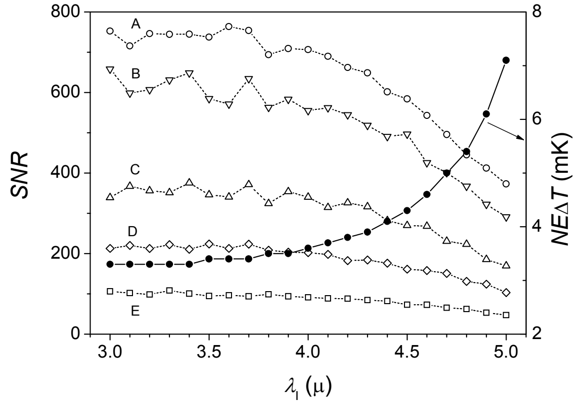

Figure 10.2: *NE*Δ*T* for the simulated spectral acquisition bands (*solid circles*) as a function of λ_l, and *SNR* of the simulated PPTR signals for test objects A–E (*empty symbols*).

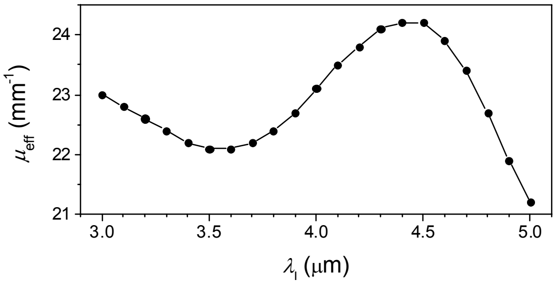

Figure 10.3: Effective IR absorption coefficient μ_{eff} as a function of λ_l.

Effective IR absorption coefficients μ_{eff} (6.2) used in monochromatic reconstruction of temperature profiles are presented in Fig. 10.3. The values lie between μ_{eff} = 21.2 mm^{-1} at λ_l = 5.0 μm and μ_{eff} = 24.2 mm^{-1} at λ_l = 4.5 μm.

Figure 10.4a presents statistical analysis of the reconstruction results for object A. When monochromatic reconstruction is used, the best reconstruction result is obtained for λ = 4.3–5.6 μm (*second row*), albeit corresponding standard deviations is somewhat larger than for λ = 3.0–5.6 μm (*first row*). Spectral reconstruction (λ = 3.0–5.6 μm; *bottom row*) results in temperature profile similar to the optimal monochromatic result, yet with smaller standard deviation. Similar trends as for object A are observed in reconstructed temperature profiles of test objects B–D (Figs. 10.4b–10.4d), except that on average reconstruction results obtained with spectral reconstruction somewhat better resemble the actual objects and feature smaller standard deviations.

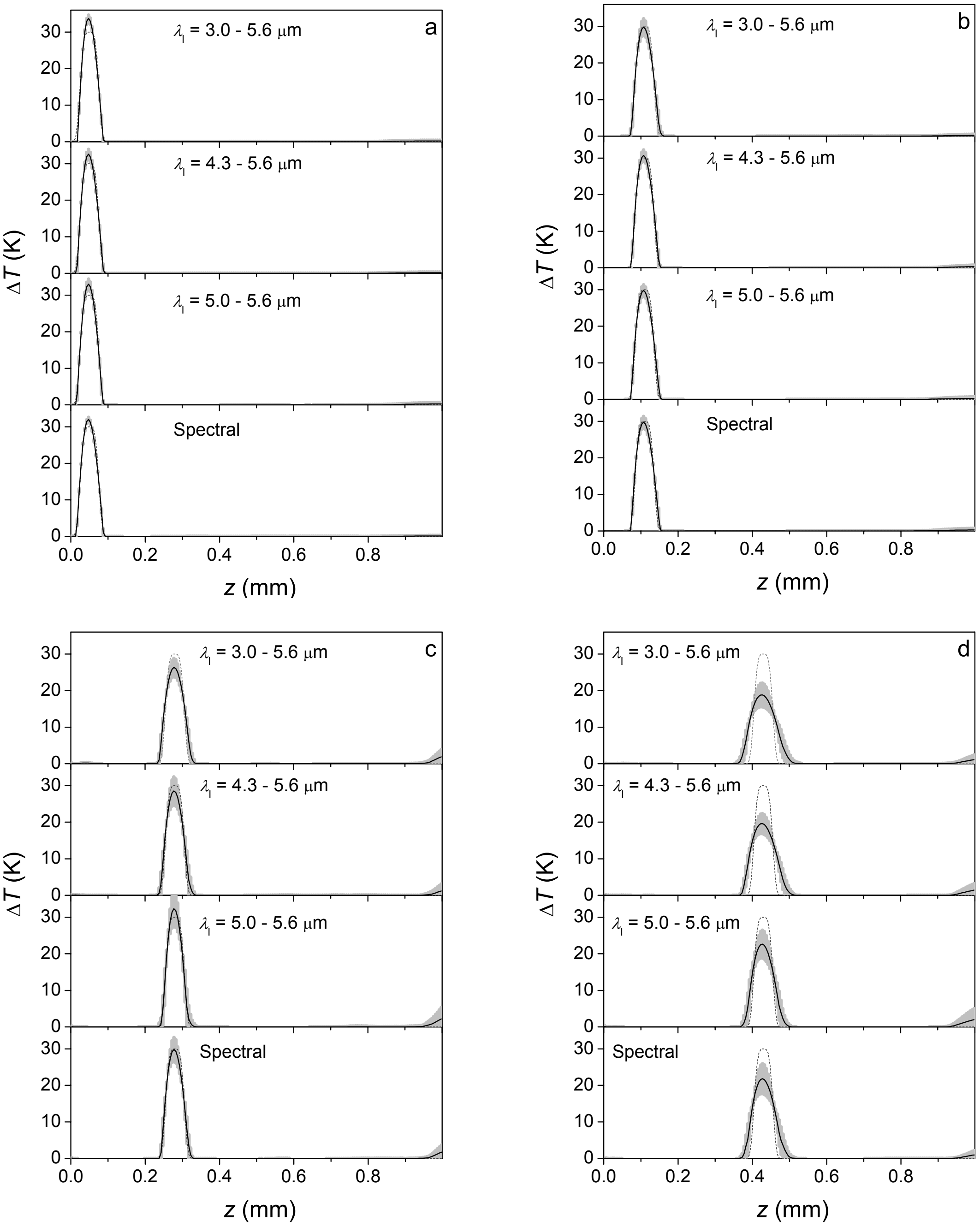

Figure 10.4: Average temperature profiles (*black lines*) and standard deviations (*light-gray bars*) reconstructed from 30 simulated PPTR signals with different noise realizations. Images of test objects (a) A, (b) B, (C), and (d) D are reconstructed from PPTR signals with spectral bands of λ = 3.0–5.6 μm (*first row*), λ = 4.3–5.6 μm (*second row*) and λ = 5.0–5.6 μm (*third row*) using monochromatic reconstruction. Images are reconstructed also using spectral reconstruction and spectral acquisition band λ = 3.0–5.6 μm (*bottom row*). The actual test objects are plotted for comparison (*dashed line*).

Temperature peak depths Z determined from temperature profiles reconstructed by using monochromatic reconstruction are equal to depths Z determined for spectral reconstruction. All depths Z are 2.5 μm smaller than the actual depth z_0 for all test objects. Hence, the results of numerical simulation indicate that PPTR temperature profiling results in accurate temperature peak depths Z when either monochromatic reconstruction with optimal μ_{eff} or spectral reconstruction are used.

Relative image errors δ (Eq. 4.10) for test objects A and B are presented in Fig. 10.5. For object A and monochromatic reconstruction (Fig. 10.5a, *solid circles*), we observe the minimal image error at λ_l = 4.3 μm ($\delta = 0.09 \pm 0.01$; *see arrow*). With λ_l increased above λ_l = 4.3 μm, image error δ and standard deviation σ_δ increase due to increased SNR. However, both δ and σ_δ also increases when λ_l is below λ_l = 4.2 μm, due to increasing deficiency of the monochromatic approximation. For spectral reconstruction, the image error δ does not vary significantly between λ_l = 3.0 and 4.7 μm ($\delta \approx 0.7 \pm 0.01$) (*open circles*), while δ and σ_δ progressively increase with λ_l above 4.7 μm due to increased SNR. In general, spectral reconstruction results in smaller δ and σ_δ, but the difference between the two approaches is small for optimal spectral filtering, λ_l = 4.0–4.5 μm.

For object B and monochromatic reconstruction (Fig. 11.5b, *solid circles*), the minimal image error is obtained at λ_l = 4.4 μm ($\delta = 0.09 \pm 0.02$). However, spectral bands of λ_l = 4.1–4.5 μm yield $\delta \approx 0.10$ and $\sigma_\delta \approx 0.02$, both reasonably small. When spectral reconstruction is used (*open circles*), average δ and σ_δ are almost constant for λ_l = 4.0–4.3 μm, and increase with λ_l above 4.5 μm. Standard deviation σ_δ is smaller for spectral reconstruction in most spectral band than for monochromatic reconstruction. All trends are almost concealed by the large standard deviations for both reconstruction approaches.

For objects C–D, standard deviation σ_δ is even more pronounced as for object B, effectively concealing all trends in δ. Image errors δ and standard deviations σ_δ are similar for both reconstruction approaches: 0.15 ± 0.6, 0.45 ± 0.10, and 0.70 ± 0.12 for test object C, D, and E, respectively.

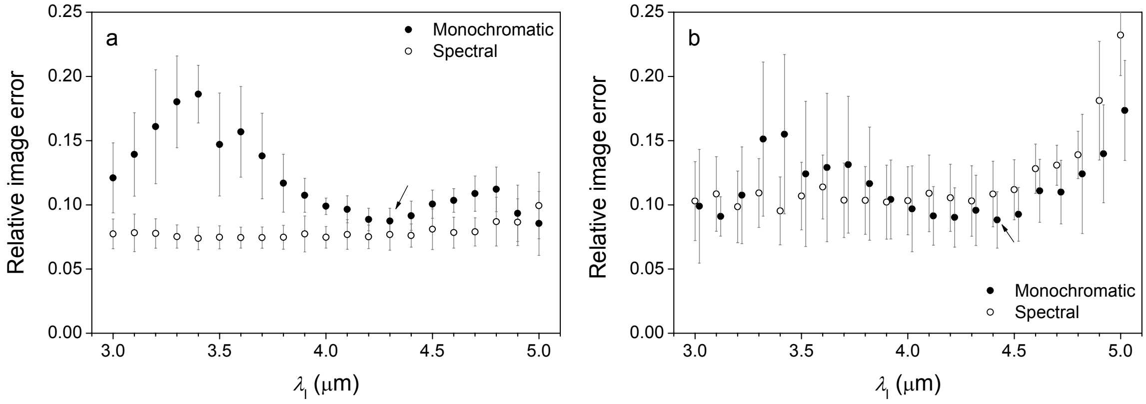

Figure 10.5: Relative image error δ and standard deviation σ_δ (*error bars*) as a function of λ_l for monochromatic (*solid circles*) and spectral reconstruction (*open circles*). Image error δ is determined from temperature profiles of test objects (a) A and (b) B. Arrows indicate optimal λ_l.

Full-widths at half maximum (W) of the reconstructed images are presented in Fig. 10.6 for test objects A and B. For monochromatic reconstruction (Fig. 11.6a, *solid circles*), the reconstructed temperature profiles are narrower than the actual object (W = 50 μm; *dashed line*), except for λ_l = 4.0–4.4 μm, where accurate widths are obtained. In contrast, accurate widths are obtained for all simulated spectral bands when spectral reconstruction is used (*open circles*). For object B, spectral acquisition bands with λ_l = 4.0–4.5 μm yield near optimal width $W \approx$ 51 μm and standard deviation $\sigma_W \approx$ 3 μm when monochromatic reconstruction is used (Fig. 11.6b, *solid circles*). For test objects C–E, all trends are concealed by large standard deviation σ_W ($W \approx$ 54 ± 7, 76 ± 13, and 200 ± 50 for test objects C, D, and E, respectively).

The last parameter determined from the reconstructed temperature profile, peak temperature T_p, is presented in Fig. 10.7. Spectral reconstruction yields peak temperatures T_p closer to the actual temperature amplitude ΔT_0 (30 K; *dashed lines*) as compared to monochromatic reconstruction. For test object A (Fig. 10.7a), monochromatic reconstruction (*solid circles*) results in $T_p \approx 33$ K and standard deviation $\sigma_T = 0.7$ K for $\lambda_l = 4.0$–4.5 μm, while spectral reconstruction (*open circles*) results in $T_p \approx 32$ K and $\sigma_T = 0.7$ K for $\lambda_l = 3.0$–4.5 μm. For test object B (Fig. 10.7b), we obtain $T_p \approx 36$ K and $\sigma_T = 2$ K for $\lambda_l = 4.1$–4.3 μm and monochromatic reconstruction (*solid circles*), but $T_p \approx 34$ K and $\sigma_T = 2$ K for $\lambda_l = 3.0$–4.5 μm. For test objects C–E, the two reconstruction approaches are equally efficient in determination of T_p for all spectral bands.

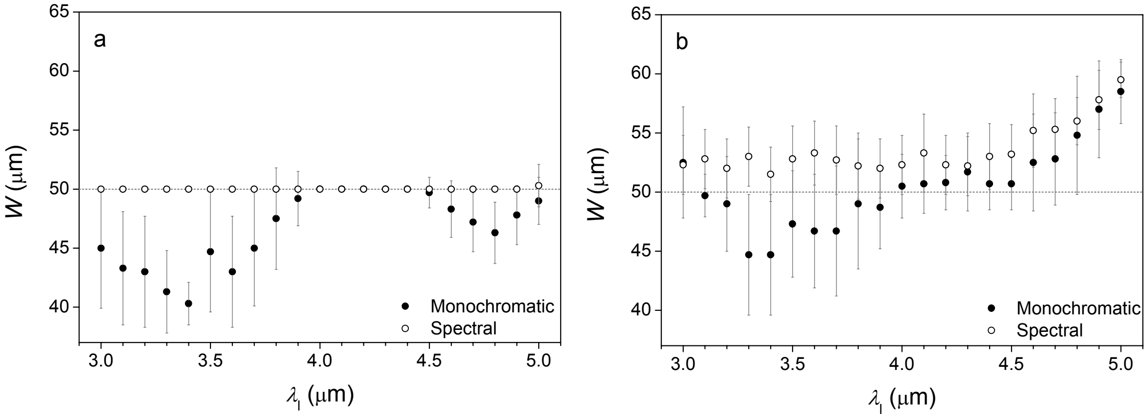

Figure 10.6: Full-widths at half maximum W and standard deviations σ_W (*bars*) as a function of λ_l for monochromatic (*solid circles*) and spectral reconstruction (*open circles*). Width W is determined from temperature profiles of test objects (a) A and (b) B. Dotted lines indicate the actual object width ($W = 50$ μm).

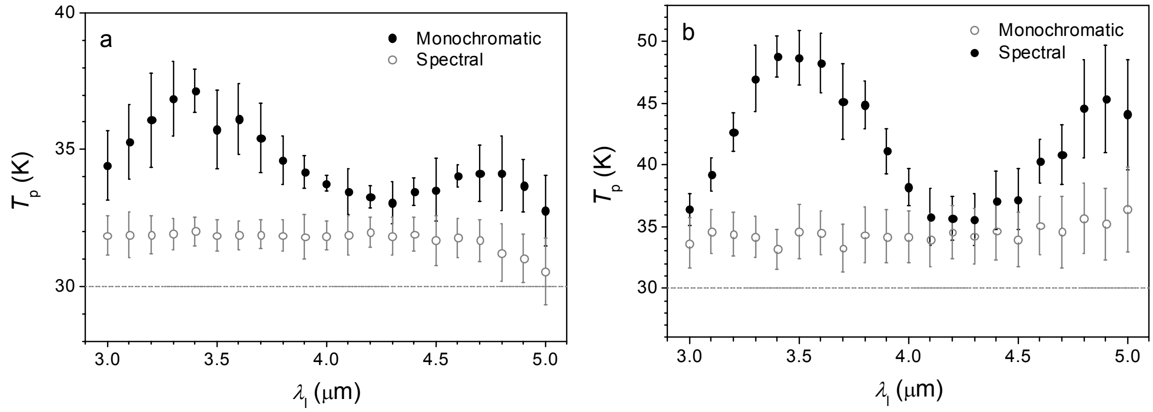

Figure 10.7: Peak temperature T_p and standard deviation (*error bars*) as a function of λ_l for monochromatic (*solid circles*) and spectral reconstruction (*open circles*). Peak temperature T_p is determined from temperature profiles of test objects (a) A and (b) B. Dotted lines indicate the actual object amplitude ($\Delta T_0 = 30$ K).

Statistical analysis of reconstructed images of test object AC, featuring two lobes are presented in Fig. 10.8 for spectral bands with $\lambda_l = 3.0$, 4.3, and 5.0 μm. Monochromatic reconstruction results in temperature profiles with a very narrow and high first peak (AC1), while the second peak (AC2) is broadened as compared to the actual object (*dashed line*). In comparison, spectral reconstruction (*right-bottom*) yields lower and broader first peaks, and higher and narrower second peaks as compared to the results for monochromatic reconstruction. Because of decreased SNR, spectral narrowing compromises the stability of the images reconstructed with either reconstruction approach.

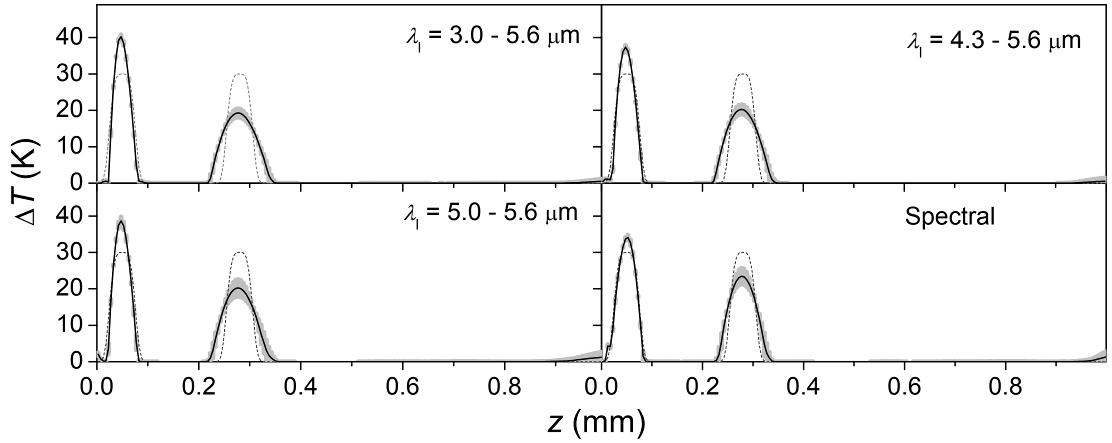

Figure 10.8: Average temperature profiles (*black lines*) and standard deviations (*light-gray bars*) reconstructed from 30 simulated PPTR signals with different noise realizations. Images of test object AC are reconstructed from PPTR signals with spectral bands of λ = 3.0–5.6 μm, 4.3–5.6 μm, and 5.0–5.6 μm using monochromatic reconstruction (*see labels*). Temperature profile for λ = 3.0–5.6 μm is obtained also using spectral reconstruction (*right-bottom*). The actual test objects are plotted for comparison (*dashed line*).

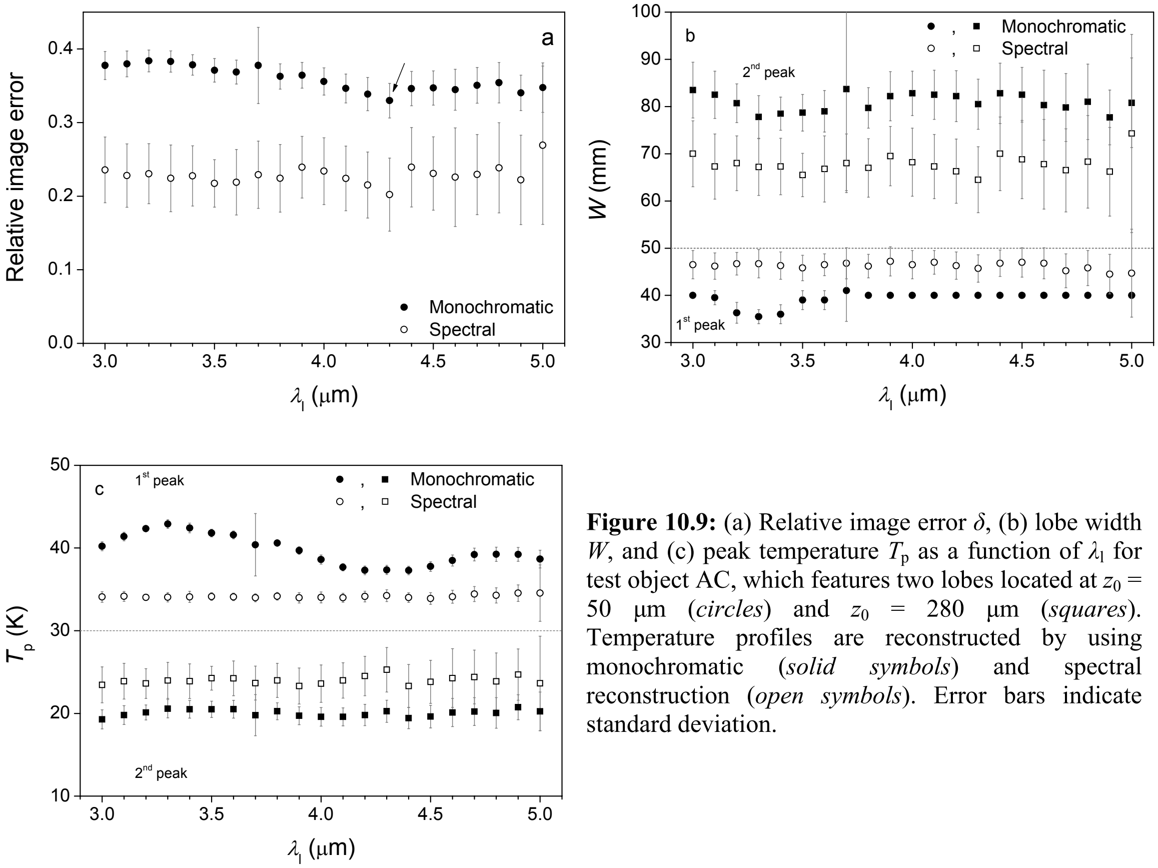

Figure 10.9: (a) Relative image error δ, (b) lobe width W, and (c) peak temperature T_p as a function of λ_l for test object AC, which features two lobes located at z_0 = 50 μm (*circles*) and z_0 = 280 μm (*squares*). Temperature profiles are reconstructed by using monochromatic (*solid symbols*) and spectral reconstruction (*open symbols*). Error bars indicate standard deviation.

Figure 10.9 presents image parameters δ, W, and T_p, determined from images of object AC. When monochromatic reconstruction is used, the minimal relative image error is obtained at λ_l = 4.3 μm (δ = 0.33 ± 0.02) (Fig. 10.9a, *solid circles*). With λ_l decreased below λ_l = 4.2 μm image error increases due to the monochromatic approximation deficiency.

For monochromatic reconstruction (Fig. 10.9b, *solid symbols*), the optimal widths for the first peak are obtained at $\lambda_l = 3.0$ µm and $\lambda_l = 3.8$–5.0 µm ($W = 40$ µm), while the spectral bands between yield even narrower peaks. The optimal widths for the second peak, obtained at $\lambda_l = 3.3$ µm and $\lambda_l = 4.9$ µm, is almost 2-times larger ($W = 78$ µm), than the actual width. But, spectral reconstruction (Fig. 10.9b) yields wider first peaks ($W \approx 46$ µm) and narrower second peaks ($W \approx 68$ µm) than monochromatic reconstruction.

Analogous results are also obtained for peak temperature T_p. Monochromatic reconstruction (Fig. 10.9c, *solid symbols*) results in markedly higher than optimal T_p of the first peak ($T_p = 35 \pm 6$ K at $\lambda_l = 4.3$ µm), and lower than optimal T_p of the second peak ($T_p = 18 \pm 5$ K at $\lambda_l = 4.3$ µm). Peak temperature of the first peak reconstructed by using spectral reconstruction is closer to optimal, average value is $T_p = 33 \pm 5$ K, while the second peak presents peak temperature similar to results for monochromatic reconstruction. In general, all spectral dependencies are hidden by large standard deviation.

Considering the above results for object AC we conclude that spectral reconstruction performs significantly better than monochromatic reconstruction for more complex temperature profiles.

Table 10.1 lists image widths W for all test objects and spectral bands with $\lambda_l = 3.0$, 4.3, and 5.0 µm.

Table 10.1: Temperature peak widths W for test objects A–C and spectral bands with $\lambda_l = 3.0$, 4.3, and 5.0 µm for monochromatic reconstruction. The last column shows widths for spectral reconstruction and $\lambda = 3.0$–5.6 µm. The object width is $W_0 = 50$ µm.

Object	$\lambda_l = 3.0$ µm (µm)	$\lambda_l = 4.3$ µm (µm)	$\lambda_l = 5.0$ µm (µm)	Spectral (µm)
A	45 ± 5	50 ± 0	49 ± 2	50 ± 0
B	53 ± 5	52 ± 3	59 ± 3	52 ± 3
C	61 ± 7	56 ± 8	50 ± 9	54 ± 6
D	87 ± 15	83 ± 11	71 ± 13	75 ± 14
E	177 ± 94	215±130	342±120	185±116
AC – 1st	40 ± 0	40 ± 0	40 ± 0	47 ± 3
AC – 2nd	84 ± 6	81 ± 5	81 ± 10	70 ± 7

Overiteration

To find which reconstruction approach and spectral acquisition bands are less sensitive to overiteration, we also obtained overiterated temperature profiles. Since test objects with larger z_0 (objects C–D) are not markedly deteriorated by non-optimal regularization, we present overiterated reconstruction results of test objects A and B only (Fig. 10.4).

For spectral bands with $\lambda_l = 3.0$ and 5.0 µm, monochromatic reconstruction (Fig. 10.10a, *upper three rows*) results in temperature profiles, which are markedly higher and narrower as compared to the actual object (*dashed line*). But, for the spectral band with $\lambda_l = 4.3$ µm similar results as with optimal regularization are obtained (Fig. 10.4a). In contrast, spectral reconstruction yields results equal to those obtained by optimal regularization (Fig. 10.4, *bottom*). Similar trends, but less prominent, can be observed for object B (Fig. 10.10b).

Figure 10.11 presents relative image error δ for test objects A and B and both reconstruction approaches when overiteration is present. One can recognize a prominent minimum of image error ($\delta = 0.10 \pm 0.01$) at $\lambda_l = 4.4$ µm for monochromatic reconstruction of object A (Fig. 10.11a, *solid circles*). However, acceptably low image errors ($\delta \leq 0.13$) similar to optimal regularization are obtained for spectral bands with $\lambda_l = 4.0$–4.5 µm. Image error is $\delta \approx 0.08$ and standard deviation $\sigma_\delta \approx 0.02$ for spectral bands with $\lambda_l = 3.0$–4.5 µm (Fig. 10.11a, *open circles*), when spectral reconstruction is applied to PPTR signals of test object A. We find similar trends for object B. The minimum of $\delta = 0.15 \pm 0.06$ is obtained at $\lambda_l = 4.3$ μm. However, image error less than 0.17 is obtained for $\lambda_l = 4.1$–4.3 μm, when monochromatic regularization is used (Fig. 10.11b, *solid circles*). For spectral reconstruction (Fig. 10.11b, *open circles*) the image error is roughly constant ($\delta \approx 0.11$ and $\sigma_\delta \approx 0.05$) for $\lambda_l = 3.0$–4.5 μm.

In general, the standard deviation σ_δ progressively increases with spectral band narrowing for both reconstruction approaches and both test objects. Image errors δ obtained for spectral reconstruction are on average similar to those obtained with optimal reconstruction, while δ for monochromatic reconstruction are larger than δ obtained with optimal reconstruction.

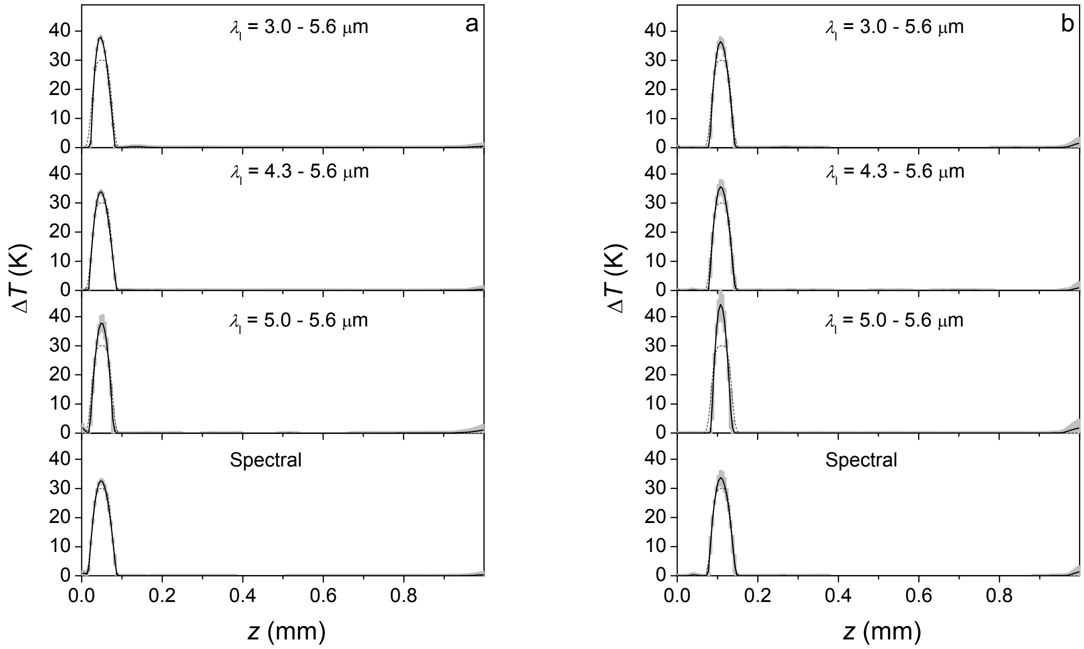

Figure 10.10: Average of overiterated reconstruction results (*black lines*) and standard deviations (*light-gray spots*) reconstructed from 30 simulated PPTR signals with different noise realizations. Images of test objects (a) A and (b) B are reconstructed from PPTR signals with spectral bands of λ = 3.0–5.6 μm (*left*), 4.3–5.6 μm (*center*), and 5.0–5.6 μm (*right*) using monochromatic reconstruction (*see labels*). Images are reconstructed using also spectral reconstruction from PPTR signal with λ = 3.0–5.6 μm. The actual test objects (*dshed line*) are plotted for comparison.

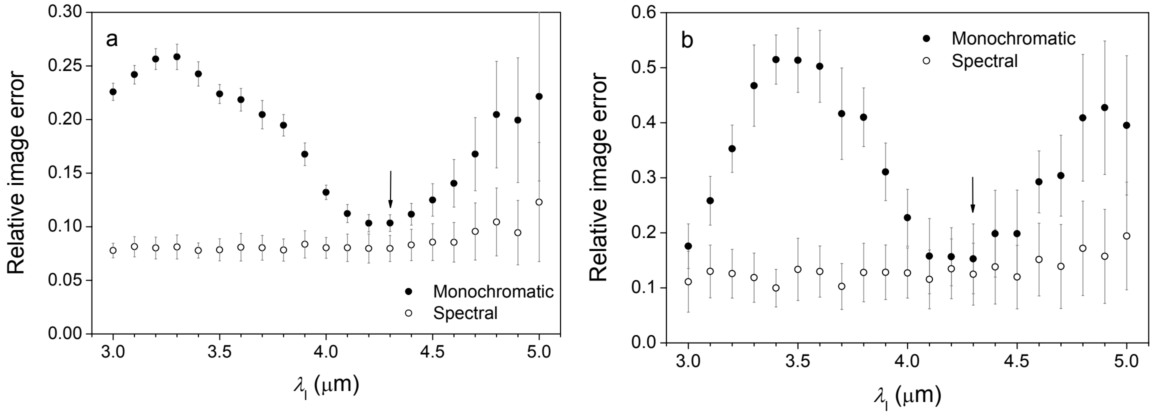

Figure 10.11: Relative image error δ and standard deviation σ_δ (*bars*) as a function of λ_l for monochromatic (*solid circles*) and spectral reconstruction (*open circles*). Image error δ is determined from overiterated temperature profiles of test objects (a) A and (b) B. Arrows indicate optimal λ_l.

Figure 10.12 shows the effect of overiteration on widths W determined from images of test objects A and B. For monochromatic reconstruction and object A (Fig. 10.12a, *solid circles*), W are exceedingly small ($W \approx 40$ µm), except for $\lambda_l = 4.2$ and 4.3 µm ($W = 49 \pm 2$ µm). But, W equals the actual width for $\lambda_l = 3.0$–4.3 µm, and decreases at $\lambda_l > 4.3$ µm, when spectral reconstruction is used (Fig. 10.12a, *open circles*). For object B (Fig. 10.12b), widths of images reconstructed by using spectral reconstruction ($W \approx 47 \pm 4$ µm at $\lambda_l = 3.0$–4.5 µm) are in general close to the actual width, but for monochromatic reconstruction acceptable widths ($W \approx 44 \pm 4$ µm) are obtained only for $\lambda_l = 4.1$–4.3 µm.

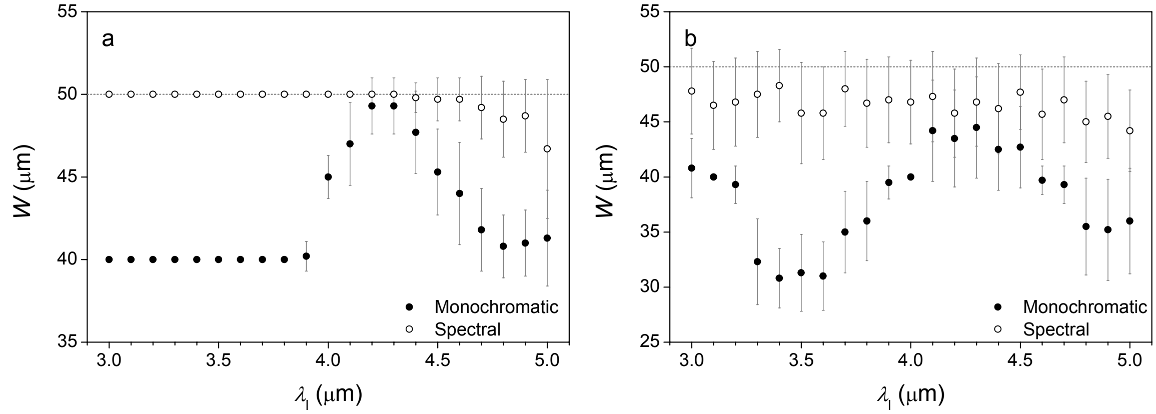

Figure 10.12: Image width W and standard deviation (*error bars*) as a function of λ_l for monochromatic (*solid circles*) and spectral reconstruction (*open circles*). Widths W are determined from overiterated temperature profiles of test objects (a) A and (b) B.

Considering the above results, we conclude that temperature profiles obtained using the monochromatic reconstruction are markedly deteriorated in case of overiteration. But, when appropriate spectral filtering is involved ($\lambda_l \approx 4.0$–4.5 µm), the error due to overiteration is smaller. Spectral reconstruction results in temperature profiles similar to those obtained with optimal regularization for all spectral bands.

10.2 Experiment

10.2.1 Materials and methods

Gelatin tissue phantoms

Our test samples are composed of a ~2 mm thick gelatin gel substrate, absorbing foil and one superficial gel layer of varying thickness (chapter 8). The subsurface depths of the absorbing layers were approximately 50, 110, 280, 430, and 640 µm, respectively, which corresponds to test objects A–E involved in the numerical simulation.

Experimental setup

For each PPTR measurement, the sample was irradiated with a single 1 ms 532 nm pulse from a KTP Nd:YAG laser. The radiant exposures (H) near the center of a 7 mm diameter laser spot were ~ 3.0, 5.0 and 7.8 J/cm^2. Radiation emitted from the center of the irradiated area was collected on our InSb detector (chapter 3). The acquisition rate was 50,000 s^{-1}, and the acquisition time was set to 1 s after the laser pulse.

Radiometric signals were obtained from 3 different sites on each sample, separated by a few millimeters to prevent thermal interference between successive measurements. On each test site, one of three radiant exposures and the entire spectral band of the IR detector ($\lambda = 3.0$–5.6 µm) was used. Finally, the PPTR signals $\boldsymbol{S}$ were obtained by averaging data from 50 subsequent calibrated signals, thus numerically reducing the acquisition rate 1000 s^{-1}, and subtracting the baseline value.

Reconstruction of temperature profiles

Similar to the numerical simulation, initial temperature profiles $\boldsymbol{T}$ were reconstructed using the monochromatic kernel matrix $\boldsymbol{\kappa}$ and the spectrally composite kernel matrix $\boldsymbol{K}$, both computed for the entire spectral acquisition band (λ = 3.0–5.6 μm). The initial temperature profiles were reconstructed using the projected υ-method, and the result consisted of 200 temperature values over a depth range of 1.0 mm.

10.2.2 Experimental results

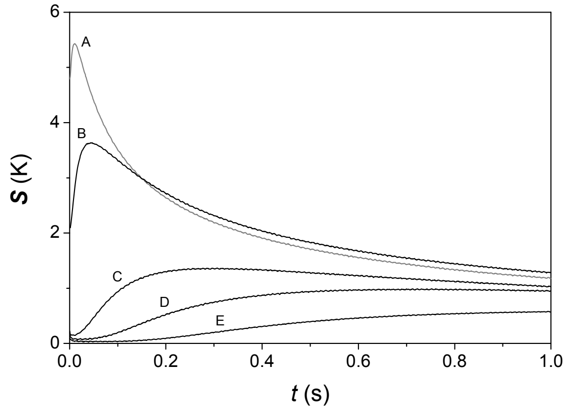

Figure 10.13: PPTR signals acquired from collagen gel samples A–E using the entire spectral band (λ = 3.0–5.6 μm) and H = 3.0 J/cm^2.

Figure 10.13 presents PPTR signals acquired from samples A–E using the full-spectrum acquisition. SNR of measured PPTR signals are summarized in Table 10.2. SNR decreases with depth of absorbing layer Z, and increases with radiant exposure H.

Table 10.2: Signal-to-noise ratios (SNR) for PPTR signals obtained from five collagen gel samples (A–E) using the full-spectrum acquisition (λ = 3.0–5.6 μm) and three radiant exposures.

Sample	H = 3.0 J/cm^2	H = 5.0 J/cm^2	H = 7.8 J/cm^2
A	695	1127	1852
B	655	1008	1260
C	354	597	873
D	249	469	665
E	119	189	287

Figure 10.14 shows images of samples A–E reconstructed by using monochromatic (*solid lines*) and spectral reconstruction (*dashed lines*) for λ = 3.0–5.6 μm. On average, spectral reconstruction does not perform markedly better than monochromatic reconstruction. The reconstruction results for the same sample but different radiant exposures (H) are qualitatively similar.

Since W does not significantly depend on radiant exposure for the same test object and reconstruction approach (Fig. 10.14), we can combine three values into average width W and corresponding standard deviation (Fig. 10.15). For monochromatic reconstruction, the average widths for objects A–E are W = 27 ± 3, 40 ± 0, 47 ± 3, 70 ± 5, and 112 ± 6 μm, respectively. For spectral reconstruction, the average widths for objects A–E are W = 28 ± 6, 38 ± 4, 45 ± 5, 67 ± 10, and 107 ± 6 μm, respectively. Thus, spectral reconstruction yields better results for all samples, except sample A.

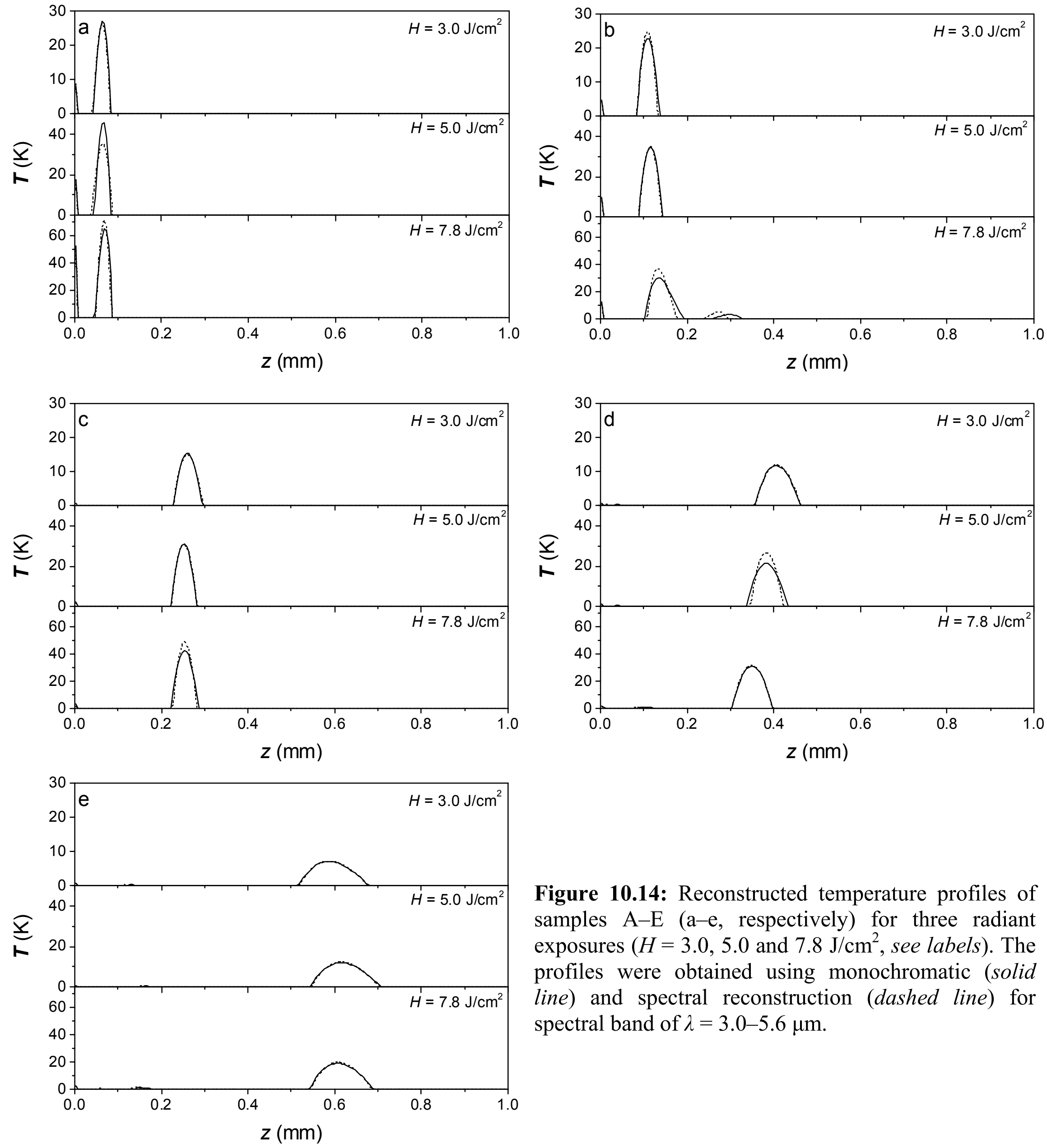

Figure 10.14: Reconstructed temperature profiles of samples A–E (a–e, respectively) for three radiant exposures (H = 3.0, 5.0 and 7.8 J/cm^2, *see labels*). The profiles were obtained using monochromatic (*solid line*) and spectral reconstruction (*dashed line*) for spectral band of λ = 3.0–5.6 µm.

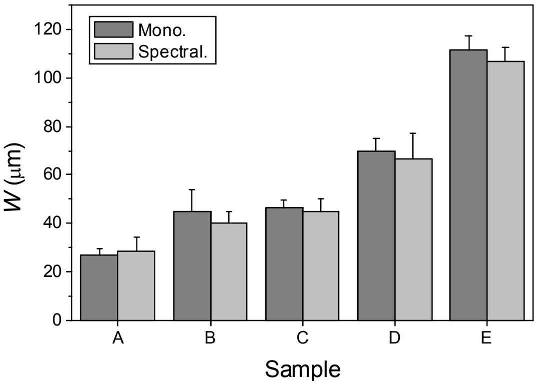

Figure 10.15: Average widths W of temperature lobes in reconstructed images of samples A–E for monochromatic (*gray bars*) and spectral reconstruction (*light-gray bars*). Error bars indicate standard deviation.

10.3 Discussion

The numerical simulation for test objects A, B and C result in the image errors δ, which have distinct minimums at λ_l = 4.3–4.4 μm, when optimal regularization is applied. But, reasonably low δ are obtained also at λ_l = 4.0–4.5 μm for objects A, B and AC. In contrast, the effect of spectral filtering is less apparent for test objects C–E, featuring deep temperature peaks, since all trends are concealed by the large standard deviations σ_δ. When images of test objects A and B are overiterated, the benefit of spectral filtering is even more obvious (Figs. 10.10 and 10.11). The spectral bands in-between (λ_l = 4.0–4.5 μm) provide reconstruction results with reasonably small image errors for both test objects in case of overiteration. Thus, for monochromatic approximation applied to PPTR signals of shallow and more complex structures in collagen samples appropriate spectral filtering reduces image error.

The widths *W* of temperature profiles reconstructed using monochromatic approximation are optimal at λ_l = 4.0–4.4 μm and at λ_l = 4.0–4.5 μm for test objects A and B, respectively. The widths are equal or almost equal to the actual width. In contrast, for deeper objects (C–E) determined widths increase with increasing depth of temperature peak z_0. This broadening effect due to increasing z_0 is well known (chapter 11). But, we also observe broadening of W with broadening of acquisition spectral band for objects B–E (Table 10.1), but the trend is less obvious than for agar gel (chapter 9), since it is almost completely concealed by the large standard deviations σ_W.

In general, spectral reconstruction results in images with smaller image errors than monochromatic reconstruction. However, for spectral bands with λ_l = 4.0–4.5 μm and objects A–E both approaches yield similar results. Yet, spectral reconstruction performs significantly better than monochromatic reconstruction for test objects AC. We obtain 1.5-times smaller δ using spectral approach. And when overiteration is present, images obtained by spectral approach are significantly more stable and accurate.

The findings of the numerical simulation are supported by our experimental results, where the reconstruction results obtained by the optimally regularized monochromatic approximation and spectral reconstruction are similar, which agrees with the results of the numerical simulation for test objects A–E.

10.4 Conclusions

In PPTR temperature profiling of collagen tissue phantoms, spectral filtering reduces the reconstruction error δ and improves accuracy of temperature peak width *W*, when the monochromatic reconstruction is used. For the simulated objects and PPTR system, results of numerical simulations suggest an optimal spectral band with λ_l = 4.0–4.5 μm. Spectral reconstruction results in more accurate and stable reconstructions than monochromatic reconstruction, especially for more complex and shallower absorbing structures. Therefore, use of spectrally composite matrix is preferred when the IR spectrum of the sample and responsivity of IR detector are known.

Chapter 11

Accuracy of temperature profiling

Since PPTR temperature profiling is used for determination of temperature profiles in biological tissues, the question about accuracy of determined temperature profiles arises. The accuracy is limited by measurement noise, efficiency of reconstruction algorithms, and also by the involved physical processes (i.e., ill-posed problem). It is known that depths of absorbing structures are determined fairly well,[6] but PPTR temperature profiling fails to predict accurate temperatures due to the broadening and attenuation effects, especially at greater depths,[9,10]

In this chapter we study the accuracy of temperature profiles obtained using our PPTR system. First, we perform experiments on agar tissue phantoms involving one very thin absorbing layer located at different depths. Second, we perform a numerical simulation to support our experimental results. Finally, we compare the obtained limitations of our PPTR system to those reported in earlier PPTR studies.[6,9,10]

11.1 Experiments on agar tissue phantoms

11.1.1 Materials and methods

Agar tissue phantoms

We prepared agar tissue phantoms composed of one superficial agar gel layer of varying thickness, one thin absorbing layer and a ~2 mm thick gel substrate. Absorbing layers were made of absorbing foil. Seven tissue phantoms (A–G) evaluated here had the subsurface depths of the absorbing layers approximately 40, 130, 270, 420, 600, 750 and 900 µm. Three tissue phantoms (B1–D1) were prepared for PPTR and NMR measurement. The depths of their absorbing layers were ~180, 300 and 480 µm. Details about agar gel tissue phantom preparation are presented in Chapter 8.

Pulsed photothermal profiling

For each PPTR measurement, the sample was irradiated with a single 1 ms long 532 nm pulse from a KTP/Nd:YAG laser. Three different radiant exposures were used with samples A–G. The radiant exposures (H) near the center of a 7 mm diameter laser spot were $H \approx 3.0$, 5.0 and 7.8 J/cm^2. However, only $H = 3.0$ J/cm^2 was used with samples B1–D1 to avoid damage due to laser irradiation. IR radiation emitted from the center of the irradiated area was collected on the InSb detector. Radiometric signals were obtained from 3 different sites on each sample, separated by a few millimeters to prevent thermal interference between successive measurements. On each site one of three radiant exposures and the entire spectral band of the IR detector (λ = 3.0–5.6 µm) was used. The acquisition rate was 50,000 s^{-1} and the acquisition time was set to 1.5 s after the laser pulse. The PPTR signals $\boldsymbol{S}$ were obtained by averaging 50 subsequent calibrated data points, thus computationally reducing the acquisition rate from 50,000 s^{-1} to 1000 s^{-1}, and subtracting the baseline value.

The initial temperature profiles $\boldsymbol{T}$ were reconstructed using the spectrally composite kernel matrix $\boldsymbol{K}$ (6.1). We used the measured IR absorption spectrum $\mu(\lambda)$ of agar tissue phantom (Fig. 8.3), spectral responsivity of the InSb detector (Fig. 3.3) and thermal parameters D = 0.143 mm^2/s and h = 0.02 mm^{-1}. The projected υ-method was used to reconstruct temperature profiles $\boldsymbol{T}$ consisting of 300 temperature values over a depth range of 1.5 mm.

Optical microscopy and micro magnetic resonance imaging (micro-MRI)

The depth of the absorbing layer in samples A–G was determined after each PPTR measurement by means of optical microscopy. We used magnification 40×. We focused the microscope on the surface of the sample and then on the boundary between the surface gel layer and the foil. At the same time we measured optical path between the surface and the boundary using calibrated fine focus. We corrected measured optical path using the index of refraction of water (1.33), thus obtaining the absorbing layer depth Z. The accuracy of Z determined by microscope focusing was approximately ±30 µm, which was found as the minimal shift of microscope focus yielding blurred image of the boundary. Z was determined at 4 locations per sample.

After PPTR measurement, cross-sectional images of samples B1–D1 were acquired using a micro-MRI system (TecMag, Bruker, Oxford, B = 2.35 T). 3D spin echo imaging technique was used with echo time/repetition time (TE/TR) = 7/1000 resulting in T1-weighted image. Field of view was 16×2×8 mm with 31 µm isotropic resolution. The image was stored in JPEG format (512 × 128 pixels). Distance from the sample surface to the absorbing layer Z was determined from the image at 10 positions for each sample.

11.1.2 Experimental results

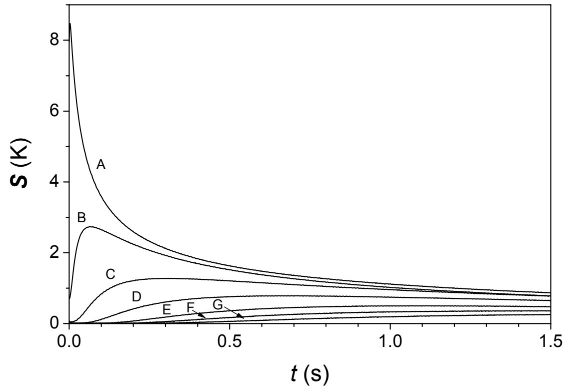

Figure 11.1: PPTR signals acquired from samples A–G (*see labels*) with radiant exposure H = 3.0 J/cm^2.

PPTR signals acquired from samples A–G at H = 3.0 J/cm^2 are presented in Figure 11.1. Noise-equivalent temperature rise, determined as standard deviation of radiometric signals before the laser exposure, equals $NE\Delta T$ = 2.2 mK. Average SNR as a function of the absorbing layer depth Z are presented in Figure 11.2 for all measured signals and radiant exposures. SNR decreases roughly exponentially with increasing Z.

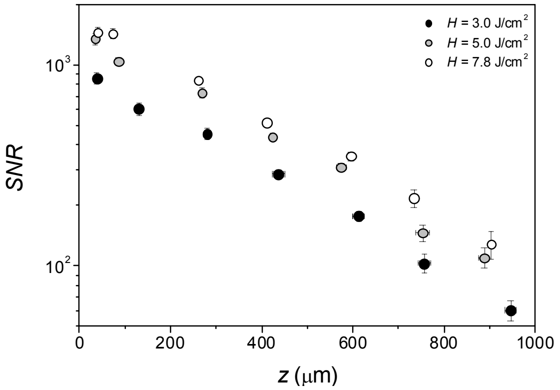

Figure 11.2: *SNR* as a function of the absorbing layer depth Z for H = 3.0 J/cm^2 (*black circles*), 5.0 J/cm^2 (*gray circles*) and 7.8 J/cm^2 (*open circles*). Error bars indicate standard deviation of Z and SNR.

Figure 11.3 presents statistical analysis of the reconstruction results for the three radiant exposures and samples A–G (*see labels*). Solid lines connect the average temperatures and light-gray bars indicate standard deviations. As expected, temperature profiles broaden with increasing depth of the peak temperature Z for all H. The reconstructed images of all samples are evidently broadened for $H = 3.0$ J/cm^2 as compared to $H = 5.0$ and 7.8 J/cm^2. Moreover, images of samples A–D feature largest standard deviations for $H = 3.0$ J/cm^2, and smallest for $H = 7.8$ J/cm^2. Thus, the broadening effect is smaller and the reconstruction is more robust when larger radiant exposures are used. We observe surface artifacts in images of sample A for $H = 5.0$ J/cm^2 and of samples A–C for $H = 7.8$ J/cm^2. Because the artifacts are present only in images of shallow samples (Z = 50–300 μm) and for large radiant exposures, we believe that the artifacts are consequence of the linearization error (chapter 5).

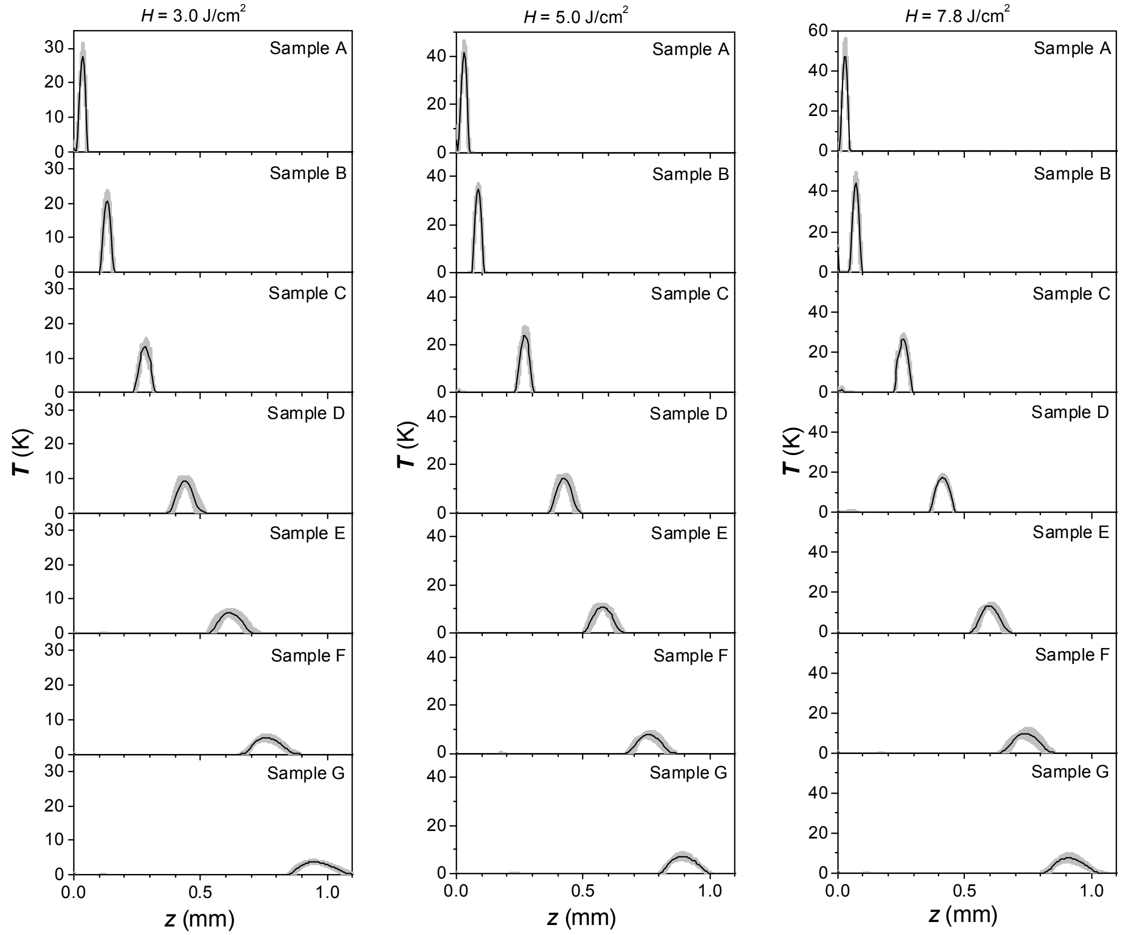

Figure 11.3: Average temperature profiles (*solid lines*) and standard deviations (*light-gray bars*) reconstructed from 10 PPTR signals acquired from samples A–G using radiant exposures $H = 3.0$ J/cm^2 (*left*), 5.0 J/cm^2 (*center*) and 7.8 J/cm^2 (*left*).

Peak temperature depth

Figure 11.4 presents peak temperature depths Z determined from PPTR reconstruction results for the three radiant exposures and absorbing layer depths determined by optical microscopy. Absorbing layer depths determined by PPTR temperature profiling, on average, match the results obtained by the microscope within respective uncertainties. Possible origin of the observed discrepancy is shrinking of the surface agar layer upon evaporation of water during microscopy, which can explain the discrepancy present for samples E–G. Apparently, the match between Z determined by PPTR and microscopy does not improve with increasing H.

We also compared absorbing layer depths obtained by PPTR profiling with those found by micro-MRI for samples B1–D1. Figure 11.5 presents reconstructed temperature profiles and micro-MRI images of samples B1–D1. Micro-MRI image of samples B1–D1 clearly show samples surfaces (*upper arrow*) and the absorbing layers (*lower arrow*). Peak temperatures in Fig. 11.5a are higher as compared to peak temperatures in Fig. 8.3, because a thicker absorbing foil (~30 μm) was used in preparation of samples B1–D1 to improve contrast in micro-MRI images, and consequentially more light was absorbed in absorbing layers.

Peak temperature depths Z determined from reconstruction results (Fig.11.5a) and absorbing layer depths determined from micro-MRI images (Fig. 11.5b) agree very well (Fig. 11.6). The largest discrepancy (10 μm) is found in sample D1, and is 3 times smaller than the micro-MRI resolution (Δz = 30 μm), which limits the accuracy of the determined absorbing layer depth. The above results indicate that the accuracy of absorbing layer depths found by PPTR temperature profiling is good, and is not significantly deteriorated by SNR or the absorbing structure depth.

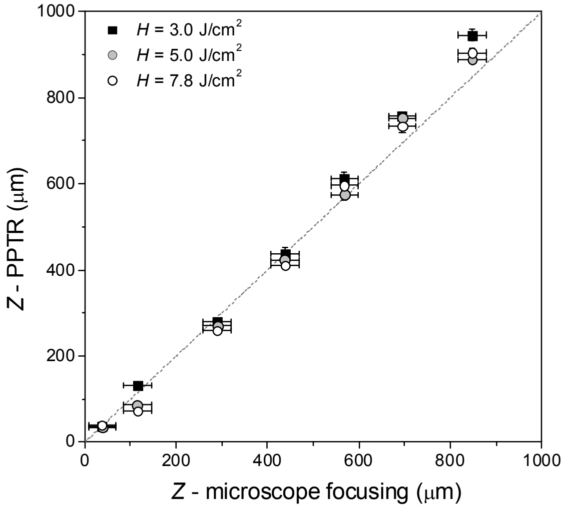

Figure 11.4: The absorbing layer depth Z from the PPTR reconstruction results and the microscope focusing for samples A–G and radiant exposures H = 3.0 J/cm^2 (*black squares*), 5.0 J/cm^2 (*gray circles*) and 7.8 J/cm^2 (*open circles*). The dashed line represents the case of Z-microscope = Z-PPTR.

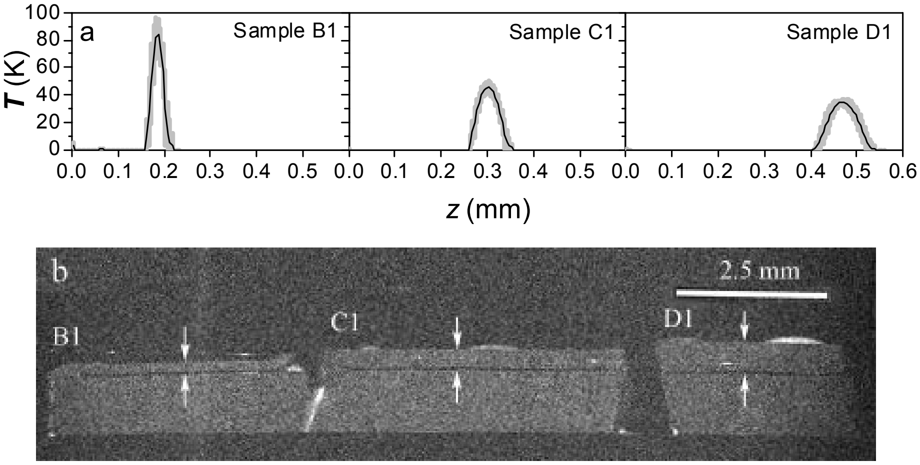

Figure 11.5: (a) Average temperature profiles (*solid lines*) and standard deviations (*error bars*) reconstructed from 10 PPTR signals acquired from samples B1–D1 using radiant exposures H = 3.0 J/cm^2. (b) A micro-MRI image of samples B1 (*left*), C1 (*center*) and D1 (*right*). The *upper arrow* indicates the sample surface and the *lower* one indicates the absorbing layer.

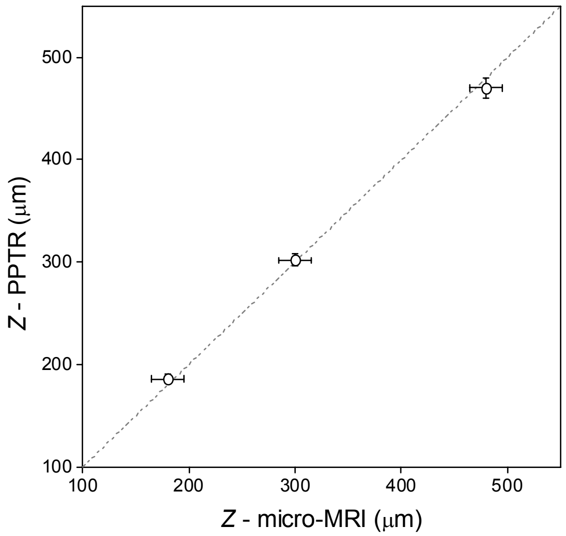

Figure 11.6: The absorbing layer depth Z from the PPTR reconstruction results and the micro-MRI for samples B1–D1 (*open circles*). The dashed line represents the case of Z-micro-MRI = Z-PPTR.

Temperature peak width

Temperature peak widths W as a function of peak temperature depth Z are presented in Figure 11.7 for samples A–G and radiant exposures H = 3.0 J/cm^2 (*left*), 5.0 J/cm^2 (*center*) and 7.8 J/cm^2 (*right*). Widths of reconstructed temperature profiles increase almost linearly with Z, except at depths $Z < 300$ μm. For these depths the actual absorbing layer width w_0 prevails over the broadening effect. Determined widths W for H = 3.0 J/cm^2 are on average 19% larger as compared to H = 5.0 J/cm^2, while the differences between widths for H = 5.0 J/cm^2 and H = 7.8 J/cm^2 are not significant. Hence, we conclude that SNR influences significantly the temperature profile widths when SNR is low, while the effect of SNR on W is insignificant when SNR is large (e.g., SNR = 1000).

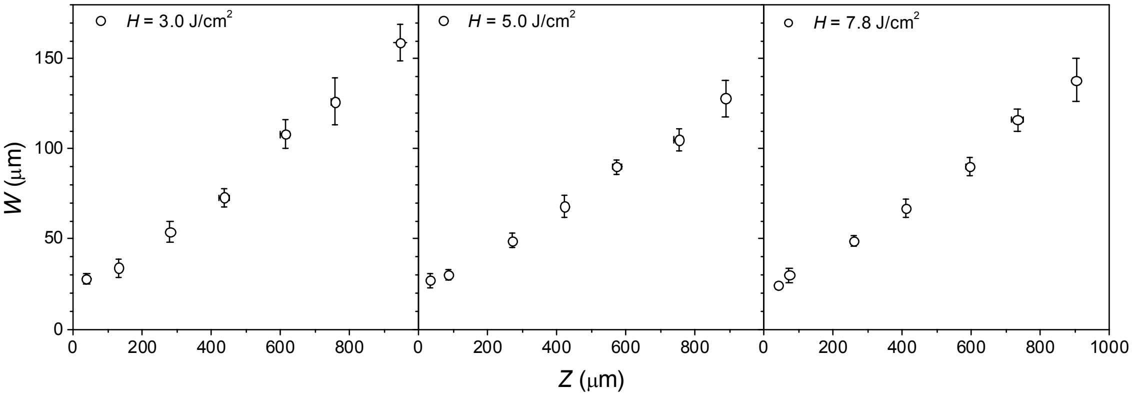

Figure 11.7: The temperature peak width W as a function of the peak temperature depth Z for samples A–G and radiant exposures H = 3.0 J/cm^2 (*left*), 5.0 J/cm^2 (*center*) and 7.8 J/cm^2 (*right*). Bars are standard deviations of W and Z.

11.2 Numerical simulation

Delta functions are frequently used in science and engineering as an input into an unknown system, because the corresponding output specific information about the system. As the input we use a delta function located at depth z_0, the unknown system is a simulated PPTR system and the output is the reconstructed temperature profile. The extracted specific information is the accuracy of determined impulse depth, and broadening and attenuation of reconstructed temperature peaks.

Our initial temperature profile is a delta function (i.e., a planar impulse)

$$T_0\left(z,0\right)=T_0 w\ \delta\left(z-z_0\right) \tag{11.1}$$

where T_0w represents the impulse amplitude. When we substitute delta function (11.1) into expression for the PPTR signal amplitude (2.7), we obtain an expression for PPTR signal of planar impulse

$$\Delta S\left(t\right)=T_0 w\ K\left(z_0,t\right) \tag{11.2}$$

We simulate theoretical signal vectors $\boldsymbol{S}_0$ using (11.2) and the spectrally composite kernel matrix $\boldsymbol{K}$ (6.1) equal to the kernel matrix in previous section. To correlate the numerical simulation with the experimental results we use similar depths of temperature profiles z_0 = 42.5 (object A), 132.5 (object B), 272.5 (object C), 422.5 (object D), 602.5 (object E), 742.5 (object F) and 902.6 μm (object G). The impulse amplitudes are T_0w = 0.15, 0.75, 1.25, 1.95 and 5.00 mmK. Each $\boldsymbol{S}_0$ has 1500 components, representing signal values acquired at a sampling rate of f = 1000 s^{-1} (for a total acquisition time was 1.5 s).

Each theoretical signal is augmented by 30 different realizations of zero mean noise with the noise amplitude $NE\Delta T$ = 2.2 mK, thus resulting in realistic PPTR signals $\boldsymbol{S}$**.** The parameters of 1/f-noise characteristic for our PPTR system are f_c = 15 s^{-1} and α = 1.3 (section 3.5). Each realization of noise is calculated using the noise spectrum $\tilde{n}(f)$ (3.5)

$$n(t_k)=\sum_{i=1}^{N}\tilde{n}(i/\Delta t\,N)\,\cos(2\pi\,t_k\,i/\Delta t\,N+\delta_i) \tag{11.3}$$

where Δt is the sampling interval (1 ms), N number of signal components and $t_k = k\,\Delta t$, where k is an integer between 0 and N–1. δ_i is a random number between –π and π, obtained by function *randn* in Matlab 14. $n(t_k)$ is then normalized so that it has a standard deviation of 1. Finally, the obtained noise vector is multiplied by $NE\Delta T$ and added to theoretical signal $\boldsymbol{S}_0$, yielding a simulated PPTR signal $\boldsymbol{S}$.

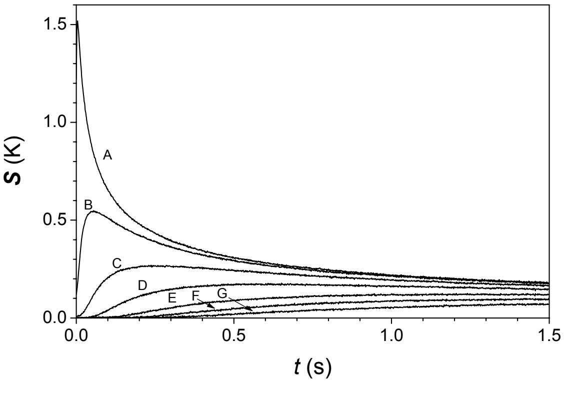

Figure 11.8: Simulated PPTR signals for planar impulses with T_0w = 0.15 mmK for test objects A–G (*see labels*).

Figure 11.8 presents simulated PPTR signals for T_0w = 0.75 (*top*), 1.25 (*center*) and 1.95 mmK (*bottom*). Signal-to-noise ratio (SNR) as a function of z_0 is presented in Figure 11.9 for all simulated PPTR signals. SNR values decrease with increasing z_0 and decreasing T_0w.

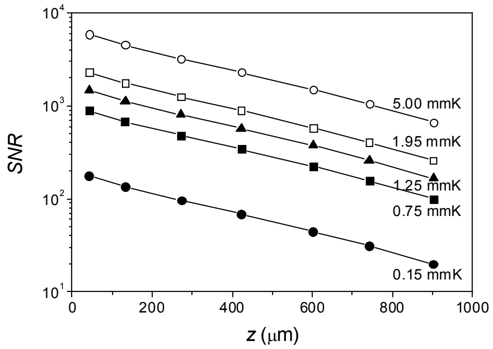

Figure 11.9: *SNR* as a function of impulse depth z_0 for T_0w = 0.15–5.00 mmK (*see labels*).

11.2.1 Numerical results

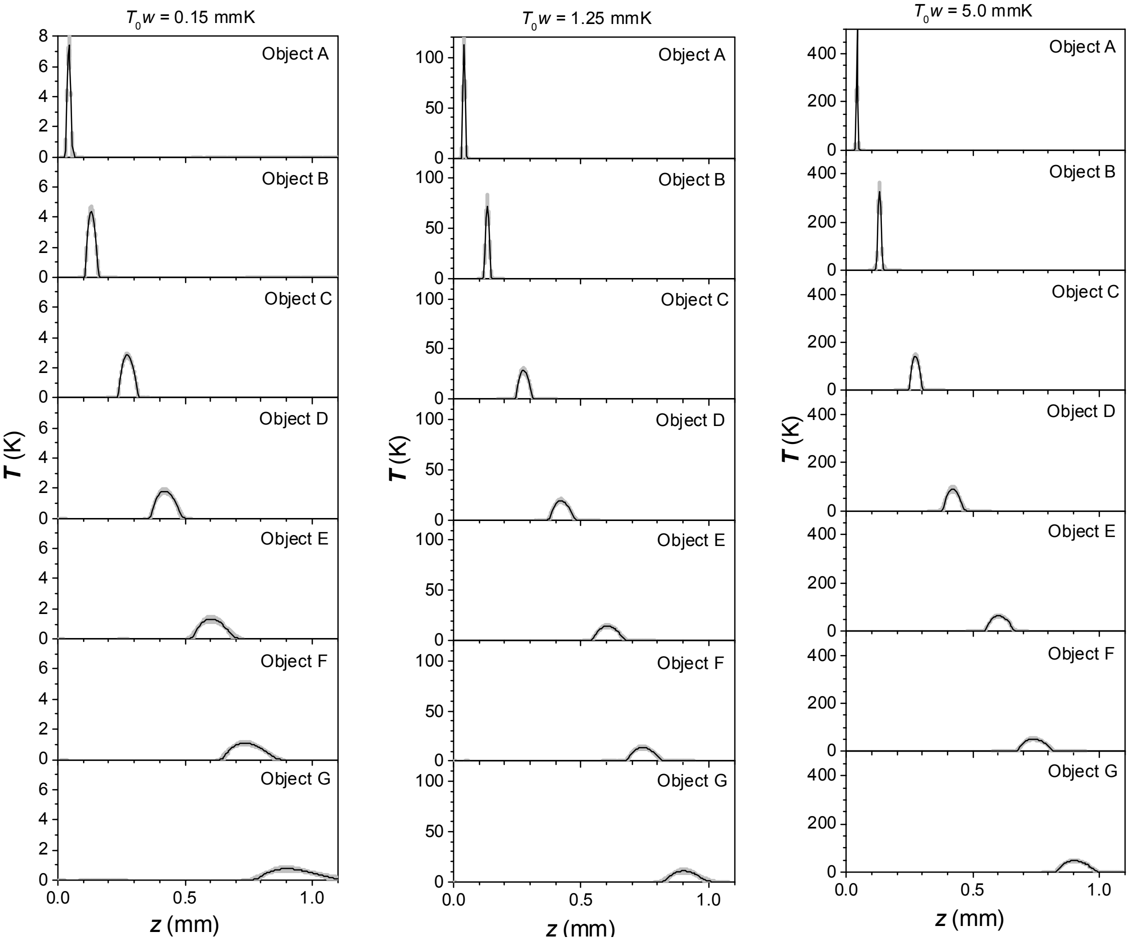

Figure 11.10: Average temperature profiles (*solid lines*) and standard deviations (*error bars*) reconstructed from 30 simulated PPTR signals with different noise realizations. Images of test objects (*see labels*) were reconstructed from PPTR signals with impulse amplitudes T_0w = 0.15 mmK (*left*), 1.25 mmK (*center*) and 5.00 mmK (*left*).

Temperature profiles $\boldsymbol{T}$ of simulated planar impulses are reconstructed from corresponding PPTR signals $\boldsymbol{S}$ using the projected υ-method with automatic regularization. The temperature profile vectors T consisted of 300 temperature values over a depth range of 1.5 mm (discretization step Δz = 5 μm).

Figure 11.10 presents statistical analysis of the reconstruction results for three impulse amplitudes:

T_0w = 0.15 mmK (*left*), 1.25 mmK (*center*) and 5.00 mmK (*left*). Obviously, width of reconstructed temperature profile W decreases with depth z_0. In addition, W increases with decreasing SNR (i.e., T_0w).

Depth Z

Figure 11.11 presents peak temperature depth Z as a function of impulse location z_0 for all impulse energies T_0w. We calculate relative depth error as $\delta_z = (z_0 - Z)/z_0$. For objects A–C (z_0 = 40–300 μm), Z absolutely matches z_0 for all T_0w. For objects D–F, we find ~1% error for T_0w = 0.15 mmK, while δ_z for other T_0w is negligible. Only for the deepest object G, error δ_z = 1–3% occurs for all T_0w. Hence, neither z_0 nor T_0w significantly deteriorate the accuracy of temperature peak location Z.

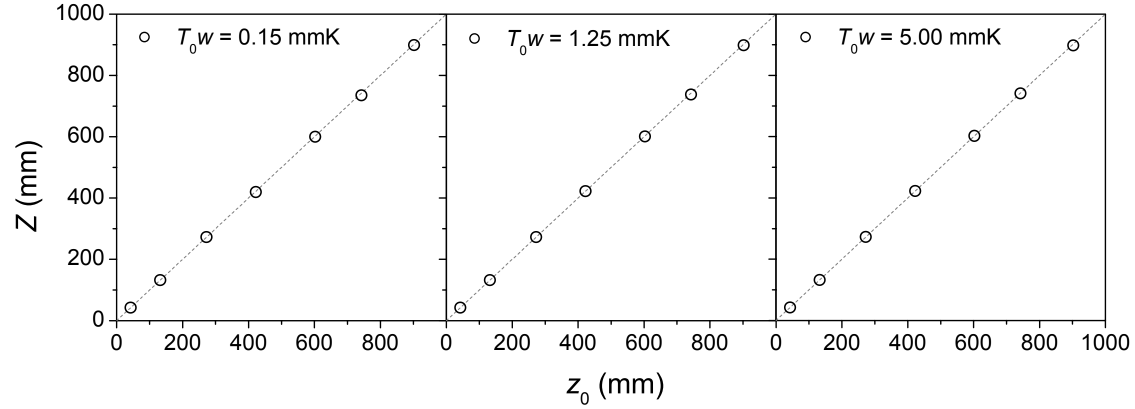

Figure 11.11: Determined peak temperature depth Z (*open circle*) as a function of the actual impulse depth z_0 for three impulse amplitudes (*see legends*). Dashed line illustrates the ideal agreement (i.e., $Z = z_0$).

Broadening and attenuation

Since planar impulses are infinitesimally thin, width W of ideally reconstructed planar impulse would be equal to depth discretization Δz and the corresponding peak temperature equal to $T_0w/\Delta z$. Yet, Figure 11.10 shows, that widths of reconstructed planar impulses are larger than Δz (5 μm).

Figure 11.12a presents widths W of temperature profiles as a function of z_0 for all T_0w. On average, W increases linearly with z_0, while it decreases with T_0w. Figure 11.12b presents W as a function of *SNR* for test objects A–G. For constant z_0, W tends to decrease with increasing SNR.

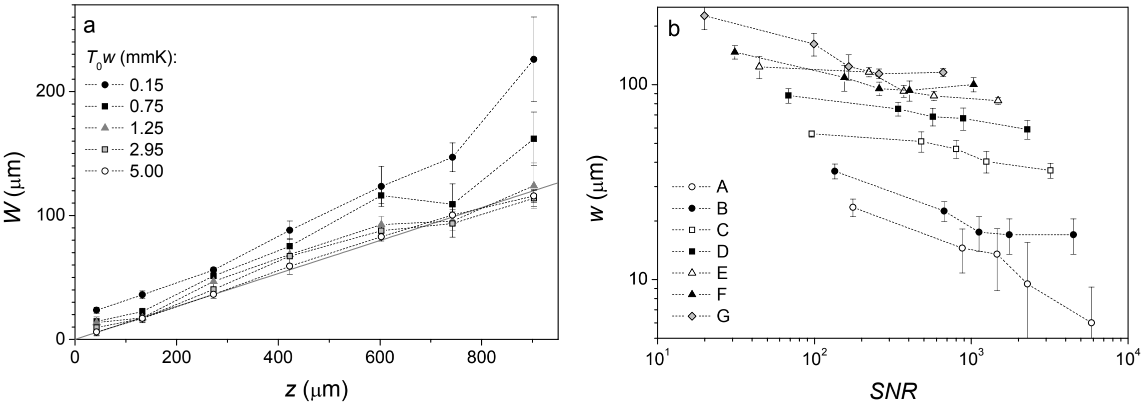

Figure 11.12: (a) Width of reconstructed planar impulse W increases almost linearly with depth z_0 (*see gray line*). (b) W as a function of *SNR* for all impulse amplitudes T_0w (*see labels*). Standard deviations are represented by error bars.

Considering the above observations, we propose the following approximation for the broadening w as a function of z_0 and SNR

$$w(z_0, SNR) = p_1\, z_0 + \frac{p_2}{SNR} \tag{11.4}$$

We fit (11.4) on data in Fig. 11.12b and determine parameters $p_1 z_0$ and p_2 for all z_0 (Figs. 11.13a–b).

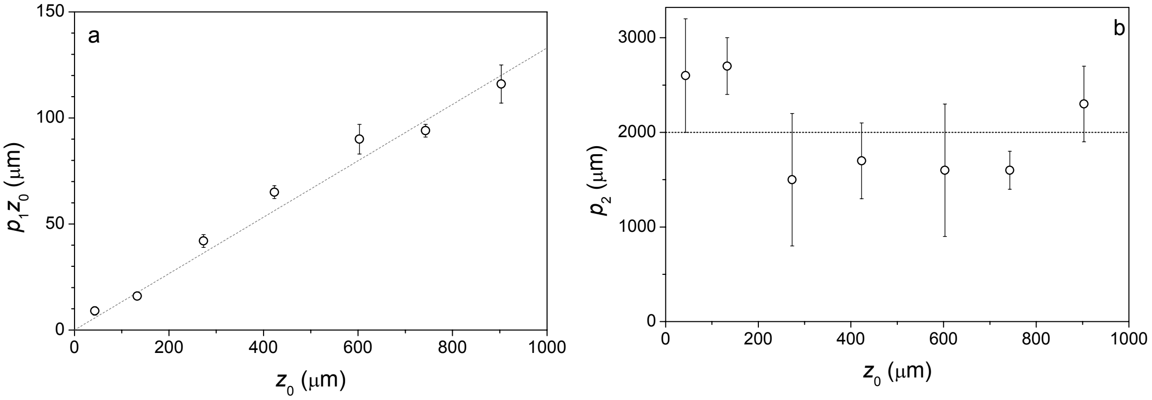

Figure 11.13: Parameters (a) $p_1 z_0$ and (b) p_2 as a function of z_0 obtained by fitting (11.4) on data in Fig. 11.12b. Gray lines present (a) the linear fit and (b) the simple mean of data points.

By fitting data in Fig.8.14a with linear function we obtain $p_1 = 0.133 \pm 0.004$. Furthermore, we determined simple mean and standard deviation from values presented in Fig. 11.13b to obtain the second parameter in (11.4) $p_2 = 2000 \pm 200$ μm. Finally, the approximation for the impulse broadening is

$$w(z_0,\, SNR) = 0.133\, z_0 + \frac{2000\ \mu m}{SNR} \tag{11.5}$$

We estimated the broadening of our experimental temperature profiles $w(z_0, SNR)$ (Fig. 11.14, *dashed line*) using the above approximation (11.5) and experimental depths Z (Fig. 11.4) and SNR values (Fig. 11.2). Experimental widths W of samples A–G, already presented in Fig. 11.7, are included also in Fig. 11.14 (*open circles*).

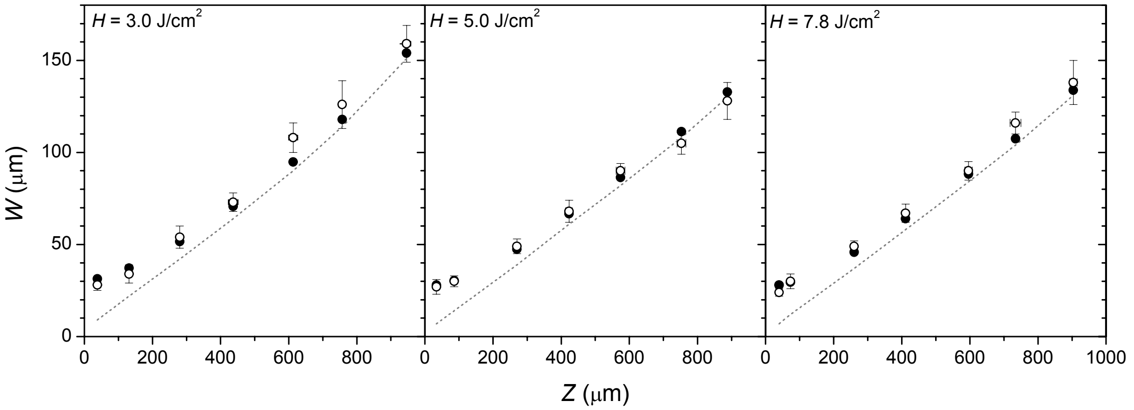

Figure 11.14: Broadening $w(z_0, SNR)$ of a planar impulse (*dashed* line) calculated using (11.5) with experimental depths Z (Fig. 11.4) and SNR values (Fig. 11.2) for radiant exposures $H = 3.0$ J/cm^2 (*left*), 5.0 J/cm^2 (*center*) and 7.8 J/cm^2 (*right*). Estimated total width W of temperature profiles (*black circles*) including the broadening $w(z_0, SNR)$ and the estimated thickness of absorbing layer ($w_0 = 30, 27, 27$ μm for $H = 3.0$, 5.0 and 7.8 J/cm^2, respectively). The actual widths W of samples A–G (*open circles*) are plotted for comparison.

Widths W determined from the experimental temperature profiles for samples A–G deviate from the corresponding broadening $w(z_0, SNR)$, especially for shallow absorbing layers (samples A and B). The absorbing layers are of finite width w_0, which must also be considered in an estimation of reconstructed temperature profile width. We estimate the total width W as $W = (w(z_0, SNR)^2 + w_0^2)^{1/2}$.

We fit this expression with the broadening (11.5) to the experimental widths W to obtain estimations for the absorbing layer width, $w_0 = 30 \pm 9$, 27 ± 2 and 27 ± 6 µm for $H = 3.0$, 5.0 and 7.8 J/cm^2, respectively. Next, we calculate the estimated total width W (Fig. 11.14, *black circles*) using the determined $w(z_0, SNR)$ and w_0. Since the deviation between the estimated W and the experimental W is within the experimental uncertainty, we conclude that (11.5) can be used to estimate the broadening effect in reconstructed temperature profiles.

11.3 Discussion

Milner *et al*,[6] who performed PPTR temperature profiling on layered collagen tissue phantoms with absorption layers located at $z_0 = 70–440$ µm, reported the standard deviation of the difference between Z deduced by PPTR temperature profiling and optical low-coherence reflectometry was 2 µm. Sathyam and Prahl,[9] who presented results of numerical simulation involving planar impulses and experiment, also showed that PPTR temperature profiling is fairly efficient at determining Z. But, the uncertainty in the depth markedly increase with the depth, hence limiting the technique to a depth of 500 µm. In contrast, the results of our study show that we can successfully determine the temperature peak depths Z at least up to 900 µm, while the accuracy of determined Z is not significantly deteriorated by low SNR.

The broadening effect involved in PPTR temperature profiling is well known.[6,7,9] It is a reconstruction artifact, which increases with object depth, thereby significantly limiting resolution of PPTR temperature profiling. Sathyam and Prahl[9] reported that a resolution about equal to the depth could be expected with PPTR temperature profiling. Smithies *et al*[10] presented simulation results, where the broadening of temperature peaks was approximately 25% of peak temperature depths Z, although monochromatic PPTR signals without noise were used. But results of our experiment combined with the numerical results, show that the broadening effect equals to ~15% of Z, although our experimental results are deteriorated by the linearization error (chapter 5) and measurement noise. At lower SNR the additional broadening due to noise in PPTR signals becomes significant (11.5).

The attenuation of peak temperature T_p accompanies the broadening. As illustrated in Figs. 11.3 and 11.10, T_p decreases with depth Z. Therefore PPTR temperature profiling fails to accurately determine temperatures, especially at larger depths. Because the broadening effect and the temperature attenuation are less prominent for larger SNR values, one should reduce noise in PPTR signals to adequately small level.

11.4 Conclusions

PPTR temperature profiling accurately predicts locations of absorbing layers at least up to a depth of 900 µm. Since reconstructed temperature profiles are progressively broadened and attenuated with depth, PPTR temperature profiling fails to accurately determine widths and temperatures of deeper absorbing structures. For agar tissue phantoms, our PPTR system and large SNR the broadening equals to ~13% of peak temperature depth, which is significantly better than the smallest broadening (i.e., ~25% of peak temperature depth) reported in any earlier PPTR study.

Chapter 12

Summary and conclusions

In this concluding chapter, we summarize the main achievements and findings presented in the dissertation, and discuss possible directions for further research.

To solve the ill-posed PPTR inverse problem, we have developed three novel reconstruction algorithms based on the truncated singular value decomposition (TSVD) method, conjugated gradient method (CG), and υ-method, respectively. All algorithms include the non-negativity constraint and automatic regularization, which substantially facilitates the reconstruction process. The optimal regularization approach is also determined for each algorithm. We demonstrate that these algorithms produce substantially more accurate solutions than commercially available general-purpose software. Furthermore, our algorithms result in more accurate temperature profiles than presented in an earlier PPTR study utilizing a dedicated non-negatively constrained reconstruction algorithm. All three presented algorithms generate similar reconstruction results.

An expression for a linearized monochromatic calibrated PPTR signal is used in all reported PPTR studies. However, the linearization error was not systematically evaluated in earlier PPTR studies. We demonstrate that the linearization error can markedly deteriorate the reconstructed temperature profiles when temperature amplitudes larger than ~20 K are involved. Due to the linearization error we can observe in reconstructed temperature profiles superficial artifacts. In general, the linearization error decreases as temperature profile depth and acquisition time increase. We derived an analytical expression for the linearization error, which indicates that linearization error decreases with increasing acquisition wavelength λ and baseline temperature T_b. For the spectrally composite calibrated PPTR signals, we observe also that the linearization error decreases with spectral acquisition band narrowing. Because temperature amplitudes are typically less than ~20 K, the linearization error is small for typical PPTR temperature profiling in human skin, especially for deeper absorbing structures.

In PPTR temperature profiling, broad-band signal acquisition is used almost invariably to increase the signal-to-noise ratio (SNR). But all reported PPTR studies utilized a fixed effective infrared (IR) absorption coefficient value (μ_{eff}) to reduce computational complexity of the reconstruction process. When a non-optimal μ_{eff} is utilized in reconstruction, the resulting temperature profiles are deteriorated. A mere 5% deviation of μ_{eff} from the optimum can increase the relative image error by 33%. We present a novel analytical approach for analytical determination of viable effective IR absorption coefficients to be used in reconstruction of temperature profiles from PPTR signals at any combination of sample spectral properties, radiation detector, and acquisition spectral band. This is particularly important in samples with large spectral variation $\mu(\lambda)$ in mid-IR, such as most biological tissues, where previously used analytical estimates are not sufficiently accurate. The analytical approach is supported by numerical simulation. The numerical results show also that the reduction of spectral acquisition band significantly improves the validity of quasi-monochromatic approximation.

We analyzed the effect of sampling frequency on the accuracy of reconstruction results. Clearly, broadened and attenuated temperature profiles are obtained by undersampling due to insufficient information in PPTR signals. On the other hand, SNR of PPTR signals is severely reduced when large sampling frequencies are used, and again deteriorated temperature profiles are obtained. Our numerical results show that higher sampling rates always yield better reconstruction results when measurement noise is small. In presence of realistic noise, high sampling rates ($f \approx 10{,}000\ \mathrm{s}^{-1}$) are preferred only for shallowest temperature profiles ($z \leq 100\ \mu\mathrm{m}$), while moderate sampling rates ($f \approx$

1000 s^{-1}) are optimal for other temperature profiles. In general, optimal sampling rate depends on specifics of experimental system and studied samples.

Since the reduction of spectral acquisition band leads to smaller SNR, one must balance the deficiency of the monochromatic approximation and the effect of noise. To find the optimal spectral acquisition band, we performed an experiment on agar tissue phantoms, supported by numerical simulation. The results show that spectral filtering can reduce the image error δ and broadening of temperature peaks, especially for shallower and more complex absorbing structures. A suitable amount of spectral filtering is thus beneficial, despite the associated reduction of SNR. For the agar tissue phantoms and our PPTR system, numerical simulation results suggest an optimal long-pass filter with a cut-on wavelength of $\lambda_l = 3.8–4.2$ µm.

We also present a study involving experiments and numerical simulation of PPTR temperature profiling in collagen tissue phantoms, which more realistically resemble IR optical and thermal properties of human skin. Similar to the study involving agar tissue phantoms, the results indicate that appropriate spectral filtering significantly improves reconstruction results. Optimal results for gelatin tissue phantoms are obtained for spectral acquisition bands with $\lambda_l = 4.0–4.5$ µm. Furthermore, the reconstruction results are less affected by overiteration, when these spectral bands are used.

The monochromatic approximation can result in a significant image error, especially when non-optimal μ_{eff} is utilized. Therefore, we analyze also the reconstruction where the correct, spectrally composite kernel matrix is used. In general, this approach performs significantly better than the conventional monochromatic reconstruction regarding both accuracy and stability issues. However, the weaknesses of this approach are that the IR absorption spectrum of the sample must be known, and increased computational complexity of the kernel matrix.

Earlier PPTR studies suggested that PPTR temperature profiling is fairly efficient at determining temperature profile depths. But it was found using numerical simulations that the broadening of temperature profile is at least ~25% of the absorber depth, which limits the technique to the depth of 500 µm. To find limitations of our PPTR temperature profiling system, we performed an experiment on agar tissue phantoms and a numerical simulation involving planar impulses. Our experimental results indicate that PPTR temperature profiling accurately predicts locations of absorbing structures at least up to 900 µm. Still more, the average width of our experimental temperature profiles equals 15% of the absorbing layer depth in spite of noise and the linear error in measured PPTR signals. In addition, from numerical results we estimate the broadening to 13% of temperature profile central depth. Thus, our PPTR system performs significantly better than the earlier PPTR systems.

The evaluation of PPTR temperature profiling presented in the dissertation suggests that this technique can provide valuable information about internal structure of samples (i.e., temperature distribution). Therefore the technique can be used as a link between the actual structure of the lesion, parameters used in laser therapy of a vascular lesion, and the therapy outcome. We designed our PPTR system to be portable and as such can be clinically used, but a small and handy PPTR temperature profiling device would better suit clinical needs. The next step in the PPTR temperature profilometry could be the miniaturization of the setup, so that in future PPTR temperature profiling could be used in clinical practice for diagnostic characterization of vascular lesions and, possibly individual guidance of laser therapy.

Appendix A

Filter factors

Purpose of regularization of a discrete ill-posed problem is finding out which SVD components to filter out and how to filter them out. We introduce filter factors f_i, since they illustrate the effect of regularization and because they are necessary for implementation of generalized cross validation (GCV) method (chapter 4). Regularized solution $\boldsymbol{T}_{\mathrm{reg}}$ produced by our reconstruction algorithm can be obtained by inserting filter factors f_i into (4.4)

$$\boldsymbol{T}_{\mathrm{reg}} = \sum_{i=1}^{n} f_i \; (\boldsymbol{u}_i^{\mathrm{T}} \boldsymbol{S} / \sigma_i) \; \boldsymbol{v}_i \qquad \text{(A.1)}$$

Thus expression for the corresponding residual vector is

$$\boldsymbol{S} - \boldsymbol{K}\,\boldsymbol{T}_{\mathrm{reg}} = \sum_{i=1}^{n} (1 - f_i) \; (\boldsymbol{u}_i^{\mathrm{T}} \boldsymbol{S}) \; \boldsymbol{u}_i \qquad \text{(A.2)}$$

The filter factors f_i for the particular reconstruction algorithm characterize the damping or filtering of the SVD components. For some methods, there exist expilicit formulas for the filter factors (e.g., Tikhonov regularization, TSVD); for other methods, there are no known expressions for filter factors (e.g., CG). The filter factors are typically close to 1 for large σ_i and much smaller than 1 for small σ_i. Therefore the contributions to the regularized solution corresponding to the smaller σ_i are effectively filtered out. Evidently, $\boldsymbol{T}_{\mathrm{reg}}$ contains only SVD components, which are not dominated by errors in $\boldsymbol{S}$, and the residual vector contains only components due to errors, when optimal filter factors are chosen. As an example, the filter factors for TSVD algorithm are

$$f_i = \begin{cases} 1, & i \le p \\ 0, & i > p \end{cases} \qquad \text{(A.3)}$$

The sum of the filter factors $\rho(p)$ appears in the definition of the GCV function (4.6)

$$\rho(p) = \sum_{i=1}^{n} f_i(p) \qquad \text{(A.4)}$$

where p represents the regularization parameter. When we insert (A.3) and (A.4) into (4.6), we obtain the expression for the GCV function for TSVD (Eq. 4.7).

Appendix B

Chebyshev approximation for erfcx(*x*)

The monochromatic kernel matrix is derived in Chapter 2 as

$$\kappa(z,t) = \frac{1}{2}\exp[-z^2/(4D\,t)]\;\left\{\mathrm{erfcx}(u_-) + \mathrm{erfcx}(u_+) + \frac{2h}{\mu - h}\left[\mathrm{erfcx}(u_+) - \mathrm{erfcx}(u_1)\right]\right\} \tag{A.1}$$

with erfcx(u) = erfc(u) exp(u^2), $u_\pm = \mu\sqrt{Dt} \pm z/(2\sqrt{Dt})$, $u_1 = h\sqrt{Dt} + z/(2\sqrt{Dt})$.

Since erfc(x) quickly decreases to zero and exp(x^2) increases to infinity as x becomes large (e.g., erfc(10) = 2.1×10^{-45} and exp(10^2) = 2.7×10^{-43}), one must very carefully consider evaluation of functions erfcx(x) in (A.1) to avoid unacceptable overflow/underflow and numerical errors.

A Chebyshev approximation of erfcx(x) function[65] used in our code is presented in Algorithm A.1. Values obtained by this approximation match values obtained by Mathematica™ 4.0 with precision set to the machine precision (32-bit PC) for all x relevant for PPTR temperature profiling .

If an argument of exponential function exceeds ~ ±709.782 on a 32-bit platform, exponential function can not be evaluated due to overflow or underflow. Yet, $u_z = -z^2/4Dt$ can be smaller than -709.782 for small time t or large depth z, therefore we must assure that underflow does not happen. Algorithm A.2 shows our implementation of $\kappa(z, t)$ calculation, where we used the Chebyshev approximation of erf(x) function. Values of $\kappa(z, t)$ obtained in such a manner match values found by Mathematica™ 4.0.

Algorithm A.1: A Chebyshev approximation for function erfcx(*x*)

```
t = 3.97886080735226 / (fabs(x) + 3.97886080735226);
u = t - 0.5;
y = (((((((((0.00127109764952614092 * u + 1.19314022838340944e-4) * u -
        0.003963850973605135) * u - 8.70779635317295828e-4) * u +
        0.00773672528313526668) * u + 0.00383335126264887303) * u -
        0.0127223813782122755) * u - 0.0133823644533460069) * u +
        0.0161315329733252248) * u + 0.0390976845588484035) * u +
        0.00249367200053503304;
y = ((((((((((((y * u - 0.0838864557023001992) * u -
        0.119463959964325415) * u + 0.0166207924969367356) * u +
        0.357524274449531043) * u + 0.805276408752910567) * u +
        1.18902982909273333) * u + 1.37040217682338167) * u +
        1.31314653831023098) * u + 1.07925515155856677) * u +
        0.774368199119538609) * u + 0.490165080585318424) * u +
        0.275374741597376782) * t;
if(x < 0)
        return(2*exp(x*x)-y);
else
        return(y);
```

Algorithm A.2: Calculation of $\kappa(z, t)$ (Eq. A.1)

```
if($u_z$ < -708 and $u_z$ + $u_-^2$ > -708)
    $\kappa(z, t)$ = exp($u_z$ + $u_-^2$) erf($u_-$);
if($u_z$ < -708 and $u_z$ + $u_-^2$ < -708)
    $\kappa(z, t)$ = 0;
else
    $\kappa(z, t)$ = exp($u_z$)(erfc($u_+$)+ erfc($u_-$)+ 2$h$ (erfc($u_+$)- erfc($u_1$))/($\mu$ - $h$));
```

Appendix C

Extended abstract in Slovenian language

Povzetek disertacije v slovenščini

Sunkovna fototermalna radiometrija (SFTR) je brezdotična tehnika, ki temelji na infrardečem (IR) sevanju kot posledici laserskega obsevanja snovi. Svetloba se selektivno absorbira v absorberjih, kar ima za posledico lokalni dvig temperature, ki ga zaznamo kot prehodno povečanje IR sevanja vzorca. Izmerjena sprememba IR sevanja omogoča določitev globinskega temperaturnega profila, če so poznane termične lastnosti vzorca. S temperaturno profilometrijo SFTR je mogoče uspešno določiti porazdelitev absorberjev v močno sipajočih bioloških tkivih. Prednost temperaturne profilometrije SFTR pred komplementarnimi tehnikami je njena neinvazivnost.

V disertaciji bomo predstavili razvoj in evalvacijo sistema SFTR za temperaturno profilometrijo v bioloških tkivih. Delo je potekalo na Odseku za kompleksno snov Instituta Jožef Stefan, Ljubljana, Slovenija in je obsegalo razvoj rekonstrukcijskega algoritma, numerično analizo, postavitev in optimizacijo laboratorijskega sistema SFTR ter eksperimente s tkivnimi fantomi.

Povod za to delo je nepopolna uspešnost laserske terapije ognjenih znamenj. Ognjena znamenja so prirojene kožno-žilne tvorbe, ki jih sestavljajo patološko pomnožene in razširjene krvne žile v zgornjem milimetru kože. Zdravi se jih s selektivno fotokoagulacijo patoloških žil, pri čemer se uporabljata sunkovni zeleni laser (KTP; 532 nm) in rumeni/zeleni laser (sunkovni barvilni; 577 nm, 585–600 nm). Ker se globina in velikost žil, količina krvi ter globina epidermisa spreminjajo od pacienta do pacienta, je potrebna individualna določitev parametrov (dolžina sunka, intenziteta in valovna dolžina svetlobe), kar omogoča temperaturna profilometrija SFTR.

C.1 Teoretično ozadje

Signal SFTR je konvolucija začetnega temperaturnega profila $\Delta T(z, t)$

$$\Delta S(t) = \int_{z=0}^{\infty} K(z,t)\,\Delta T(z,0)\,\mathrm{d}z \tag{C.1}$$

z jedrno funkcijo $K(z,t)$

$$K(z,t) = C \int_{\lambda_\mathrm{l}}^{\lambda_\mathrm{h}} R(\lambda)\, B_\lambda'(T_\mathrm{b})\, \mu(\lambda) \int_0^{\infty} G_\mathrm{T}(z',z,t)\, e^{-\mu(\lambda)\, z'}\,\mathrm{d}z'\,\mathrm{d}\lambda\,, \tag{C.2}$$

kjer sta λ_l in λ_h spodnja in zgornja meja spektralnega pasu, v katerem se zajema signal, $R(\lambda)$ predstavlja občutljivost detektorja IR, T_b je osnovna temperatura, $B_\lambda'(T_\mathrm{b})$ je odvod Planckovega zakona po temperaturi, $\mu(\lambda)$ je IR absorpcijski koeficient vzorca in $G_\mathrm{T}(z', z, t)$ je enodimenzionalna Greenova funkcija za toplotno difuzijo. Konstanta C vsebuje emisivnost vzorca in ostale značilnosti sistema (izgube na lečju, vidni kot IR detektorja, itd.).

Kadar smemo namesto $\mu(\lambda)$ uporabiti spektralno neodvisen koeficient μ, dvojni integral v (C.2) razpade na dva samostojna integrala

$$\tilde{K}(z,t) \; = \; C \int_{\lambda_1}^{\lambda_h} R(\lambda)\, B_\lambda{}'(T_b)\, d\lambda \;\; \mu \int_0^\infty G_T(z',z,t)\, e^{-\mu z'}\, dz' \tag{C.3}$$

kjer je za dane eksperimentalne razmere prvi integral konstanten. Ko izračunamo drugi integral, dobimo analitičen izraz

$$\kappa(z,t) = \frac{1}{2}\exp[-z^2/(4D\,t)] \left\{ \mathrm{erfcx}(u_-) + \mathrm{erfcx}(u_+) + \frac{2h}{\mu - h}\left[\mathrm{erfcx}(u_+) - \mathrm{erfcx}(u_1)\right] \right\} \tag{C.4}$$

kjer je $\mathrm{erfcx}(u) = [1 - \mathrm{erf}(u)]\exp(u^2)$, $u_\pm = \mu\sqrt{Dt} \pm z/(2\sqrt{Dt})$, $u_1 = h\sqrt{Dt} + z/(2\sqrt{Dt})$. Pri eksperimentalnem delu sta tako signal kakor temperaturni profil diskretna, zato (C.1) postane algebraična enačba, kjer je signalni vektor $\boldsymbol{S}$ enak produktu jedrne matrike $\boldsymbol{K}$ s temperaturnim vektorjem $\boldsymbol{T}$

$$\boldsymbol{S} = \boldsymbol{K}\,\boldsymbol{T} \tag{C.5}$$

C.2 Postavitev eksperimenta

Slika C.1 prikazuje shemo sistema SFTR. Na vzorec posvetimo s sunkom laserske svetlobe, pri čemer mora biti osvetljena površina precej večja kot površina, s katere zajemamo radiometrični signal, da se zagotovi veljavnost enodimenzionalnega približka predstavljenega zgoraj. Radiometrični signal se preko lečja IR zbere na detektorju IR. Signal z detektorja se ojača na predojačevalniku in se prenese preko analogno-digitalnega pretvornika v računalnik. S fotodiodo določimo čas, ko je bil izsevan laserski sunek.

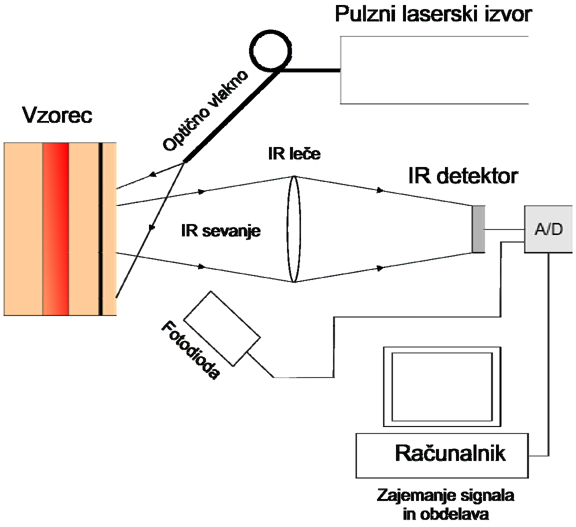

Slika C.1: Shema eksperimentalne postavitve sistema za temperaturno profilometrijo SFTR. A/D – analogno-digitalni pretvornik.

Kot izvir svetlobnega sunka pri tehniki SFTR se lahko uporabi katerikoli sunkovni izvor svetlobe, vendar v našem primeru uporabimo laser KTP (λ = 532 nm), saj tako zagotovimo enake razmere kot v primeru laserske terapije. Radiometrični signal zberemo na detektorju IR (InSb, λ = 3–5 μm, P5968-100, Hamamatsu) s silicijevimi lečami prevlečenimi z antirefleksno plastjo, ki zagotavlja ~98% prepustnost za svetlobo v srednjem območju IR (λ = 3–5 μm). Naš detektor IR ima vrh občutljivost pri λ_p = 5,3 μm, največjo občutljivost R_p = 2,5 A/W, površino 0,78 mm^2 in vidni kot 45°. Slika C.2 prikazuje spektralni občutljivosti uporabljenega detektorja, alternativnega HgCdTe detektorja ter temperaturni odvod Planckovega zakona $B_\lambda'(T_b)$.

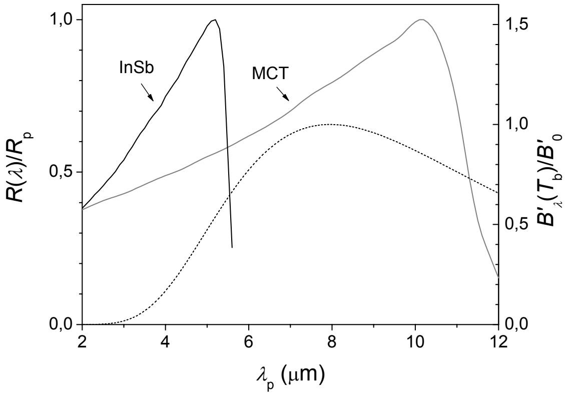

Slika C.2: Relativna spektralna občutljivost $R(\lambda)$ detektorjev InSb in HgCdTe (*polni črti*) in temperaturni odvod Planckovega zakona $B_\lambda'(T_b)$ pri $T_b = 303$ K z največjo vrednostjo pri $\lambda = 8$ μm.

V izmerjenemu radiometričnemu signalu se pojavi šum, ki ima več prispevkov. Prispevek, ki je odvisen od vpadne moči sevanja, je šum štetja, katerega amplituda je enaka

$$n_{sh} = \sqrt{2 e_0 i_s \Delta f} \tag{C.6}$$

Pri tem so i_s signalni tok, Δf frekvenčna širina in e_0 osnovni naboj. Drugi prispevki so še termični šum, šum ojačevalnika, šum diskretizacije, itd. V radiometričnih signalih se pojavlja tudi 1/f šum, katerega spektralno gostoto opišemo kot

$$\tilde{n}_t^2 = \tilde{n}_{bel}^2 \left[\left(\frac{f_c}{f} \right)^\alpha + 1 \right] \tag{C.7}$$

pri čemer so f frekvenca zajemanja, f_c kolenska frekvenca, α značilni eksponent in n_{bel} spektralna gostota belega šuma.

Eksperimentalno smo določili šum našega sistema in dobili sledeče vrednosti: amplituda celotnega šuma pri $\Delta f = 500\ s^{-1}$ je približno $n_t = 3 \times 10^{-10}$ A, kolenska frekvenca je $f_c = 15 \pm 10\ s^{-1}$ in eksponent $\alpha = 1{,}3 \pm 0{,}4$.

C.3 Rekonstrukcijski algoritmi

Inverzni problem SFTR (C.5) spada med slabo pogojene probleme, za katere je značilno, da so njihove rešitve zelo občutljive na motnje (npr., merski šum v signalu). Zato je reševanje tovrstnih problemov kompleksno in zahteva posebej prilagojene rekonstrukcijske algoritme. V ta namen smo razvili tri rekonstrukcijske algoritme. Prvi algoritem temelji na dekompoziciji po singularnih vrednostih (SVD), drugi na metodi konjugiranih gradientov (CG) in tretji na υ-metodi.

Rešitev inverznega problema SFTR je potrebno primerno regularizirati, t.j. omejiti množico rešitev z vnaprej določenim kriterijem in tako pridobiti uporabno rešitev. Najprej izpostavimo regularizacijske parametre za naše tri algoritme. Parameter je v primeru SVD število singularnih vektorjev vključenih v rešitev p (metoda postane skrajšana SVD oz. TSVD) ter v primeru CG in υ-metode število iteracij i. Nato smo poiskali metodo določanja optimalnih vrednosti regularizacijskih parametrov iz množice razpoložljivih metod za vsak rekonstrukcijski algoritem posebej. V obsežni numerični simulaciji smo preizkusili kombinacije gornjih treh rekonstrukcijskih algoritmov s tremi metodami izbire regularizacijskih parametrov: princip razlike (DP), L-krivulja in metoda GCV. Rezultati simulacije so pokazali, da so optimalne sledeče kombinacije: CG in L-krivulja, TSVD in GCV ter υ-metoda in Monte Carlo GCV. Monte Carlo GCV je posebna različica GCV metode, ki je posebej prilagojena za iterativne algoritme.

Gornji rekonstrukcijski algoritmi lahko dajo rešitve, ki vsebujejo nefizikalne nenegativne vrednosti rekonstruiranih temperaturnih profilov. Zato je potrebno v algoritme vgraditi nenegativni pogoj, ki to pomanjkljivost odpravi. Tako smo v primeru υ-metode uporabili princip projekcije (P), ki poreže vse negativne vrednosti rešitve pri vsaki iteraciji algoritma. V primeru metod TSVD in CG smo bili primorani uporabiti princip projekcije-ponovitve (PR), saj P znatno zmanjša učinkovitost teh dveh algoritmov. Princip PR je razdeljen na notranjo in zunanjo zanko. V notranji zanki se izvaja nespremenjen regulariziran rekonstrukcijski algoritem, v zunanji zanki pa se po izteku notranje zanke njena rešitev prišteje rešitvi v zunanji zanki, ki se ji nato odrežejo negativne vrednosti. Zaporedje notranje in zunanje zanke se ponavlja, dokler ni zadoščeno vnaprej določenim kriterijem. Algoritme, ki vključujejo nenegativnost in avtomatsko regularizacijo, smo poimenovali P υ-metoda, PR-TSVD in PR-CGLS.

Razvite algoritme smo nato primerjali z drugimi razpoložljivimi algoritmi in nato še med seboj. Najprej smo rezultate rekonstrukcije, objavljene v predhodni študiji SFTR, kjer je bil uporabljen komercialni algoritem Solver vključen v Microsoft Excel, primerjali z rezultati našega algoritma PR CGLS (Slika C.3).

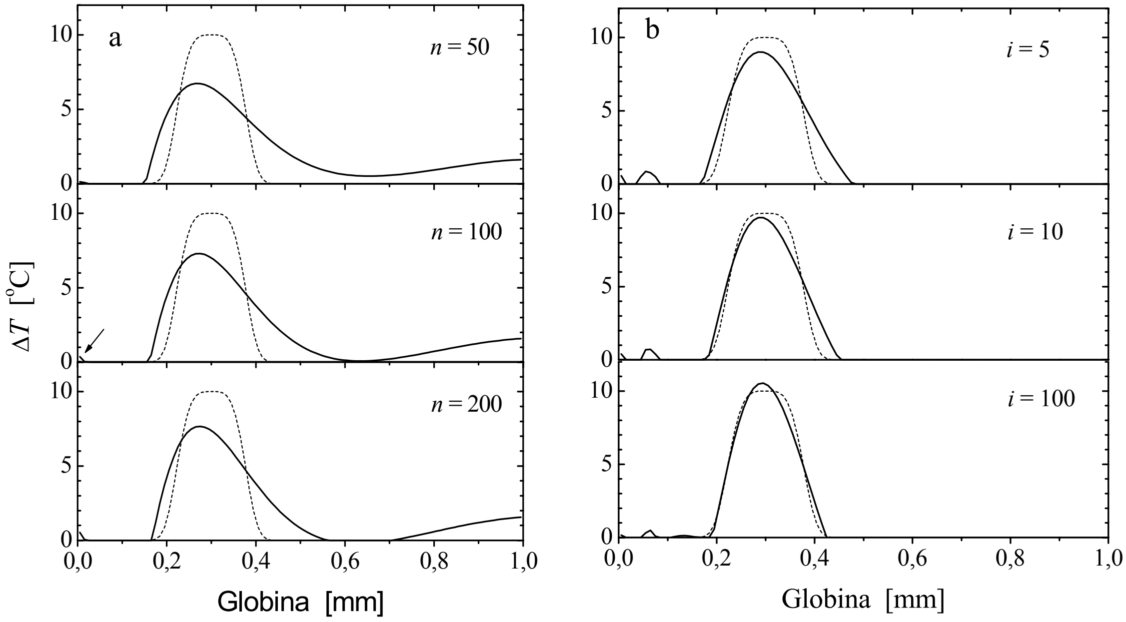

Slika C.3: Temperaturni profili rekonstruirani (a) s komercialnim algoritmom (Solver v Microsoft Excel-u) in (b) našim namenskim algoritmom PR-CGLS. Prikazani rezultati so dobljeni v n oz. i korakih algoritmov.

Očitno naš namenski rekonstrukcijski algoritem (Slika C.3b) omogoča natančnejšo rekonstrukcijo začetnega temperaturnega profila kot komercialni algoritem (Slika C.3a). Opravili smo tudi primerjavo med rekonstrukcijskimi rezultati, ki so jih dobili v eni izmed predhodnih študij SFTR z namenskim rekonstrukcijskim algoritmom, ki je temeljil na metodi CG in našimi tremi rekonstrukcijskimi algoritmi. Ugotovili smo, da imajo temperaturni profili, dobljeni z našimi algoritmi, približno 20% manjšo napako rekonstrukcije kot predhodni rezultati. Na koncu smo primerjali učinkovitost naših algoritmov med seboj in ugotovili, da so v povprečju rezultati vseh treh algoritmov primerljivi, vendar z algoritmom PR-TSVD občasno dobimo premalo regularizirano rešitev.

C.4 Kalibracija

Pri kalibraciji izmerjen signal SFTR prilagajamo na izmerjen odziv sistema SFTR na sevanje črnega telesa pri različnih temperaturah T_{BB}. S kalibracijo odpravimo eksperimentalne značilnosti, kot so prepustnost lečja, kot zajemanja in podobno ter odpravimo nelinearnost med radiometričnim signalom ter temperaturo telesa.

Kalibracija se običajno opravlja v monokromatskem približku, kjer predpostavimo eno valovno dolžino λ, konstantno občutljivost detektorja R in IR absorpcijskega koeficienta μ. Izraz za kalibriran monokromatski signal $\Delta S(t)$ je enak

$$\Delta S(t) = -\frac{hc/k_\mathrm{B}\lambda}{\ln \int\limits_{z=0}^{\infty} e^{-\frac{hc}{\lambda\, k_\mathrm{B}(T_b+\Delta T(z,t))}}\, e^{-\mu z}\, \mu \,\mathrm{d}z} - T_\mathrm{b} \tag{C.8}$$

kjer sta h in c Planckova konstanta in svetlobna hitrost in k_B je Boltzmannova konstanta. Kalibriran izraz se dodatno poenostavi, če ga lineariziramo

$$\Delta S_\mathrm{L}(t) = \mu \int\limits_{z=0}^{\infty} \Delta T(z,t)\, e^{-\mu z}\, \mathrm{d}z \tag{C.9}$$

V lineariziranem monokromatskem signalu $\Delta S(t)_\mathrm{L}$ ni več prisotnih faktorjev, ki bi bili odvisni od λ. Vendar pa linearizacija, ki je sicer potrebna za reševanje inverznega problema SFTR (C.5), privede do linearizacijske napake. Z razvojem (C.8) v Taylorjevo vrsto in ohranitvijo členov reda velikosti $\Delta \mathrm{T}(z, t)^2$ dobimo oceno za velikost linearizacijske napake kalibriranega signala SFTR

$$\begin{aligned} N_2\left(\Delta T(z,t)\right) &= \frac{1}{T_\mathrm{b}}\left(\frac{hc}{2\lambda k_\mathrm{B} T_\mathrm{b}} - 1\right) \times \\ &\times \left\{ \mu \int\limits_{z=0}^{\infty} \Delta T(z,t)^2\, e^{-\mu_\mathrm{eff} z}\, \mathrm{d}z - \left(\mu \int\limits_{z=0}^{\infty} \Delta T(z,t)\, e^{-\mu_\mathrm{eff} z}\, \mathrm{d}z \right)^2 \right\} \end{aligned} \tag{C.10}$$

Ocena (C.11) nam pokaže, da napaka pada s padanjem amplitude temperaturnega dviga $\Delta T(z, t)$ ter z naraščanjem valovne dolžine λ ter osnovne temperature T_b. V podporo analitični oceni smo izvedli numerično simulacijo, kjer smo izračunali napako zaradi linearizacije. V ta namen smo simulirali signale SFTR temperaturnih objektov s hiper-gaussovo obliko: $\Delta T(z,0) = T_\mathrm{p} \exp[-2(z-z_0)^4/w^4]$ with $T_\mathrm{p} = 1 - 100$ K, $w = 30$ µm in centralnimi globinami $z_0 = 100$, 200 in 300 µm. Točne in linearizirane signale smo izračunali z integraloma (C.8) in (C.9), in sicer v 1000 točkah v časovnem intervalu 1 s. Uporabljeni eksperimentalni parametri so: $\lambda = 4{,}5$ µm, $\mu = 26{,}5$ mm^{-1}, $T_\mathrm{b} = 303$ K, $D = 0{,}11$ mm^2/s in $h = 0{,}02$ mm^{-1}.

Iz točnih signalov (enačba C.8) smo rekonstruirali temperaturne profile (Slika C.4), da bi ugotovili, kako napaka vpliva na kvaliteto rekonstrukcij. Za rekonstrukcijo smo uporabili P-υ-metodo.

Iz slike C.8 je razvidno, da se vpliv linearizacijske napake zmanjšuje z manjšanjem amplitude T_p in večanjem globine objekta z_0. Poleg površinskih artefaktov (*glej puščice*) se v primeru amplitud $T_\mathrm{p} = 50$ in 100 K ter globine $z_0 = 100$ µm pojavi tud premik objekta proti večjim globinam.

Poleg rekonstrukcij smo izračunali relativno napako linearizacije (slika C.9) za vse simulirane objekte. Relativna napaka skoraj izgine v 10–100 ms.

Simulirali smo tudi točne ter linearizirane signale SFTR za spektralne pasove s spodnjo mejo $\lambda_\mathrm{l} = 3{,}0$–4,9 µm in izračunali relativno napako na enak način kot v primeru monokromatskih signalov. Poleg enakih trendov kot v monokromatskem primeru, smo opazili, da linearizacijska napaka pada tudi z zožitvijo spektralnih pasov.

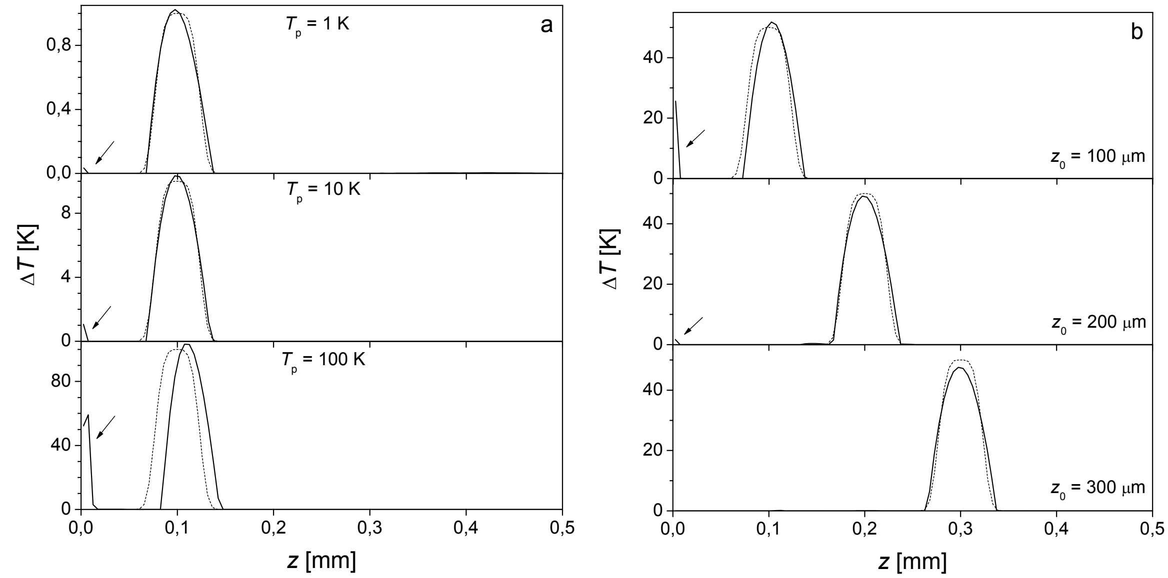

Slika C.8: Rekonstruirani temperaturni profili ΔT iz točnih monokromatskih kalibriranih signalov SFTR $\Delta S(t)$ (enačba C.8) za (a) testne objekte na globini z_0 = 100 μm s T_p = 1–100 K (*glej označbe*) in (b) testne objekte na globinah z_0 = 100–300 μm s T_p = 50 K (*glej označbe*). Pravi testni objekt je dodan za primerjavo (*črtkane črte*). Puščice označujejo površinske artefakte zaradi linearizacijske napake.

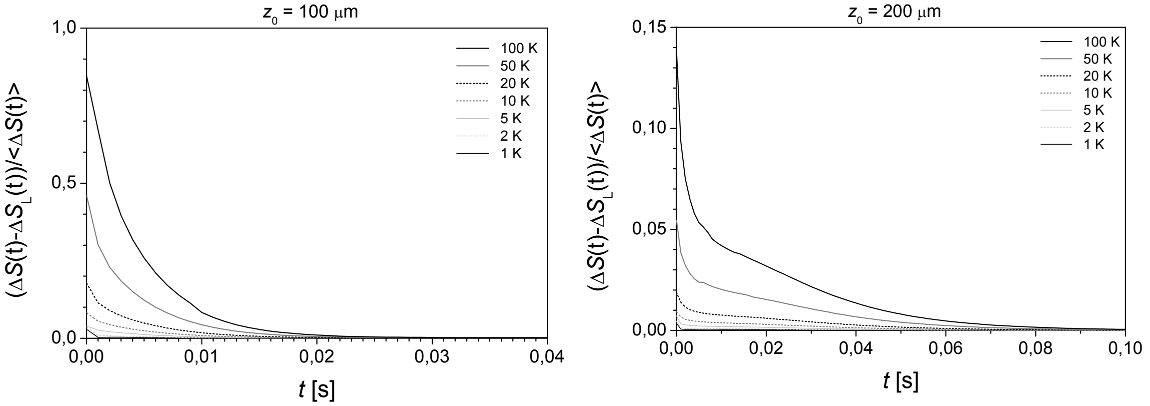

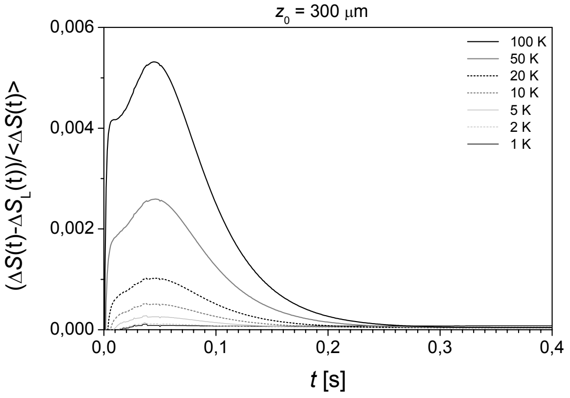

Slika C.9: Relativna linearizacijska napaka za objekte z z_0 = 100, 200 in 300 μm izračunana kot $(\Delta S(t) - \Delta S_L(t))/<\Delta S(t)>$, kjer je $<\Delta S(t)>$ povprečna vrednost $\Delta S(t)$. Vrednosti temperaturnih amplitud so T_p = 1 – 100 K (*glej označbe*), valovna dolžina je λ = 4,5 μm in IR absorpcijski koeficient je μ = 26,5 mm^{-1}.

C.5 Efektivni IR absorpcijski koeficient

V temperaturni profilometriji SFTR se običajno uporablja širok spektralni pas, saj se s tem izboljša razmerje med signalom in šumom (SNR). Hkrati se za rekonstrukcijo uporablja konstanten efektivni IR absorbcijski koeficient μ_{eff}, zato da se zmanjša računsko zahtevnost. Uporaba tovrstnega približka pri profilometriji v bioloških vzorcih SFTR, kjer je prisotna velika variabilnost $\mu(\lambda)$, lahko povzroči napake v rekonstrukciji temperaturnih profilov.

Da bi ugotovili, kakšen je vpliv monokromatskega približka na kvaliteto rekonstrukcij in da bi poiskali optimalne vrednosti μ_{eff} za različne spektralne pasove, smo izvedli numerično simulacijo. Naši testni objekti so imeli hiper-gaussovo obliko (*glej zgoraj*) s parametri ΔT_0 = 10 K, w = 100 µm in z_0 = 100–400 µm. Uporabili smo spektralne (75% $\mu(\lambda)$ vode in 25% $\mu(\lambda)$ kolagena) in termične lastnosti (D = 0,11 mm^2/s in h = 0,02 mm^{-1}) značilne za človeško kožo. Spektralne signale SFTR smo simulirali za različne spektralne pasove detektorjev InSb (λ = 3,0–5,6 µm) ter dveh HgCdTe (λ = 3,0–12,0 µm in λ = 3,0–14,0 µm). Temperaturne profile smo rekonstruirali iz simuliranih signalov z uporabo različnih vrednosti μ_{eff}. Kvantitativno smo ocenili napako rekonstrukcije kot

$$\delta = \frac{\left\| \boldsymbol{T} - \boldsymbol{T}_0 \right\|_2}{\left\| \boldsymbol{T}_0 \right\|_2} \tag{B.11}$$

kjer sta $\boldsymbol{T}$ vektor rekonstruiranega profila in $\boldsymbol{T}_0$ vektor testnega objekta. Slika C.10 prikazuje rekonstrukcije testnega objekta na globini z_0 = 300 µm, kjer so bile uporabljene premajhna (*zgoraj*), pravšnja (*sredina*) in prevelika (*spodaj*) vrednost μ_{eff}. Tako premajhna kot prevelika vrednost μ_{eff} očitno zmanjšata kvaliteto rekonstrukcije.

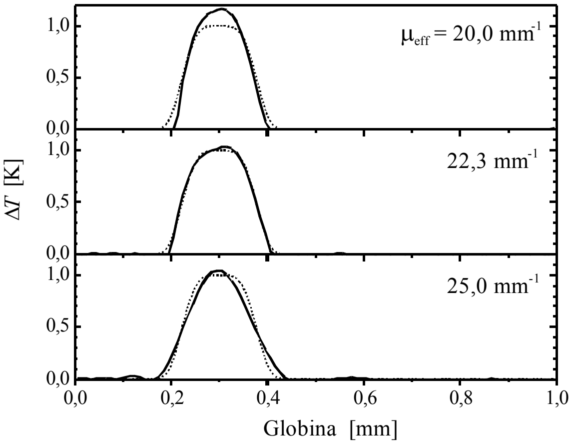

Slika B.10: Temperaturni globinski profil (*sklenjene črte*) rekonstruirane iz simuliranega signala SFTR za celoten pas detektorja InSb (λ = 3,0–5,6 µm). Uporabljena vrednost μ_{eff} je bila premajhna (*zgoraj*), skoraj optimalna (*sredina*) in prevelika (*spodaj*). Testni objekt je prikazan za primerjavo (*črtkana črta*).

Za vsak simuliran spektralni pas in testni objekt smo določili optimalno vrednost μ_{eff} tam, kjer je bila napaka rekonstrukcije δ najmanjša. Slika C.11a prikazuje optimalne efektivne IR absorpcijske koeficiente μ_{opt}. Očitno vrednost μ_{opt} pada z globino objekta. Iz slike C.11b, ki prikazuje ustrezne vrednosti δ, je razvidno, da se napaka rekonstrukcije δ zmanjšuje z zoženjem spektralnega pasu, zaradi izboljšane veljavnosti monokromatskega približka. Iz slike je tudi razvidno, da napaka δ narašča z globino objekta. $\mu_{\mathrm{opt}}(z_0)$ smo uravnotežili z $1/z_0$ faktorjem ter tako dobili uteženo povprečje $\bar{\mu}_{\mathrm{opt}}$ (Slika C.12), ki da zadovoljive rezultate za vse globine.

Ker je določanje μ_{opt} iz rezultatov numerične simulacije zelo zamudno, smo izpeljali nov analitičen pristop za določanje μ_{opt}, ki sloni na rešitvah enačbe

$$\mu_{\mathrm{eff}}\ e^{-\mu_{\mathrm{eff}}\,z} = \int_{\lambda_\mathrm{l}}^{\lambda_\mathrm{h}} R(\lambda)\, B_\lambda'(T_\mathrm{b})\, \mu(\lambda)\, e^{-\mu(\lambda) z}\, \mathrm{d}\lambda \Big/ \int_{\lambda_\mathrm{l}}^{\lambda_\mathrm{h}} R(\lambda)\, B_\lambda'(T_\mathrm{b})\, \mathrm{d}\lambda \tag{C.12}$$

Iz rešitev (C.12) μ_{eff} za dane spektralne pasove se nato izračuna μ_{opt} kot uteženo povprečje

$$\mu_{\mathrm{opt}} = \frac{\sum_i \mu_{\mathrm{eff}}(z_i)\ \mathrm{e}^{-\mu_{\mathrm{eff}}(z_i) z_i}}{\sum_i \mathrm{e}^{-\mu_{\mathrm{eff}}(z_i) z_i}} \tag{B.13}$$

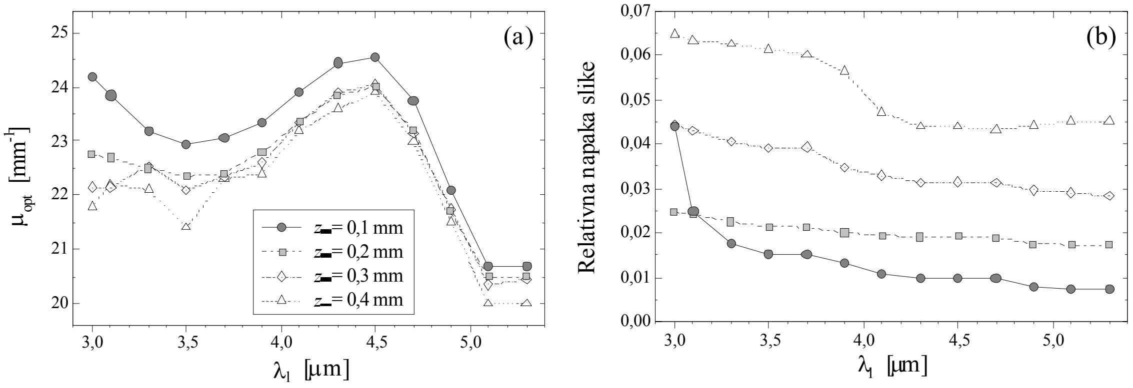

Slika C.11: (a) Optimalni efektivni IR absorpcijski koeficient $\mu_{\mathrm{opt}}(z_0)$ za objekte na globinah z_0 = 100–400 μm kot funkcija spodnje meje spektralnega pasu λ_l detektorja InSb. Zgornja meja spektralnega pasu je bila ves čas λ_h = 5,6 μm. (b) Pripadajoče relativne napake rekonstrukcije.

Optimalni absorpcijski koeficienti μ_{opt} določeni iz rezultatov numerične simulacije in z našim analitičnim pristopom (C.12 in C.13) za detektor InSb, se zelo dobro ujemajo (Slika C.12). Za primerjavo so prikazane tudi μ_{opt} izračunane, kot je bilo predlagano v predhodnih študijah SFTR. Očitno je ujemanje slednjih z rezultati numerične simulacije precej slabše, kot v primeru novega analitičnega pristopa.

Podobne rezultate smo dobili tudi za oba detektorja HgCdTe, kar nakazuje, da je predstavljen pristop uporaben za določitev μ_{opt} za poljuben detektor IR, spektralni pas in vzorec, če poznamo njihove spektralne odvisnosti.

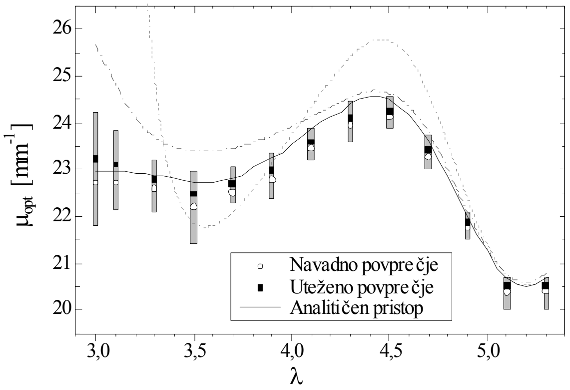

Slika C.12: Analitične vrednosti μ_{opt} (C.13) kot funkcija λ_l (*polna črta*). Sivi trakovi označujejo interval, na katerem se nahajajo vrednosti $\mu_{\mathrm{opt}}(z)$ za objekte na globinah z_0 = 100–400 μm; beli krogi in črni kvadrati označujejo navadno in uteženo povprečje. Rezultati dveh predhodnih analitičnih pristopov k določitvi μ_{opt} so prikazani s črtkanima črtama.

C.6 Frekvenca zajemanja

Parameter sistema SFTR je tudi frekvenca zajemanja podatkov f. V člankih na temo SFTR se pojavljajo frekvence med 200 in 2000 s^{-1}, vendar brez navedbe dejstev, zakaj so bile take vrednosti izbrane. Odvisnost natančnosti rekonstruiranih temperaturnih profilov od f smo preverili z numerično simulacijo. Simulirali smo signale SFTR v pasu λ = 3,0–5,0 μm za testne objekte, kot posledico absorpcije svetlobe v plasti absorberja debeline 50 μm z začetkom na globinah z_1 = 50–500 μm. Prednost takšnih testnih objektov je, da je mogoče analitično izračunati integral (C.1) in tako dobiti analitični izraz za $\Delta S(t)$. Signale smo izračunali za frekvence zajemanja f = 100–10.000 s^{-1} v času t = 1 s.

Iz simuliranih signalov smo rekonstruirali pripadajoče temperaturne profile $\boldsymbol{T}$ in ugotovili, da v primeru, ko v signalu SFTR ni prisotnega šuma, signali z višjo frekvenco f omogočijo natančnejšo rekonstrukcijo temperaturnih profilov.

V nadaljevanju smo simuliranim signalom dodali realističen šum z amplitudo ustrezno pasovni širini zajemanja Δf. Iz signalov s šumom smo rekonstruirali profile testnih objektov, določili napako rekonstrukcije δ (Slika B.13a) in širino W (Slika C.13b).

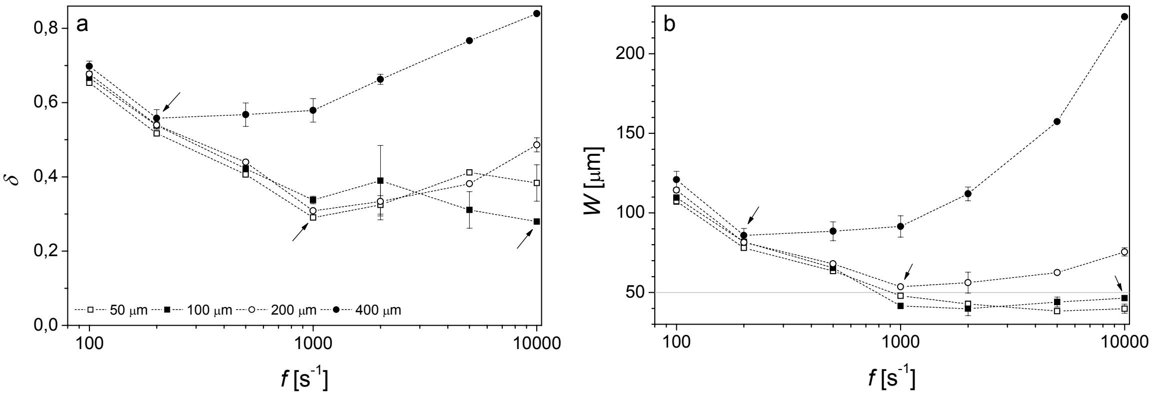

Slika C.13: (a) Relativna napaka rekonstrukcije δ in (b) širina profila W kot funkciji frekvence zajemanja f za testne objekte na globinah z_1 = 50–400 μm (*glej oznake*) in zašumljene signale SFTR. Siva črta v (b) označuje pravo širino objekta. Puščice kažejo optimalne vrednosti.

Iz Slike C.13 je razvidno, da je v primeru zašumljenih signalov visoka frekvenca 10.000 s^{-1} optimalna samo za objekt na globini 100 μm, medtem ko je za globlje objekte optimalna frekvenca f = 1000–2000 s^{-1}. Prenizke frekvence (~100 s^{-1}) vedno povzročijo neoptimalno rekonstrukcijo, kar je posledica pomanjkanja informacij v zajetem signalu. Zaradi nizkih vrednosti SNR signali zajeti z visoko frekvenco ne omogočajo kvalitetne rekonstrukcije globljih objektov.

C.7 Tkivni fantomi

Razvoj nove diagnostične tehnike zahteva izdelavo vzorcev z dobro definirano zgradbo in poznanimi snovnimi lastnostmi. Zato smo v namen evalvacije našega sistema SFTR izdelali tkivne fantome, ki temeljijo na vodnih gelih, katerih dobra lastnost je, da imajo podobne IR optične in termične lastnosti kot človeška koža.

Prvi izmed uporabljenih gelov je agar, katerega prednost je preprosta izdelava tankih plasti. Mešanico agarja in vode smo pripravili tako, da smo v 6 ml destilirane vode vmešali 0,15 mg agarja v prahu. Polimerizacijo smo sprožili v mikrovalovki, nakar smo tekočo zmes vlili v pripravljen kalup. Ko je agar polimeriziral, smo dobili homogene plasti agarja, katerih debelina je bila od nekaj 10 μm navzgor.

Drugi uporabljen vodni gel je želatin. Mešanico želatina smo pripravili tako, da smo v 75 masnih % vode vmešali 25 masnih % želatina v prahu. Mešanico smo segreli v vodni kopeli pri temperaturi

75 °C ter tako sprožili polimerizacijo. Tekočo zmes želatina in vode smo vlili v kalup, ga postavili v hladilnik in počakali na konec polimerizacije. Na tak način smo dobili plasti želatina poljubnih debelin (najmanjša debelina je bila ~30 µm).

Za obe vrsti gelov smo izmerili IR spekter $\mu(\lambda)$ ter poiskali vrednosti difuzijskih konstant. V gele smo vmešali tudi ustrezno količino sipalca, da bi lastnosti tkivnih fantomov še dodatno približali pravi koži.

Naslednja stopnja je bila priprava absorpcijske plasti. Možen način priprave je tanek nanos finega ogljikovega prahu na površino gela, nakar se to plast prekrije z drugo plastjo gela. Drug način priprave je uporaba tanke absorbirajoče folije, ki se jo vloži med dve plasti gela. Tretji način je vmešanje absorberja v plast gela (npr. črnilo). Več plasti gela in absorberjev se sestavi v tkivni fantom, ki ga shematsko prikazuje Slika C.14.

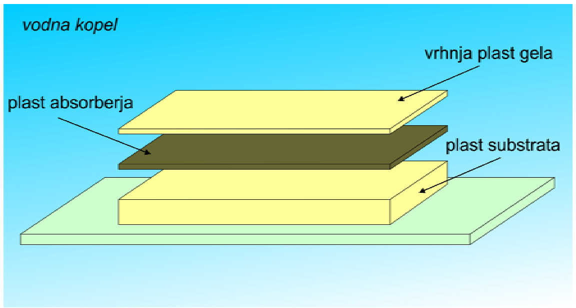

Slika C.14: Shema tkivnega fantoma z eno plastjo absorberja. Vodna kopel prepreči nastanek zračnih mehurčkov na stiku med plastmi.

C.8 Spektralno filtriranje

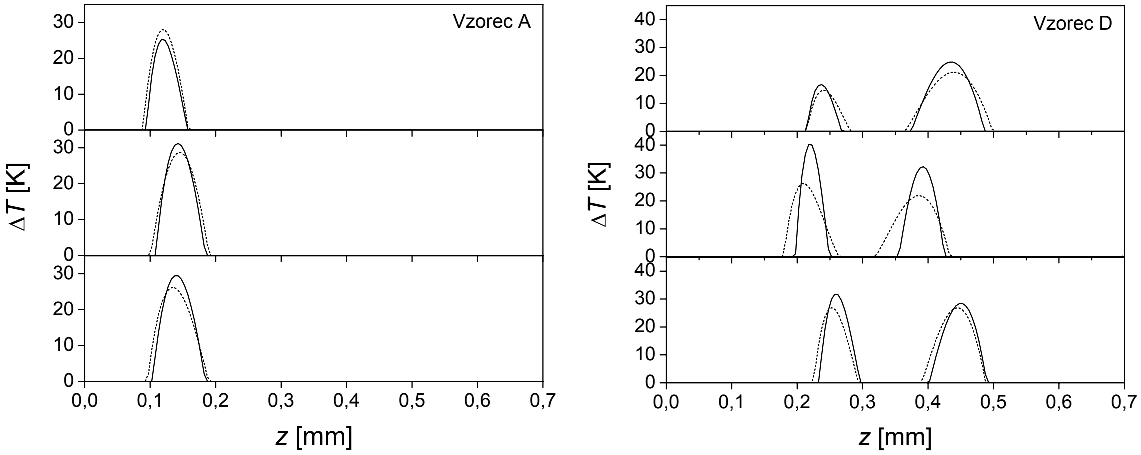

Slika C.15: Rekonstruirani temperaturni profili s treh mest na vzorcih A in D. Signali SFTR so bili zajeti s polnim (*črtkana črta*; λ = 3,0–5,6 µm) in zoženim spektralnim pasom (*polna črta*; λ = 4,5–5,6 µm).

Kot se je izkazalo v primeru iskanja optimalne vrednosti μ_{eff}, zoževanje spektralnega pasu izboljša veljavnost monokromatskega približka. Vendar pa zoževanje povzroči zmanjševanje SNR zajetih signalov SFTR, kar pa tudi poslabša kvaliteto rekonstrukcije. Torej obstajajo spektralni pasovi, kjer je skupen efekt obeh motenj minimalen in s tem omogočajo optimalno rekonstrukcijo. Zato smo izvedli eksperiment na tkivnih fantomih iz agarja, ki so vsebovali eno plast absorberja na globini 130, 280 in 450 µm (vzorci A, B in C) ter dve plasti absorberja na globinah 240 in 440 µm (vzorec D). Signale SFTR smo zajeli v spektralnem pasu λ = 3,0–5,6 µm in v zoženem spektralnem pasu λ = 4,5–5,6 µm. Za oba pasova smo določili μ_{opt} ter iz signalov rekonstruirali temperaturne profile v vzorcih. Globine absorpcijskih plasti smo hkrati določili tudi z optično koherenčno tomografijo (OCT) in histološko rezino pod optičnim mikroskopom.

Slika B.15 prikazuje rekonstruirane profile vzorcev A in D v primeru celotnega (*črtkana črta*) in zoženega spektralnega pasu (*cela črta*) na treh različnih mestih na vzorcu. V obeh primerih je izboljšanje rekonstrukcij zaradi zoženja spektralnega pasu očitno. V primeru globljih vzorcev B in C izboljšanje rekonstrukcij ni tako očitno.

Slika C.16 prikazuje slike OCT vzorcev A in D. Globine absorpcijskih plasti določenih iz rekonstruiranih profilov in iz slik OCT se ujemajo v okviru merske napake. Razlike med globinami določenimi z OCT ali SFTR ter tistimi, določenimi iz histološke slike, so nekoliko večje, kar je posledica priprave histološke rezine. Pomembna ugotovitev je tudi, da se globine določene za poln oz. zožen spektralni pas ne razlikujejo bistveno, kar pomeni, da spektralno filtriranje ne vpliva bistveno na natančnost določenih globin.

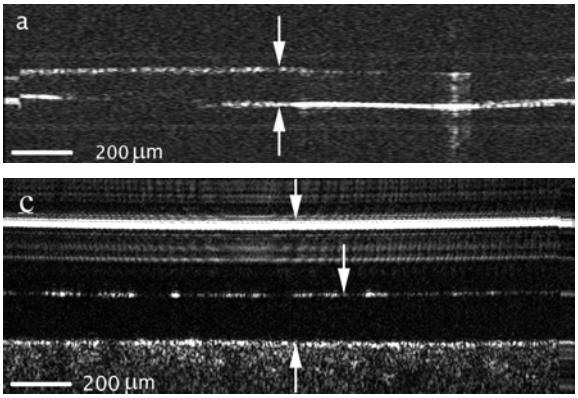

Slika B.16: Sliki OCT vzorcev (a) A in (c) D. Zgornji puščici kažeta površino vzorca, spodnji puščici globoko absorpcijsko plast in sredinska puščica v primeru vzorca D kaže prvo plast absorberja.

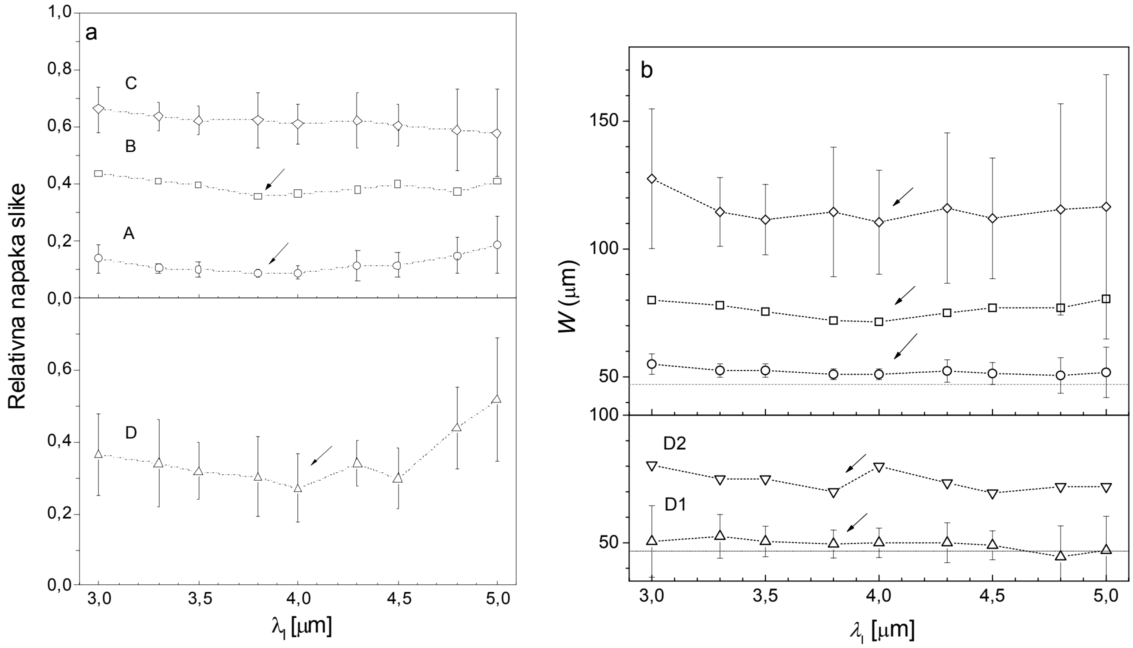

Slika C.17: (a) Relativna napaka rekonstrukcije δ kot funkcija λ_l za testne objekte A–D (*glej oznake*). (b) Širina rekonstruiranih temperaturnih profilov W. D1 in D2 predstavljata prvi in drugi vrh objekta D. Standardne deviacije so prikazane kot palice. Črtkana črta v (b) prikazuje točno širino testnih objektov (W = 47 μm). Puščice kažejo optimalne vrednosti.

Eksperimentalne rezultate smo podprli z rezultati numerične simulacije, kjer smo simulirali signale SFTR za testne objekte, ki so ponazarjali eksperimentalne temperaturne profile. Signale SFTR smo simulirali za različne spektralne pasove s spodnjo mejno valovno dolžino λ_{l} = 3,0–5,0 µm in zgornjo mejno valovno dolžino λ_{h} = 5,6 µm. Rezultati simulacij so pokazali, da primerno spektralno filtriranje (λ_{l} = 3,8–4,0 µm) zmanjša napako rekonstrukcij δ (Slika C.17a) in razširitev profilov W (Slika C.17b).

C.9 Spektralno filtriranje v kolagenskih vzorcih

Učinek spektralnega filtriranja na kakovost rekonstrukcij smo preverili tudi v kolagenskih vzorcih, ker so ti po lastnostih bolj podobni človeški koži kakor vzorci iz agarja. Najprej smo izvedli numerično simulacijo, kjer smo simulirali signale SFTR temperaturnih profilov s hiper-gaussovo obliko na globinah z_0 = 50–640 µm in širino w = 33 µm in signale temperaturnega profila z dvema hiper-gaussovima vrhovoma na globinah 50 in 280 µm. Signale SFTR smo simulirali za spektralne pasove detektorja InSb z λ_{l} = 3,0–5,0 µm ter jim dodali ustrezno količino realističnega šuma, ki je vključeval tudi 1/f šum. Ker so rezultati rekonstrukcije zelo občutljivi na praktično izvedbo šuma, smo vsakemu brezšumnemu signalu SFTR dodali po 30 različnih realizacij šuma. Iz signalov smo rekonstruirali temperaturne profile z uporabo υ-metode. Pri rekonstrukciji smo uporabili dva pristopa: rekonstrukcija z monokromatsko jedrno matriko (*monokromatska rekonstrukcija*), kjer smo μ_{opt} določili, kot je opisano zgoraj, ter s točno jedrno matriko (*spektralna rekonstrukcija*). Rezultate smo statistično obdelali in določili relativno napako rekonstrukcije δ in širino W.

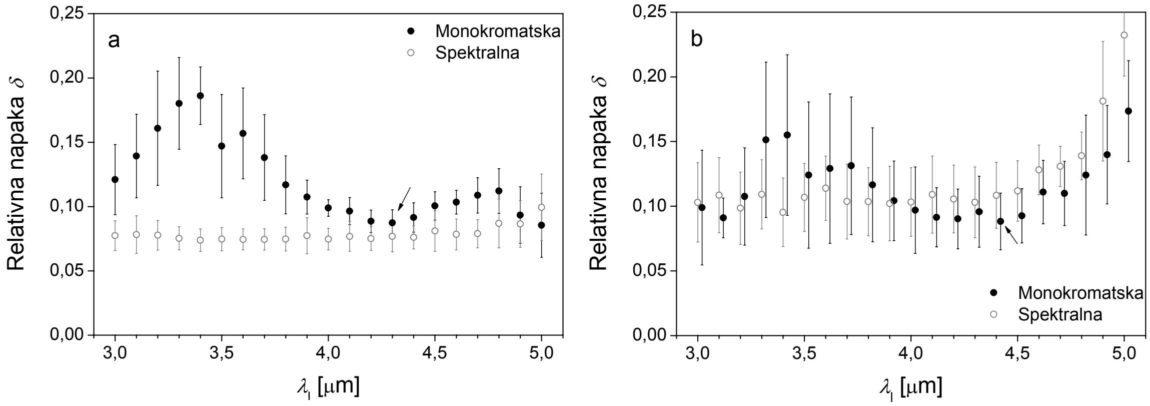

Slika C.18: Relativna napaka rekonstrukcije δ in standardna deviacija σ_δ (*palice*) kot funkciji λ_{l} za primer monokromatske rekonstrukcije (*črni krogci*) in spektralne rekonstrukcije (*prazni krogci*). Napake so bile določene za testne objekte na globinah (a) z_0 = 50 µm in (b) z_0 = 100 µm. Puščice kažejo optimalno λ_{l}.

Izkaže se, da monokromatska rekonstrukcija v primeru spektralnih pasov λ_{l} = 4,0–4,5 µm da najbolj kvalitetne rekonstrukcije, kar je razvidno iz Slike C.18, kjer je prikazana relativna napaka rekonstrukcije δ v odvisnosti od λ_{l} za objekta na globinah z_0 = 50 in 100 µm. Podobne rezultate za δ smo dobili tudi za temperaturni objekt z dvema vrhoma. Pri globljih objektih je efekt spektralnega filtriranja zakrit v standardni deviaciji relativne napake δ, ki je posledica nižjih vrednosti SNR. Podobne trende kot za δ smo dobili tudi za W in T_{p}. Slika C.18 prikazuje tudi napako rekonstrukcije δ za primer spektralne rekonstrukcije in za temperaturna objekta na globinah z_0 = 50 in 100 µm. Za razliko od monokromatske rekonstrukcije, vsi spektralni pasovi z λ_{l} = 3,0–4,5 µm dajo rekonstrukcije primerljive kvalitete. S spektralno rekonstrukcijo dobljeni temperaturni profili imajo manjšo napako δ kakor tisti dobljeni z monokromatsko rekonstrukcijo pri istem spektralnem pasu. Podobne rezultate kot za objekta z z_0 = 50 in 100 µm smo dobili tudi za objekt z dvema temperaturnima vrhoma, medtem ko je za globlje objekte odvisnost od spektralnega pasu skrita v standardni deviaciji δ. Podobne trende kot za δ smo opazili tudi pri W.

Numerične rezultate smo podprli tudi z eksperimentom na kolagenskih vzorcih. Signale SFTR smo zajeli v celotnem spektralnem pasu detektorja InSb. Tako z monokromatsko kot spektralno rekonstrukcijo smo dobili primerljive rezultate.

Če povzamemo, spektralno filtriranje izboljša natančnost rekonstruiranih profilov, kadar se uporabi monokromatska rekonstrukcija. V primeru spektralne rekonstrukcije taka izboljšava ni opazna. Upoštevati pa je potrebno, da naša simulacija ni vključevala napake linearizacije, za katero smo ugotovili, da se zmanjšuje s spektralnim filtriranjem.

C.10 Natančnost temperaturne profilometrije SFTR

Pri temperaturni profilometriji SFTR je znan pojav razširitve in atenuacije temperaturnih profilov z globino, medtem ko je določanje lege absorbirajočih struktur precej dobro. Da bi ocenili omejitve našega sistema SFTR, smo izvedli eksperiment na tkivnih fantomih iz agarja.

Pripravili smo 7 tkivnih fantomov z eno plastjo absorberja na globinah 40, 130, 270, 420, 600, 750 in 900 μm ter tri fantome (B1–D1) z absorpcijsko plastjo na globinah 180, 300 in 470 μm. Za absorber je služila tanka folija debeline ~20 μm. Vsak vzorec smo osvetlili z 1 ms dolgimi laserskimi sunki svetlobe iz laserja KTP/Nd:YAG (λ = 532 nm; Dualis^{VP}, Fotona, Ljubljana, Slovenija). Uporabili smo tri različne energije sunkov (H = 3,0, 5,0 in 7,8 J/cm^2). Signale s frekvenco 50.000 s^{-1} smo zajemali z uporabo celotnega pasu InSb detektorja (λ = 3,0–5,6 μm). S povprečenjem smo znižali frekvenco signalov na 1000 s^{-1} in frekvenčno širino zajemanja na 500 s^{-1}. Na ta način smo zmanjšali amplitudo šuma v signalih. Profile smo rekonstruirali z uporabo spektralne jedrne matrike, kjer je $\mu(\lambda)$ ustrezal izmerjenem spektru za agar. Poleg profilometrije SFTR smo izmerili globino vseh vzorcev še z optičnim mikroskopom in na treh ločenih vzorcih (B1–D1) z mikro magnetno resonančnim slikanjem (MRI).

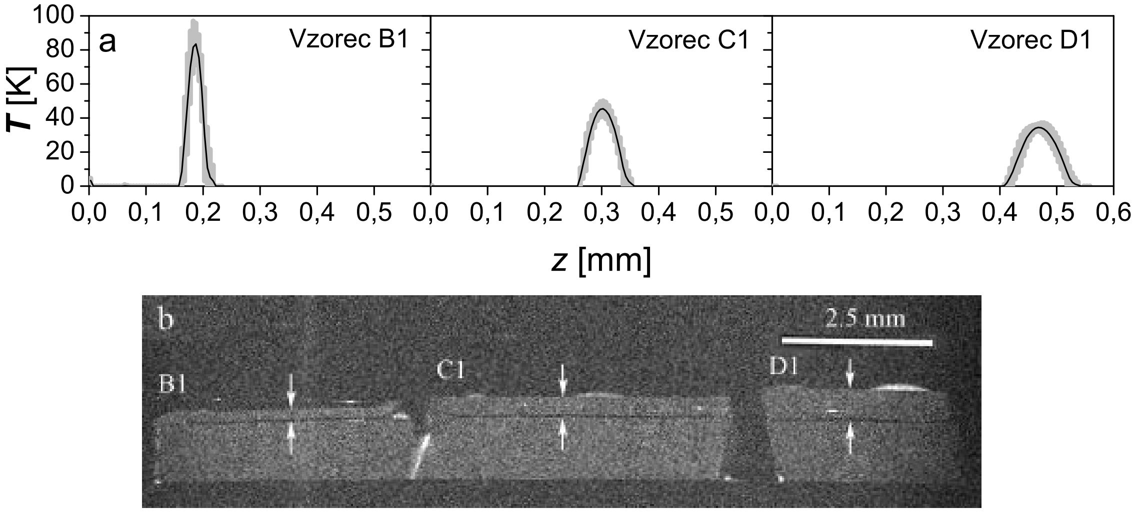

Slika C.19: (a) Povprečni temperaturni profili (*polne črte*) in standardne deviacije (*sive palice*) rekonstruirani iz 10 signalov SFTR zajetih z vzorcev B1–D1 pri H = 3,0 J/cm^2. (b) Mikro-MRI vzorcev B1 (*levo*), C1 (*center*) in D1 (*desno*). Zgornje puščice kažejo površino fantoma in spodnje puščice kažejo absorpcijsko plast.

Slika C.19a prikazuje rekonstruirane profile vzorcev B1–D1 in Slika C.19b mikro-MRI istih vzorcev. Ugotovili smo, da se globine absorpcijskih plasti določene s SFTR popolnoma ujemajo z globinami določenimi z mikro-MRI. Podobno ujemanje smo dobili za preostale vzorce med SFTR in optično mikroskopijo. Iz slike C.19a je razvidno tudi, da se temperaturni profil z globino razširja in niža. Izkaže se, da na razširitev poleg globine vpliva tudi SNR. Da bi dobili oceno razširitve, smo izvedli numerično simulacijo, kjer smo za testne objekte uporabili delta plasti, ki se nahajajo na istih globinah kot eksperimentalne absorpcijske plasti. Signale SFRT smo simulirali pri enakih pogojih, kot je potekal eksperiment, kar pomeni, da smo jim dodali tudi ustrezen šum z eksperimentalno določeno amplitudo. Na podlagi numeričnih rezultatov smo predpostavili sledečo zvezo za oceno razširitve temperaturnih profilov

$$w(z_0, SNR) = 0{,}133\, z_0 + \frac{2000\,\mu\text{m}}{SNR} \tag{C.14}$$

Iz (C.14) je razvidno, da je v primeru visokega SNR razširitev profilov enaka ~13% globine profila.

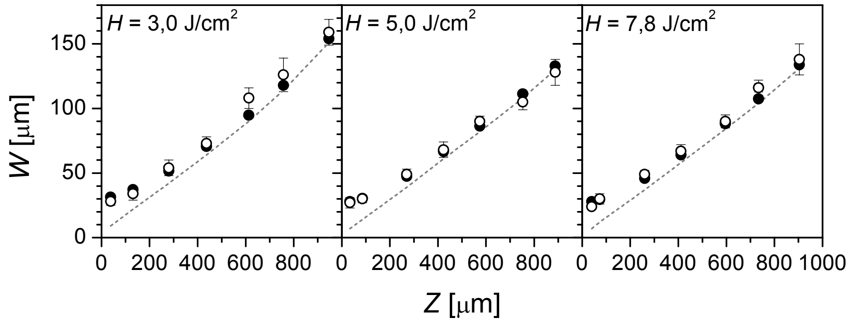

Slika C.20: Razširitev $w(z_0, SNR)$ delta plasti (*črtkane črte*) izračunane z (C.14) za globine in SNR vrednosti, dobljene pri eksperimentu za energije H = 3,0 (*levo*), 5,0 (*center*) in 7,8 J/cm^2 (*desno*). Ocenjena širina, ki vključuje efekt razširitve $w(z_0, SNR)$ in dejanske debeline plasti (*črni krogci*) ter izmerjena širina eksperimentalnih temperaturnih profilov (*prazni krogci*).

Slika C.20 prikazuje širine absorpcijskih plasti izmerjene iz rekonstruiranih temperaturnih profilov v vzorcih A–G (*prazni krogci*), razširitev ocenjeno z (C.14) (*črtkana črta*) in oceno, ki upošteva tako razširitev kakor dejansko širino absorpcijske plasti (*polni krogci*). Ujemanje med dejansko širino in ocenjeno širino je zadovoljivo, kar kaže, da je (C.14) dobra ocena razširitve za naš SFTR sistem in dane eksperimentalne pogoje. Pomembno je navesti, da so v prejšnjih SFTR študijah objavili oceno za spodnjo mejo razširitve 25% globine profila, ki je bila dobljena z numerično simulacijo brezšumnih signalov in brez napake linearizacije. Naša ocena razširitve je skoraj 2-krat manjša.

Bibliography

[1] Wang LW and Wu H 2007 *Biomedical Optics* (Wiley, New York)

[2] Barsky SH, Rosen S, Geer DE and Noe JM 1980 The nature and evolution of port wine stains: a computer-asisted study *J Invest Dermatol* **74** 154–7

[3] van Gemert MJC, Nelson JS, Milner TE, Smithies DJ, Verkruysse W, de Boer JF, Lucassen GW, Goodman DM, Tannenbaum BS, Norvang LT and Svaasand LO 1997 Non-invasive determination of port wine stain anatomy and physiology for optimal laser treatment strategies *Phys Med Biol* **42** 937–50

[4] Verkruysse W, Majaron B, Tannenbaum BS and Nelson JS 2000 Optimal cryogen spray cooling parameters for pulsed laser treatment of port wine stains *Las Surg Med* **27** 165–70

[5] Jacques SL, Nelson JS, Wright WH and Milner TE 1993 Pulsed photothermal radiometry of port-wine-stain lesions *Appl Opt* **32** 2439–46

[6] Milner TE, Goodman DM, Tanenbaum BS and Nelson JS 1995 Depth profiling of laser-heated chromophores in biological tissues by pulsed photothermal radiometry *J Opt Soc Am A: Optics, Vision* **12** 1479-88

[7] Milner TE, Smithies DJ, Goodman DM, Lau A and Nelson JS 1996 Depth determination of chromophores in human skin by pulsed photothermal radiometry *Appl Opt* **35** 3379-85

[8] Vitkin IA, Wilson BC and Anderson RR 1995 Pulsed photothermal radiometry studies in tissue optics *Optical-Thermal Response of Laser-Irradiated Tissue* eds Welch AJ and van Gemert MJC (Plenum Press, New York)

[9] Sathyam US and Prahl SA 1997 Limitations in measurement of subsurface temperatures using pulsed photothermal radiometry *J Biomed Opt* **2** 251-61

[10] Smithies DJ, Millner TE, Tanenbaum BS, Goodman DM and Nelson JS 1998 Accuracy of subsurface distributions computed from pulsed photothermal radiometry *Phys Med Biol* **43** 2453–63

[11] Majaron B, Verkruysse W, Tanenbaum BS, Milner TE, Telenkov SA, Goodman DM and Nelson JS 2000 Combining two excitation wavelengths for pulsed photothermal profiling of hypervascular lesions in human skin *Phys Med Biol* **45** 1913–22

[12] Choi B, Majaron B and Nelson JS 2004 Computational model to evaluate port wine stain depth profiling using pulsed photothermal radiometry *J Biomed Opt* **9** 299–307

[13] Fujimoto JG 2002 Optical coherence tomography : Introduction *Handbook of Optical Coherence Tomography* eds Bouma BE and Tearney GJ (Dekker, New York)

[14] Pouge BW, Testorf M, McBride T, Osterberg U, and Paulsen K 1997 Instrumentation and design of a frequency domain diffuse optical tomography imager for breast cancer detection *Opt Express* **1(13)** 391–403

[15] Li J and Wang LHV 2004 Ultrasound-modulated optical computed tomography of biological tissues *Appl Phys Lett* **84(9)** 1597–9

[16] Diebold GJ, Sun T and Khan MI 1991 Photoacustic monopole radiation in 1-dimension, 2-dimension and 3-dimension *Phys Rev Lett* **67 (24)** 3384–7

[17] Leung WP and Tam AC 1984 Technique of flash radiometry *J Appl Phys* **56** 153–161

[18] Majaron B, Verkruysse W, Tanenbaum BS, Milner TE and Nelson JS 2002 Spectral variation of infrared absorption coefficient in pulsed photothermal profiling of biological samples *Phys Med Biol* **47** 1929–46

[19] Telenkov SA, Tanenbaum BS, Goodman DM, Nelson JS and Milner TE 1999 In Vivo Infrared Tomographic Imaging of Laser-Heated Blood Vessels *IEE J Sel Top Quant Elect* **5 (4)** 1193–9

[20] van Gemert MJC and Welch AJ 1995 Approximate solutions for heat conduction: Time constants *Optical-Thermal Response of Laser-Irradiated Tissue* eds Welch AJ and van Gemert MJC (Plenum Press, New York)

[21] Mandelis A 1995 Green's functions in thermal-wave physics: Cartesian coordinate representations *J Appl Phys* **78 (2)** 647–55

[22] Vincent JD 1989 Fundamentals of Infrared Detector Operation and Testing (Wiley, New York)

[23] Dreniak EL and Crowe DG 1984 *Optical Radiation Detectors* (Wiley, New York)

[24] Witteman WJ 2006 *Detection and Signal Processing* (Springer, Heidelberg)

[25] Björck A 1996 Numerical Methods for Least Squares Problems (Philadelphia: SIAM)

[26] Hansen PC 1998 Rank-Deficient and Discrete Ill-Posed Problems (Philadelphia: SIAM)

[27] Hansen PC 2007 *Regularization Tools* (web released: www2.imm.dtu.dk/~pch/Regtools)

[28] Calvetti D 2007 Preconditioned iterative methods for linear discrete ill-posed problems from a Bayesian inversion perspective *J Comp Appl Math* **198** 378–95

[29] Hoffmann B 1986 Regularization for Applied Inverse and Ill-Posed Problems: A numarical approach (Leipzig: Teubner)

[30] Shewchuk JR 1995 An Introduction to the Conjugate Gradient Method Without the Agonizing Pain (web released: www.cs.cmu.edu/~quake-papers/painless-conjugate-gradient.pdf)

[31] Brakhage H 1987 On ill-posed problems and the method of conjugate gradients *Inverse and Ill-Posed Problems* ed Engl HW and Groetsch CW (London: Academic Press) pp 165–75

[32] Press WH, Flannery BP, Teukolsky SA and Vetterling WT 1992 Numerical recipes in C (Cambridge: Cambridge University Press)

[33] Hanke M 1995 *Conjugate Gradient Type Methods for Ill-Posed Problems* (Harlow: Longman Scientific & Technical)

[34] Tikhonov AN and Arsenin VA 1977 *Solutions of Ill-posed Problems* (Winston & Sons, Washington)

[35] Craven P and Wahba G 1979 Smoothing noisy data with spline function *Numer Math* **31** 377–403

[36] Golub GH, Heath MT and Wahba G 1979 Generalized cross-validation as a method for choosing a good ridge parameters *Technometrics* **21** 215–23

[37] Girard PA 1989 A fast ‘Monte Carlo cross-validation’ procedure for large least squares problems with noisy data *Numer Math* **56** 1–23

[38] Lawson CL and Hanson RJ 1974 *Least Squares Problems* (Englewood Cliffs, N.J.: Prentice-Hall)

[39] Bertero M and Boccacci P 1998 Introduction to Inverse Problems in Imaging (Bristol: Institute of Physiscs Publishing)

[40] Hanke M, Nagy J and Vogel C 2000 Quasi-Newton approach to non-negative image restorations *Linear Algebra Appl* **316** 223–36

[41] Nagy J and Strakoš Z 2000 Enforcing non-negativity in image reconstruction algorithms Mathematical Modeling, Estimation and Imaging (SPIE vol 4121) ed DC Wilson et al (Bellingham, WA: The International Society for Optical Engineering) pp. 182–90

[42] Calvetti D, Landi G, Reichel L and Sagallari F 2004 Non-negativity and iterative methods for ill-posed problems *Inverse Problems* **20** 1747–58

[43] Favati P, Lotti G, Menchi O and Romani F 2006 Iterative image restoration with non negativity constraints (Pisa: Istituto di Informatica e Telematica)

[44] Dempster AP, Laird NM and Rubin DB 1977 Maximum Likehood Estimation from Incomplete Data via the EM Algorithm *J Royal Statistical Society B*: **30** 1–38

[45] Archer GEB and Titterington DM 1995 The iterative image space reconstruction algorithm (ISRA) as an alternative to the EM algorithm for solving positive linear inverse problems *Stat. Sinica* **5** 77–96

[46] Verkruysse W, Majaron B, Choi B and Nelson JS 2005 Combining singular value decomposition and non-negative constraint in a hybrid method for photothermal depth profiling *Review Sci Instr* **76** 024301-024301-6

[47] Majaron B and Milanič M 2007 Re-evaluation of pulsed photothermal radiometric profiling in samples with spectrally varied infrared absorption coefficient *Phys Med Biol* **52** 1089-101

[48] Palik ED ed 1991 *Handbook of Optical Constants in Solids II* (Boston, MA: Academic Press)

[49] Milanič M, Majaron B and Nelson J S 2007 Pulsed photothermal temperature profiling of agar tissue phantoms Lasers Med Sci **22 (4)** 279–84

[50] Milanič M, Majaron B and Nelson J S 2007, Optimal spectral acquisition band for temperature profiling in human skin using pulsed photothermal radiometry, Photonic Therapeutics and Diagnostics III vol 6424, ed N Kollias et al (Bellingham, WA: SPIE) pp. 6424S

[51] Viator JA, Choi B, Peavy GM, Kimel S and Nelson JS 2003 Spectra from 2.5-15 μm tissue phantom materials, optical clearing agents and ex vivo human skin: implications for depth profiling of human skin *Phys Med Biol* **48** N15-N24

[52] Duck FA 1990 *Physical Properties of Tissue* (London: Academic Press) ch 2

[53] Prahl SA, Vitkin IA, Bruggemann U, Wilson BC and Anderson RR 1992 Determination of optical properties of turbid media using pulsed photothermal radiometry *Phys Med Biol* **37** 1203-17

[54] Pogue BW and Patterson MS 2006 Review of tissue simulating phantoms for optical spectroscopy, imaging and dosimetry *J Biomed Opt* **11** 1–16

[55] Pifferi A, Torricelli A, Bassi A, Taroni P, Cubeddu R, Wabnidz H, Grosenick D, Moeller M, Macdonald R, Swartling J, Svensson T, Andersson-Engels S, van Veen RLP, Sterenborg JCM, Tualle JM, Nghiem HL, Avrillier S, Whelan M and Stamm H 2005 Performance assessment of photon migration instruments: the MEDPHOT protocol *Appl Opt* **44 (11)** 2104–24

[56] Nesvadba P 1982 A new transient method of the measurement of temperature dependent thermal diffusivity *J Phys D: Appl Phys* **15** 725-38

[57] Opuku A, Tabil LG, Crerar B and Shaw MD 2006 Thermal conductivity and thermal diffusivity of timothy hay *Canadian Biosystems Engineering* **48** 3.1–3.7

[58] Medina-Esquivel R, Yanez-Limon JM, Alvarado–Gil JJ 2005 Measurement of phase transitions and thermal diffusivity in agar using a thermal wave resonator *J Phys IV* **125** 811-5

[59] Dickerson RW Jr 1965 An Apparatus For The Measurement Of Thermal Diffusivity Of Foods *Food Technol* **19(5)** 198-204

[60] Yao CH, Liu BS, Chang CJ, Hsu SH and Chen YS 2004 Preparation of networks of gelatin and genipin as degradable biomaterials *Materials Chem. Phys.* **83** 204–8

[61] Jacques SL 1998 *Skin optics* (web released: http://omlc.ogi.edu/news/jan98/skinoptics.html)

[62] Doyley MM, Weaver JB, Van Houten EE, Kennedy FE and Paulsen KD 2003 Treshold for detecting and characterizing focal lesions using steady-state MR elastography *Med Phys* **30 (4)** 495-504

[63] Wilson BC 1995 Measurement of tissue optical properties: methods and theories *Optical-Thermal Response of Laser-Irradiated Tissue* ed Welch J A (Plenum, New York) pp. 233–271

[64] Kim J, Oh J, Milner TE and Nelson JS 2006 Hemoglobin contrast in magnetomotive optical Doppler tomography *Opt Lett* **6** 778–80

[65] Cody WJ 1969 Rational Chebyshev Approximations for the Error Function *Math. Comp.*, pp. 631–638

Izjava

Izjavljam, da sem v disertaciji predstavil rezultate lastnega znanstvenoraziskovalnega dela.

Ljubljana, 2.5.2008 Matija Milanič